ISSN **2960-9534**
DOI https://doi.org/10.36073/2960-9534

JOURNAL OF THE GEORGIAN CERAMISTS' ASSOCIATION

INTERNATIONAL JOURNAL OF CERAMICS, COMPOSITES, SCIENCE AND ADVANCED TECHNOLOGIES

Scientific, technical and industrial illustrated, registered, referral magazine

Vol. 28. 1(55).2026

Guidelines for submitting an article to the journal

- It is necessary to submit, one hardcopy of the article, as well as an electronic versionin English language, to editorial office.
- The length of the article is not limited to pages (including tables and images with appropriate numbering). Interval 1.5. Program-Sylfaen. Font size 12, the article must be accompanied by an abstract in Georgian of no more than 300 words.
- The article should use International System of Units (SI), as well as those units that are equated to this system.
- Mathematical and chemical formulas should be clearly indicated so that the difference between Capital (upper case) and Nuskhuri (Georgian script AD 800-1100) (lower case) letters, quality coefficient and co-multiplier can be easily discerned. All letter designations in the text of the article and formula are subject to decoding. Different concepts can not be represented by the same symbol.
- The literary source should be indicated at the end of the article as follows: for a book - indicating the author, title, title of publication, place of publication, year of publication and total number of pages;

  for a journal - indicating the author of the article, the name of the journal, year of publication, volume, number, beginning and end pages of the article;

  Foreign surnames, the title of the book and journal must be in the original language without abbreviation, it is not allowed to refer to unpublished work.
- When using a copyright certificate, it is necessary to refer to the bulletin of the invention (where the formula of the invention is published) indicating the number and year of publication.
- Pictures and drawings should be presented only in text in one copy in computerized form, they should not be overloaded with details and inscriptions. The position must be indicated by numbers and decoded by inscriptions under the picture;
- The article must be signed by one of the authors. It is necessary to indicate place of work, position, scientific degree, and telephone number.
- The publishing fee for foreign authors not residing in Georgia makes up 100 euros. It's free for authors residing in Georgia.

CONTENTS

Z. Kovziridze, N. Nizharadze, T. Loladze, N. Loladze, G. Tabatadze, T. Cheishvili, M. Mshvildadze, V. Qinqladze, N. Darakhvelidze, M. Balakhashvili. MULTIFUNCTIONAL COMPOSITE IN THE B_4C-SiC-TiC- TiB_2-PERLITE SYSTEM 5

Z. Kovziridze. THERMAL SHOCK RESISTANCE FORMULA FOR COMPOSITE MATERIALS 18

Z. Kovziridze, M. Mshvildadze, N. Kutsiava, T. Loladze, T. Tsilosani, N. Nizharadze, G. Tabatadze, M. Kapanadze, M. Balakhashvili, N. Darakhvelidze, V. Qinqladze. SYNTHESIS AND CHARACTERIZATION OF β SiAlON-SiC COMPOSITES BASED ON NATURAL ALUMINOSILICATES 33

Z. Kovziridze, N. Mitskevich, S. Badzgaradze, G. Mentheshashvili, P. Khorava, A. Saldadze. TREATMENT OF MALIGNANT TUMORS WITH MAGNETIC HYPERTHERMIA AND GUIDED LOCAL HYPERTHERMIA 48

N. Gegia, T. Rukhadze, G. Enukidze, K. Khachaturiani, M. Tkemaladze, T. Loladze. PRODUCTION OF VITRIFIED CERAMIC TILES FROM GURIA POLYMINERAL CLAYS AND OBSIDIAN COMPOSITES 75

UDC 666.762.93

MULTIFUNCTIONAL COMPOSITE IN THE B_4C-SiC-TiC- TiB_2-PERLITE SYSTEM

Z. Kovziridze, N. Nizharadze, T. Loladze, N. Loladze, G. Tabatadze, T. Cheishvili,

M. Mshvildadze, V. Qinqladze, N. Darakhvelidze, M. Balakhashvili.

Georgian Technical University, Institute of Bionanoceramics and Nanocomposite Technology, Bionanoceramic and Nanocomposite Materials Science Center. 69 Kostava Str., Tbilisi, 0175, Georgia

E-mail: kowsiri@gtu.ge

Resume: **Objective:** This study aims to fabricate a composite material with enhanced technical and performance characteristics within the B_4C-SiC-TiC-TiB_2-perlite system.

Method: The composite was fabricated via hot pressing at a temperature of 1620°C under a pressure of 25 MPa for 50 min, followed by a 10-minute dwell time at the peak temperature. Phase and microstructural analyses were conducted using X-ray diffraction (DRON-3) and scanning electron microscopy (SEM). Mechanical properties were evaluated using an R-100 tensile testing machine and a Rockwell hardness tester.

Results: A composite within the B_4C-SiC-TiC-TiB_2-perlite system was successfully obtained. During the hot-pressing process, an in-situ reaction occurred between titanium carbide (TiC) and boron carbide (B_4C), leading to the formation of titanium diboride (TiB_2) grains, which significantly enhanced the mechanical properties of the composite. Furthermore, in the presence of perlite, a liquid glass phase formed during sintering, establishing grain-boundary "bridges" with the carbide grains, thereby further improving the mechanical performance.

Conclusion: The resulting material exhibits high mechanical strength, achieving a flexural strength of 389 MPa, a compressive strength of 1923 MPa, and a remarkably high impact toughness of 11.2 kJ/m². These composites are highly suitable for use in wear-resistant components operating under high dynamic loads and impact conditions

Key words: Composite, correlation, porous phase, mechanical strength, microstructure

1. INTRODUCTION

In modern materials science, the development and implementation of advanced manufacturing technologies are widely recognized as vital prerequisites for engineering competitive, multi-functional materials that drive national economic growth. High-temperature, hetero-modulus, advanced ceramic matrix composites (CMCs) represent a crucial class of such materials. They are characterized by outstanding physicochemical and technical properties (e.g., high hardness, superior ultimate strength, fracture toughness, and elastic modulus), excellent processability (such as machinability with cutting tools), and exceptional operational parameters (including wear resistance,

reliability under static and dynamic loading, and radiation stability).

The foundational components of these high-performance materials are refractory compounds, such as boron carbide, boron nitride, tantalum carbide, zirconium oxide, aluminum oxide, yttrium oxide, silicon nitride, silicon carbide, titanium and zirconium borides, as well as titanium, tungsten, and tantalum carbides. These compounds exhibit remarkable thermodynamic stability, ultra-high hardness, and superb wear resistance, maintaining these attributes even under extreme temperatures - a critical factor for their successful industrial application.

The present study focuses on the fabrication and characterization of composite ceramic materials based on the boron carbide (B_4C) and silicon carbide (SiC) systems. The initial nominal composition selected for composite formulation was (wt. %): 60% B_4C, 20% SiC, 13% TiC, and 3% perlite.

These constituent compounds were chosen for their unique properties, including high hardness, high melting points, superior corrosion resistance, wear resistance, and low density. However, unlike some other advanced engineering ceramics, individual carbides exhibit inherently low fracture toughness and poor impact resistance, which limits their widespread industrial adoption despite their exceptional intrinsic advantages.

Extensive research has been dedicated to developing various specialized composites based on these compounds, particularly for armoring and defense applications where low density is crucial [1–13]. In this work, titanium carbide (TiC) was introduced into the base B_4C-SiC mixture to induce an in-situ chemical reaction between TiC and B_4C during thermal consolidation. This interaction leads to the formation of titanium diboride (TiB_2), as confirmed by X-ray diffraction (XRD) analysis (Figure 1). Although TiB_2 independently exhibits exceptional technical properties, our specific objective was to generate highly dispersed, in-situ TiB_2 grains that distribute uniformly throughout the bulk volume of the composite within the amorphous glass matrix derived from volcanic perlite (Figure 2).

The chemical composition of the utilized raw perlite is as follows (wt.%): SiO_2 – 72.11; Al_2O_3 – 15.56; Fe_2O_3 – 0.53; CaO – 0.71; MgO – 0.35; K_2O – 4.87; Na_2O – 3.27; loss on ignition (LOI) – 3.03. Its melting temperature is 1240°C. The material contains approximately 76 wt.% of a glassy phase, with the remainder consisting of crystallites and entrapped volcanic gases retained during the rapid cooling of the erupted lava. The density of the perlite ranges between 2.3–2.4 g/cm³.

The structural, morphological, and elemental composition of the consolidated samples were investigated using a JEOL JSM-6510LV scanning electron microscope (Japan), equipped with an Oxford Instruments X-MaxN energy-dispersive X-ray spectroscopy (EDS) microanalysis system (UK). Scanning electron micrographs of the surfaces were acquired in both secondary electron imaging (SEI) and backscattered electron (BES) modes, utilizing an accelerating voltage of 20 kV. To mitigate surface charging, select samples were sputter-coated with an approximately 10 nm thick layer of platinum (Pt) using a JEOL JEC-3000FC vacuum coating system.

2. MAIN PART

Figure 1 displays the X-ray diffraction pattern of the synthesized composite, confirming the presence of the constituent phases via their characteristic interplanar spacings (dhkl).

Figure 2 presents the morphological analysis of a polished sample surface. The microstructure clearly displays the grey silicon carbide grains and white boron carbide grains interspersed with newly formed titanium diboride particulates, as verified by the micro-spectral and electronic configurations (Figure 4).

To microscopically investigate the fracture behavior of the composite, fractographic evaluation was conducted on freshly fractured surfaces via SEM. Figure 3 illustrates the scanning electron micrograph of the fracture surface.

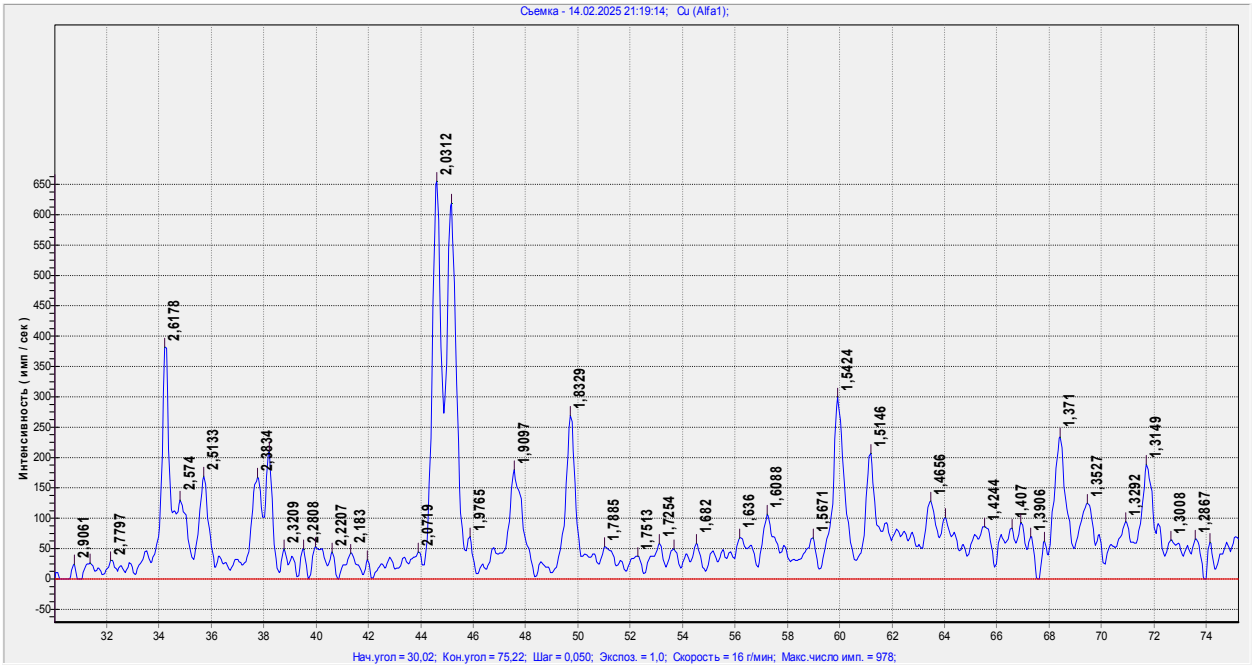

Fig. 1. XRD pattern of the obtained composite.

TiB_2 - dhkl - 1.3149; 1.371; 1.5146; 1.6088; 2.0312; 2.6178 Å .

SiC - dhkl - 1.5424; 1.9097; 2.3834; 2.5133; 2.574 Å

B_4C - dhkl - 238 Å

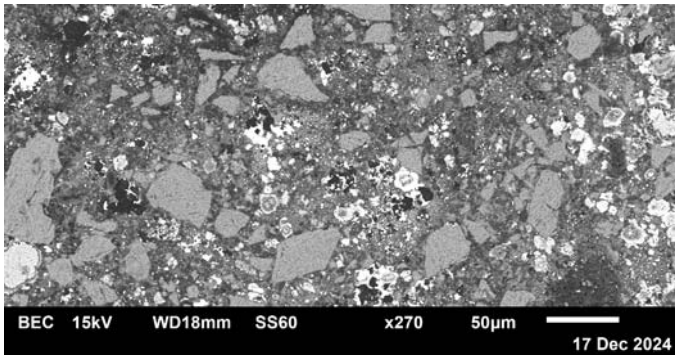

Fig. 2. Microstructure of the composite.

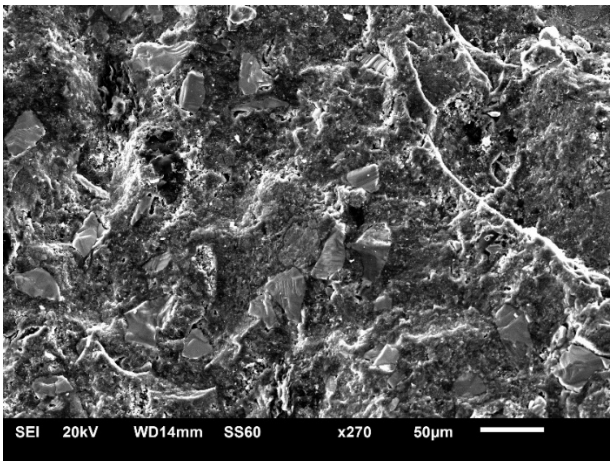

Fig. 3. SEM micrograph of the fracture surface of the investigated composite.

From Figure 3, it can be inferred that the morphology observed on the surface is identical to that throughout the entire volume of the specimen, demonstrating macrostructural homogeneity. Regarding the failure mechanism, it is evident that fracture proceeds through a combination of transcrystalline (cleavage) and plastic deformation modes. Concurrently, the crystalline phases undergo stepped, multi-level fracturing, which acts to effectively impede the crack propagation velocity. This failure-energy dissipation mechanism is well-reflected in the excellent mechanical strength values exhibited by the specimens (Table 1).

Table 1

Physical and Mechanical Characteristics of the B_4C-SiC-TiB_2-Perlite Composite

Composite System	Theoretical Density γ_{th} (g/cm³)	Relative Density γ_r	Open Porosity Π (%)	Hardness (HRA)	Compressive Strength σ_c (MPa)	Flexural Strength σ_f (MPa)	Impact Toughness A (kJ/m²)
B_4C-SiC-TiB_2-perlite	3.1	0.96	<1.0	91	1923	389	11.2

As summarized in Table 1, the processed composite is characterized by high physical and mechanical properties along with low bulk porosity, which vastly improves its prospects for high-stress engineering applications.

From the EDS microanalysis patterns and elemental mapping presented in Figures 4 and 5, it is distinctively observed that the in-situ formed titanium diboride phase encapsulates the silicon carbide grains. Consequently, upon crack initiation within a carbide grain, the surrounding TiB_2 localizes the stress field and noticeably arrests crack propagation [1]. Simultaneously, the unreacted boron carbide and titanium diboride grains are interlinked via thin-film bridges composed of the amorphous glass phase [2].

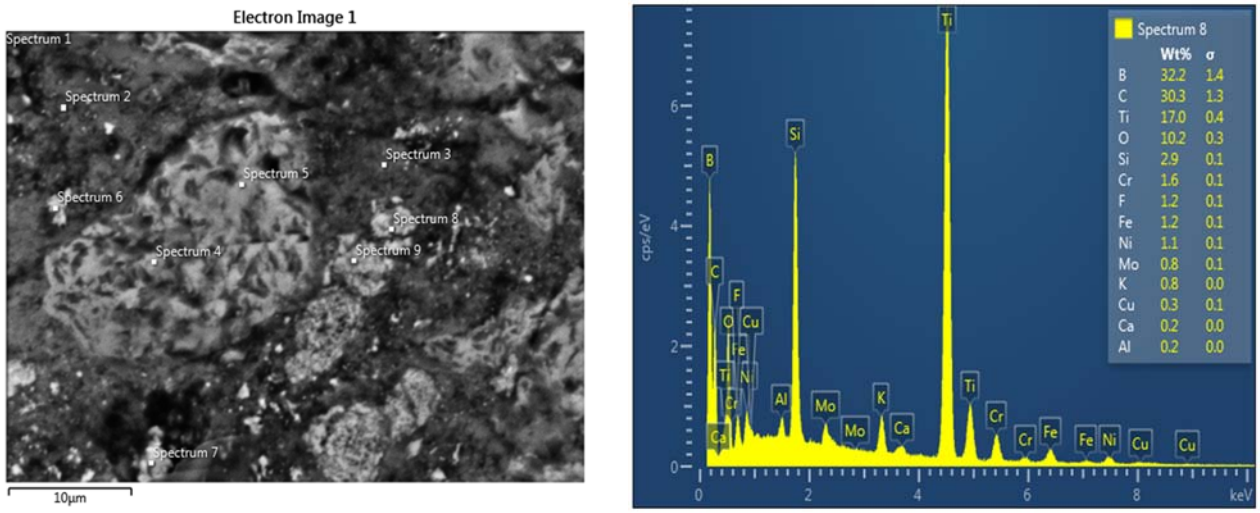

Fig. 4. EDS microanalysis patterns of the investigated composite.

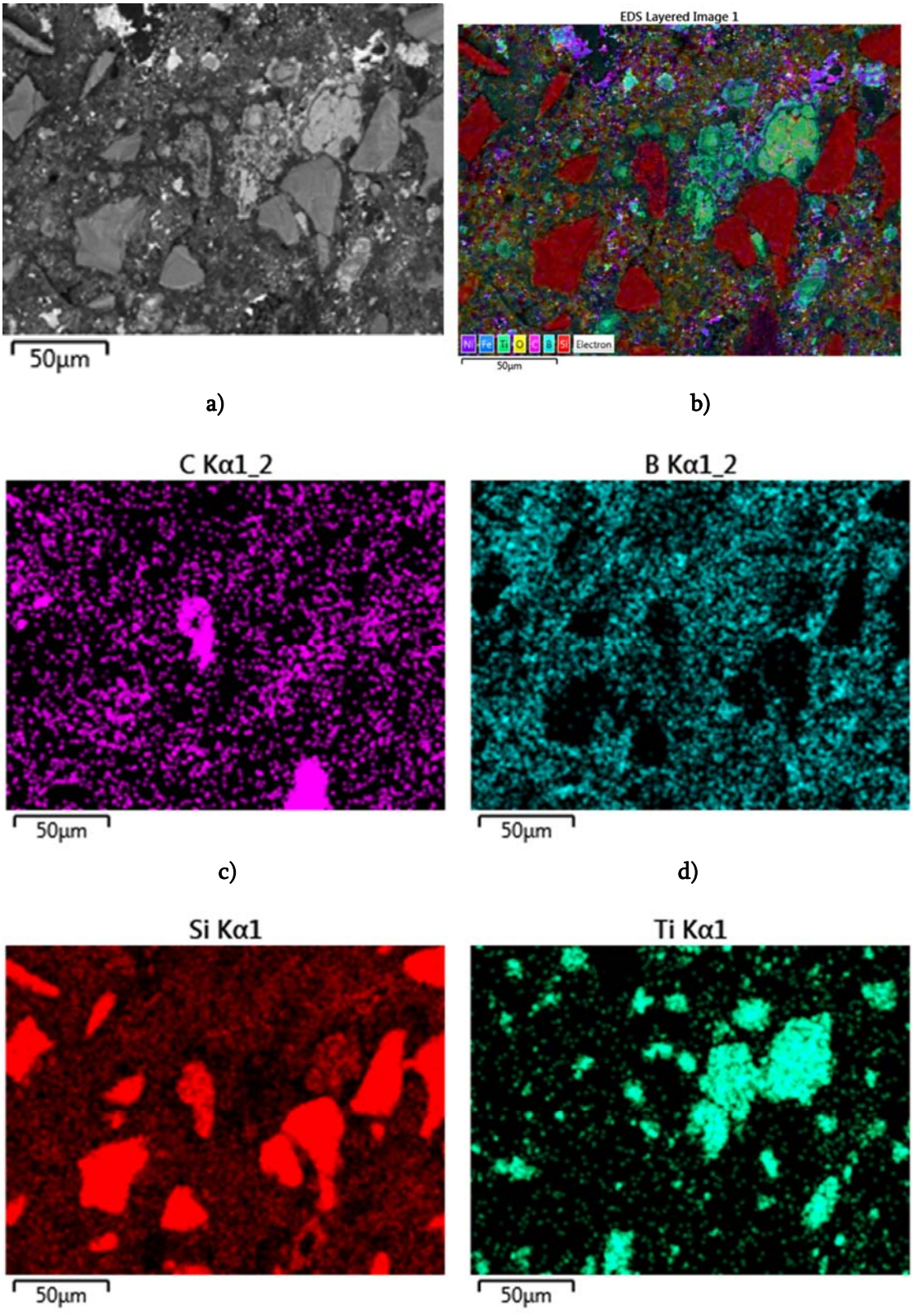

Fig. 5. EDS elemental mapping of the phases in the composite matrix.

To mathematically model and characterize the composite matrix, we applied the structural-mechanical analytical formulations developed by Z. Kovziridze, which define the dependence of mechanical properties on the porous phase architecture and the correlation between crystalline phase morphology and macro-mechanical performance [14]. For this purpose, the geometric parameters of the pores and crystalline grains were extracted from the microstructural images and tabulated (Tables 2 and 3).

Table 2

Morphological Parameters of the Porous Phase

Field Area S (μm²)	Total Pore Area Sp (μm²)	Max Pore Size Dmax (μm)	Min Pore Size Dmin (μm)	Shape Factor Fp = Dmax/Dmin	Distribution Factor Pd	Vol Fraction Pvol (%)	Avg Pore Size Pm (μm)	Flexural Load P (MPa)
36,500	303	10.5	2	0.9	0.83	7	2	389

The empirical equation relating flexural behavior to porosity is expressed as:

$$\sigma_{m/p} = P / (Fp \cdot Pd \cdot Pvol \cdot Pm)$$

Where:

P is the applied flexural load (MPa); F_p is the pore shape factor; P_d is the spatial distribution factor of pores within the matrix; P_{vol} is the volume fraction of the porous phase in the matrix; and P_m is the average pore size.

Substituting the values from Table 2:

$$\sigma_{m/p} = 389 / (0.9 \cdot 0.83 \cdot 7 \cdot 2) = 389 / 10.46 = 37.2 \text{ MPa}$$

Table 3

Morphological Parameters of the Crystalline Phase

Field Area S (μm²)	Total Crystal Area Sc (μm²)	Max Crystal Size Dmax (μm)	Min Crystal Size Dmin (μm)	Shape Factor Fkf = Dmax/Dmin	Distribution Factor Fkd	Vol Fraction Kv (%)	Avg Crystal Size Km (μm)	Flexural Load P (MPa)
36,500	36,197	18.4	4.5	4.1	0.9	89.17	6	389

The analytical equation correlating strength with the crystalline morphology is given by:

$$\sigma_d = (P \cdot F_{kd}) / (Km \cdot Kv \cdot F_{kf})$$

Where:

P is the applied load in flexure or compression (MPa); F_{kd} is the spatial distribution factor of crystals within the matrix; K_m is the average crystal size (μm); K_v is the volume fraction of the crystalline phase (wt.%); and F_{kf} is the crystal shape factor.

Calculating for flexural loading (P = 389 MPa):

$$\sigma_d = PxF_{kd}/KmKvF_{kf} = 389x0,9/\ 6 \cdot 89,17 \cdot 4.5 =$$
$$= 389.0,9/\ 2407.6 = O.17$$

Calculating for compressive loading (P = 1923 MPa):

$$\sigma_d = PxF_{kd}/KmKvF_{kf} = 1923x0,9/\ 6 \cdot 89,17 \cdot 4.5 =$$
$$= 1730.7/2407.6 = O.\ 72$$

This mathematical model successfully incorporates both bulk and surface defects of the crystals, the micro- and macrostructural volumetric and surface topologies, the composition and spatial arrangement within the matrix, and the phase transformations occurring due to chemical and physicochemical reactions during material consolidation.

As observed from the analytical calculations, the structural correlation index is not high. We attribute this lower correlation to the elevated value of the crystal shape factor. In this study, the raw batch mixture was intentionally not processed in an attritor or planetary ball mill, allowing the materials to retain their initial as-received particle size distribution. The disparity between the minimum and maximum particle fractions was substantially large, which inherently constrained the correlation coefficients (0.17 for flexure and 0.72 for compression). To optimize these parameters, the crystal shape factor should ideally not exceed a value of 3, and the average grain size should be maintained within a tighter 7 - 8 μm envelope, distributed homogeneously throughout the matrix.

It has been experimentally established that fine-grained microstructures exhibit significantly higher mechanical strength compared to coarse-grained variants [15–19], as the critical Griffith microcrack length is directly bounded by the grain size boundaries. This phenomenon is typically associated with localized internal stress generation at grain boundaries caused by anisotropic thermal expansion behavior [20–26].

The bulk and surface electrical resistivities (ρ_v, ρ_s) of the consolidated material were experimentally measured as a function of temperature within the 25–300°C range. Resistivity measurements were conducted inside a specialized, temperature-controlled cell simultaneously using two parallel specimens monitored via an electronic digital ohmmeter.

The disk-shaped test specimens featured a diameter-to-height ratio (D/H) of approximately 5. Air-dry samples (stabilized at 25°C with a relative air humidity of 47.5%) were initially positioned inside the measuring cell to determine baseline Rv and Rs values. Subsequent electrical resistance data points within the 100–300°C range were acquired at regular temperature steps of 50°C. Through appropriate geometric calculations, the specific volume resistivity ρv (Ω · m) and surface resistivity ρs (Ω) were derived, mapping the "$\rho_{v,s}$ - t" relationships presented in Figure 6.

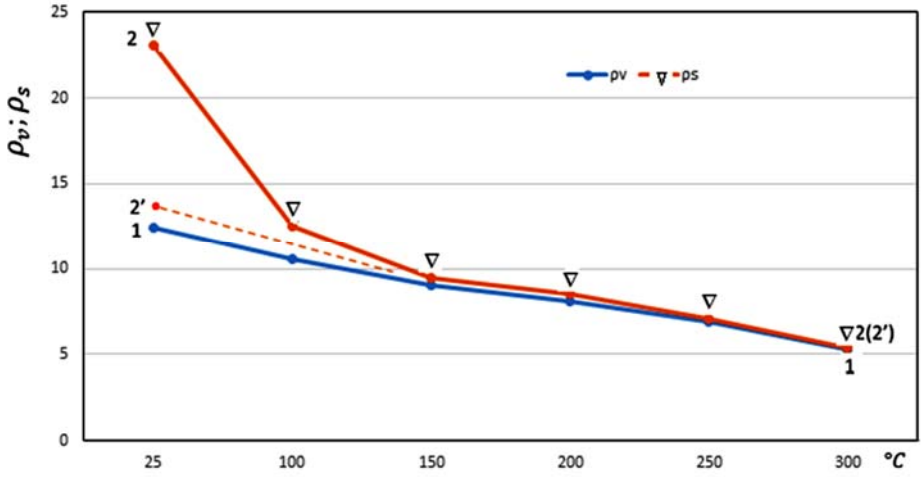

Fig. 6. Temperature dependence of specific volume resistivity $\rho_v - t$ (1) and surface resistivity $\rho_s - t$ (2, 2^1) of the material.

The experimental data indicate that the temperature-dependent variation of ρv is strictly linear, with specific volume resistivity decreasing by nearly a factor of two across the 25–300°C range. A unique hysteresis-like behavior was observed for the surface resistivity (ρ_s) under reversible thermal cycling conditions (25–300°C). For the pristine sample (Curve 2), the ρ_s values recorded at room temperature were initially high but dropped sharply in the 25–150°C interval, subsequently matching the ρ_v curve at higher temperatures. Upon cooling the system back down (reversible cycle, Curve 2^1), the ρ_s values closely coincided with the volume resistivity profile (ρ_v), showing minimal divergence. This distinct discrepancy in the path of the "ρ_s - t" curves during reversible thermal cycling is attributed to the desorption of moisture initially condensed on the surface of the specimen. As the test progressed, this surface moisture evaporated, leading to the convergence of the surface and volume resistivity values at elevated temperatures.

The fundamental electrical parameters, calculated for the 25–300°C thermal window, are compiled in Table 4. The composite material, comprising a matrix dominated by titanium, silicon, and boron carbides, which are well-documented semiconducting compounds, demonstrates classical, well-defined semiconducting electrical transport behavior.

Table 4

Electro-physical Properties of the Composite Material

No.	Electrical Characteristic	Symbol	Unit	Value
1	Temperature Coefficient of Electrical Sensitivity	B	$\Omega \cdot m \cdot K$	529.1
2	Temperature Coefficient of Electrical Resistance	$\Delta\alpha_T$	$\Omega \cdot m \cdot K^{-1}$	-2.7×10^{-3}
3	Activation Energy of Electrical Conductivity	ΔE	eV	0.334

The resulting material, whose composition predominantly features the carbides of titanium, silicon, and boron, well-documented semiconductors based on their electrical performance profiles, exhibits electrical properties characteristic of conventional semiconducting materials.

3. CONCLUSION

1. During hot pressing at 1620°C, an in-situ chemical reaction occurred between titanium carbide (TiC) and boron carbide (B4C), generating highly dispersed titanium diboride (TiB2) grains that served to substantially enhance the mechanical strength parameters of the resulting composite.

2. The addition of 3 wt.% volcanic perlite induced the formation of a liquid glass phase during sintering. This phase created microscopic "bridges" at the boundaries of the carbide grains, further increasing the overall mechanical performance of the material.

3. Analytical correlation models were successfully implemented to establish the quantitative relationships between the structural morphology of the matrix (porous and crystalline phases) and its macro-mechanical performance.

4. Electro-physical characterization confirmed that the B4C-SiC-TiC-TiB2-perlite composite exhibits distinct semiconducting properties, governed by its constituent carbide phases, with a calculated electrical activation energy of 0.334 eV.

REFERENCES

1. Lensky, V. V., Chikina, A. A., et al. (2008). Development of armor shells for personal armor protection from reaction-bonded silicon carbide. *Scientific and Technical Collection: Issues of Defense Technology (Series 15)*, *1*(148)–*2*(149).
2. *Method for manufacturing a ceramic armor material based on silicon carbide and boron carbide*. (1974). U.S. Patent No. 3,796,564. U.S. Patent and Trademark Office.
3. *Composite ceramic material*. (2004). U.S. Patent No. 6,805,034. U.S. Patent and Trademark Office.
4. Wang, B., Cai, D., Wang, H., Zou, W., Yang, Z., Duan, X., He, P., Li, D., Duan, W., Jia, D., Lin, H.-T., Zhao, C., & Zhou, Y. (2023). Microstructures and mechanical properties of B_4C–SiC and B_4C–SiC–TiB_2 ceramic composites fabricated by hot pressing. *Journal of the*

American Ceramic Society, *106*(8), 4982–4994. https://doi.org/10.1111/jace.19136

5. Kovziridze, Z., Mestvirishvili, Z., & Tabatadze, G. (2012). Influence of TiB_2 and ZrB_2 additives on the properties of boron carbide. *Ceramics*, *27*(1), 33–39.
6. Srivatsan, T.S., Guruprasad, G., Black, D., Radhakrishnan, R., & Sudarshan, T.S. (2005). Influence of TiB_2 content on microstructure and hardness of TiB_2–B_4C composite. *Powder Technology*, *159*(3), 161–167. https://doi.org/10.1016/j.powtec.2005.08.005
7. Huang, S. G., Vanmeensel, K., Malek, O. J. A., Van der Biest, O., & Vleugels, J. (2011). Microstructure and mechanical properties of pulsed electric current sintered B_4C–TiB_2 composites. *Materials Science and Engineering: A*, *528*(3), 1302–1309. https://doi.org/10.1016/j.msea.2010.10.024
8. Kriener, M., Muranaka, T., Kato, J., Ren, Z. A., Akimitsu, J., & Maeno, Y. (2008). Superconductivity in heavily boron-doped silicon carbide. *Science and Technology of Advanced Materials*, *9*(4), Article 044205. https://doi.org/10.1088/1468-6996/9/4/044205
9. Kovziridze, Z., Nizharadze, N., Tabatadze, G., Nikoleishvili, E., Mestvirishvili, Z., & Kinkladze, V. (2011). Multifunctional hetero-modulus composites in the B_4C-BN-TiC-SiC-C system. *Journal of the European Ceramic Society*, *31*(10), 1921–1926. https://doi.org/10.1016/j.jeurceramsoc.2011.03.014
10. Kovziridze, Z., Nijaradze, N., Tabatadze, G., Mshvildadze, M., Nikoleishvili, E., & Mestvirishvili, Z. (2013). Improvement of boron carbide mechanical properties in B_4C-TiB_2 and B_4C-ZrB_2 systems. *Journal of Electronics Cooling and Thermal Control*, *3*(2), 43–48. https://doi.org/10.4236/jectc.2013.32006
11. Kovziridze, Z., Nijaradze, N., Tabatadze, G., & Mestvirishvili, Z. (2013). Ceramic composite in the Al_2O_3-B_4C-TiC system. *Ceramics*, *2*(30), 19–22.
12. Kovziridze, Z., Nijaradze, N., Tabatadze, G., Darakhvelidze, N., & Mestvirishvili, Z. (2015). Smart materials in the SiAlON-SiC-Al_2O_3 system. *Journal of Material Science and Engineering* (International Conference and Expo on Ceramics, August 17-18, 2015, Chicago, USA).
13. Kovziridze, Z., Nijaradze, N., Tabatadze, G., Darakhvelidze, N., & Balakhashvili, M. (2018). Obtaining Sialon-containing composites in the SiC-B_4C-Si-Al-Al_2O_3 system by reaction sintering method with metallothermic and nitriding processes. *Ceramics and Advanced Technologies*, *20*, 2(40), 13–17.
14. Kovziridze, Z., Nijaradze, N., Tabatadze, G., Mestvirishvili, Z., & Darakhvelidze, N. (2019). Study of phase composition of composites in the SiC-B_4C-Si-Al-Al_2O_3 system. *Ceramics and Advanced Technologies*, *21*, 1(41), 44–51.
15. Kovziridze, Z. (2022). *Physics and kinetics of sintering* [Monograph]. Technical University Publishing House.
16. Griffith, A. A. (1920). The phenomena of rupture and flow in solids. *Philosophical Transactions of the Royal Society of London. Series A, Containing Papers of a Mathematical or Physical Character*, *221*(582-593), 163–198. https://doi.org/10.1098/rsta.1921.0006

17. Griffith, A. A. (1925). The theory of rupture. In *Proceedings of the First International Congress for Applied Mechanics (Delft, 1924)* (ed. J. Waltman, pp. 55-63). Delft.
18. Inglis, C. E. (1913). Stresses in a plate due to the presence of cracks and sharp corners. *Transactions of the Institution of Naval Architects*, *55*(1), 219–241.
19. Orowan, E. (1934). Die Festigkeitseigenschaften von Kristallen [The strength properties of crystals]. *Zeitschrift für Kristallographie - Crystalline Materials*, *A89*, 327–343.
20. Charles, R. J. (1958). Static fatigue of glass. I. *Journal of Applied Physics*, *29*(11), 1549–1553. https://doi.org/10.1063/1.1722991
21. Baker, T. C., & Preston, F. W. (1946). Wide range static strength testing apparatus for glass vials. *Journal of Applied Physics*, *17*(3), 170–178. https://doi.org/10.1063/1.1707700
22. Kovziridze, Z. (2018). *Formula for the dependence of macromechanical characteristics on the porous phase* (Sakpatenti Patent/ Certificate No. 7276, issued March 7, 2018). National Intellectual Property Center of Georgia.
23. Kovziridze, Z., Aneli, J., Nijaradze, N., & Tabatadze, G. (2017). *Ceramic and polymer composites* [Monograph]. Lambert Academic Publishing. ISBN: 978-620-2-06984-7.
24. Kovziridze, Z., Nijaradze, N., Tabatadze, G., & Aneli, J. (2016). *Ceramic and polymer composites* [Monograph]. Georgian Technical University. http://www.gtu.ge
25. Kovziridze, Z., Nijaradze, N., Tabatadze, G., & Darakhvelidze, N. (2017). *Sialon and low-tungsten composite materials* [Monograph]. Georgian Technical University. http://www.gtu.ge
26. Kovziridze, Z., Nijaradze, N., & Tabatadze, G. (2014). *High-power hetero-modulus composites* [Monograph]. Georgian Technical University. http://www.gtu.ge
27. Kollenberg, W. (2004). *Technische Keramik* [Technical Ceramics] (p. 52). Vulkan-Verlag ESSEN.
28. Kovziridze, Z., et al. (2017). Obtaining of SiAlON composite via metal-thermal and nitrogen processes in the SiC-Si-Al-geopolymer system. *Journal of Electronics Cooling and Thermal Control*, *7*(4), 103–122. https://doi.org/10.4236/jectc.2017.74009,

უაკ 666.762.93

მულტიფუნქციური კომპოზიტი B4C-SiC-TiC-TiB2-პერლიტის სისტემაში

ზ. კოვზირიძე, ნ. ნიჟარაძე, თ. ლოლაძე, ნ. ლოლაძე, გ. ტაბატაძე, თ. ჭეიშვილი, მ. მშვილდაძე

საქართველოს ტექნიკური უნივერსიტეტი. ბიონანოკერამიკისა და ნანოკომპოზიტური ტექნოლოგიების ინსტიტუტი, ბიონანოკერამიკული და ნანოკომპოზიტური მასალათმცოდნეობის ცენტრი. საქართველო, 0175, თბილისი, კოსტავას ქ. 69

E-mail: kowsiri@gtu.ge

რეზიუმე: მიზანი. მაღალი ტექნიკური და საექსპლუატაციო თვისებების მქონე კომპოზიტის მიღება B4C-SiC-TiC-TiB_2-პერლიტი სისტემაში.

მეთოდი. კომპოზიტის მიღება მოხდა ცხელი დაწნეხვის მეთოდით 1620^{0}C ტემპერატურაზე, 25 მპა წნევით, 50 წუთის განმავლობაში. დაყოვნება საბოლოო ტემპერატურაზე 10წთ. ფაზური და მიკროსტრუქტურული ანალიზები ჩატარდა რენტგენისა (DRON3), ელექტრონულ მიკროსკოპიული მეთოდებით, მექანიკური თვისებები განისაზღვრა გერმანული წარმოების გამგლეჯ მანქანაზე R-100 და სისალის საზომ როკველის ხელსაწყოზე.

შედეგები. მიღებულია კომპოზიტი სისტემაში B4C-SiC-TiC-TiB_2-პერლიტი, სადაც ცხელი წნეხვის პროცესში მოხდა ტიტანის კარბიდსა და ბორის კარბიდს შორის რეაგირება და წარმოიქმნა ტიტანის დიბორიდის მარცვლები, რამაც ხელი შეუწყო კომპოზიტის მექანიკური თვისებების მაღალი მაჩვენებლის მიღებას, გარდა ამისა პერლიტის თანაობისას კომპოზიტში წარმოქმნილი მინისებური მასა კარბიდების მარცვლებთან ქმნის ე.წ. ხიდებს და ესეც აუმჯობესებს მექანიკურ მაჩვენებლებს.

დასკვნა. მიღებული მასალა ხასიათდება მაღალი მექანიკური სიმტკიცით ღუნვაზე - 389 MPa და კუმშვაზე - 1923 MPa, ასევე საკმაოდ მაღალი დარტყმითი სიბლანტით - 11.2 KJ/M^2. მათი გამოყენება შესაძლებელია ცვეთამედეგ კვანძებში, მაღალი დარტყმითი სიბლანტის პირობებში და სხვა

საკვანძო სიტყვები: კომპოზიტი, კორელაცია, ფორიანი ფაზა, მექანიკური სიმტკიცე, სტრუქტურა.

UDC 621.9.02

THERMAL SHOCK RESISTANCE FORMULA FOR COMPOSITE MATERIALS

Z. Kovziridze

Institute of Bionanoceramic and Nanocomposite Technology Technical University of Georgia. GTU Center for Materials Science of Bionanoceramics and Nanocomposites. 69, Kostava Str., Tbilisi 0175, Georgia

E-mail: kowsiri@gtu.ge

Resume: Purpose. In the conditions of exploitation of ceramic materials and composites, not only high mechanical stresses, but also thermal loads and aerothermal shocks often develop. For example, on power lines, when spacecraft enter dense atmospheric layers, etc. These loads can significantly damage the structure. All materials have microcracks and may have them, at the tips of which during critical temperature shocks maximum stresses are generated, high energies are developed and the crack tip is torn off, which leads to the collapse of the product. Given such extreme working conditions, it is of interest to calculate those temperature energies, the ratio of the expansion coefficient between the phases, the values of porosity and modulus of elasticity,

which ensure the effective exploitation of the products. **Method.** Based on the exploitation conditions of the materials, their exploitation properties were studied using modern research methods. Based on the study and generalization of the micro- and macrostructural, micro- and macromechanical characteristics of ceramic materials, the parameters of the formula were selected. **Results.** The formula includes the thermal shocks applied to the product as a result of Analysis of the mechanisms of development of induced energies and the impact of these energies on the cracks in the material. The consequences of the activation of the mechanisms of propagation of the energies caused by these loads on the existing cracks and the energies developed in the product itself, which leads the material to a catastrophe. The positive role of closed pores in the product under the conditions of stresses arising during temperature loads is taken into account.

Conclusion. The formula we propose describes the process of transforming the energy developed as a result of thermal and gas thermal shocks on the product into internal energies in the product, which act on defects in the material, and this primarily works on the development of a crack, since when critical stress develops at its tip, the crack breaks off from the tip. As is known, maximum stresses develop at the crack tip during the accumulation of energy and its rupture occurs.

Key words: thermal shock, modulus of elasticity, coefficient of expansion, porosity, crack.

1. INTRODUCTION

The process of grain growth under conditions of thermal exposure can significantly influence the ultimate densification of a material during sintering. Typically, the densification associated with the diffusion process proceeds until porosity reaches approximately 10%. At this stage, rapid grain growth - secondary recrystallization occurs,

leading to a sharp decline in the densification rate. To achieve maximum density before the onset of this phenomenon, it is necessary to implement measures that inhibit secondary recrystallization. One highly effective approach is the introduction of finely dispersed additives into the composition. These additives distribute uniformly throughout the matrix and inhibit or retard grain boundary migration, thereby facilitating the elimination of residual pores [1-8].

2. MAIN PART

It is recognized that a comprehensive and exhaustive discussion regarding the influence of material composition, formulation, and microstructure on degradation is practically unattainable. For the majority of ceramic materials, the role of microstructure is primarily reduced to the effects of porosity. Existing pores reduce the effective cross-sectional area subjected to loading and act as stress concentrators. Specifically, for an isolated spherical pore, the stress concentration increases by a factor of two. Empirical evidence demonstrates that the strength of porous ceramics decreases exponentially with increasing porosity. A significant body of data is satisfactorily described by the Ryshkewitch equation:

$$\sigma=\sigma_0 \exp.(-nP) \qquad 1$$

Where n - is a constant whose value typically ranges from 4 to 7; P - is the volume fraction of porosity.

Consequently, it can be inferred that at 10% porosity, the strength of a material is approximately halved compared to its fully dense, pore-free state. For instance, hard porcelain typically exhibits a porosity of around 3%, whereas red clay products range between 10% and 15%; this discrepancy clearly accounts for the significant difference in mechanical strength between the two materials. However, pores can play a beneficial role when ceramic materials are subjected to high-stress gradients generated during thermal shock [9-12]. For example, when a spacecraft re-enters the dense layers of the atmosphere from space, external friction with the air causes the surface temperature to rise to 4,000–4,500°C for several seconds. To date, a material capable of withstanding such extreme temperatures for even a few minutes has not been developed. Composite materials used for aerospace shielding endure these temperatures for the brief duration required during the rapid deceleration of the craft, after which the temperature drops sharply.

A notable instance where porosity plays a beneficial role is in the application of ceramic composites under the high-stress gradients generated by thermal shock. In this context, pores can resist the inward propagation of cracks through the body of the component. While surface cracking may be observed, total structural fracture is averted. This occurs because the stress levels drop rapidly from their peak values at the surface toward the interior of the material.

Surface Tension and Surface Energy

It is well-established that ceramic materials and composites undergo brittle fracture. Given that brittle fracture necessitates the initiation and subsequent propagation of cracks, even within the 'ideal' materials that technologists strive to produce, it is essential to understand the mechanisms of microcrack formation. The causes are numerous. A critical aspect of brittle fracture is the inherent

difficulty in protecting the specimen surface from defect formation. For instance, the impact of solid particles on the surface of a newly fired component can induce dislocations within the crystal lattice. Such interactions often lead to the formation of microscopic surface cracks, as significant stresses are generated at the points of contact. Another primary source of microcracking in polycrystalline materials is the thermal expansion mismatch between constituent phases. This discrepancy generates localized stresses at the grain boundaries, subsequently leading to the initiation of fine cracks [13]. Microcrack initiation may also be attributed to residual stresses developed during the cooling process following firing, or to thermal stresses encountered during service, provided these stresses reach critical levels at the specimen surface. Such surface cracking is a common phenomenon. A distinct mechanism for stress concentration and crack initiation in multiphase ceramics is the formation of grooves at the interfaces between different phases, or along the boundaries of grains of the same phase, as a result of thermal etching.

In viscous liquids, shear stress dissipates through viscous flow; consequently, when the shape of such liquid changes under the influence of surface tension, no energy is expended on elastic deformation. As a result, surface tension and surface energy are numerically equivalent. This is not the case for crystalline solids, where surface tension is not equivalent to surface energy. Nevertheless, the equilibrium conditions for a surface subjected to surface forces can be determined, provided the deformation of the crystal's interior remains constant, assuming the solid is incompressible and undergoes no plastic deformation. The process is justified when the surface configuration evolves through mechanisms such as solubility, evaporation, surface diffusion, bulk diffusion, vacancy migration, and grain growth. Collectively, these phenomena drive the surface configuration toward a state defined by the minimum free surface energy. The creation of new surfaces requires the rupture or dissociation of interatomic bonds, which inherently increases the system's total energy. Generally, the surfaces of crystals with different crystallographic orientations exhibit varying surface energies; orientations that coincide with the most closely packed atomic planes possess the lowest energy and are, consequently, the most stable.

The Effect of Dopants

In a binary system, the distribution of components occurs in a manner that minimizes the total surface energy. For example, when TaC particles with a size of 2–3 μm are supplemented with SiC grains measuring 9–20 μm, whose surface energy in this case is lower than that of the tantalum carbide grains, the SiC grains preferentially concentrate at the surface. Consequently, the surface energy of the principal component, namely tantalum carbide, is correspondingly reduced. Conversely, if an additive possesses a higher surface energy, it tends to concentrate within the bulk of the material, resulting in a lower surface concentration and, therefore, a negligible effect on surface tension. Thus, the surface energy in a binary system varies non-linearly when transitioning from one end-member composition to another (Fig. 1). In Figure 1, the excess concentration of impurities at the surface is related to the change in the system's surface tension via the Gibbs Adsorption Isotherm:

$$G_2 = \approx \frac{dy}{RTdInc_2} \qquad 2$$

Where G_2 denotes the excess concentration of impurities at the surface per unit area.

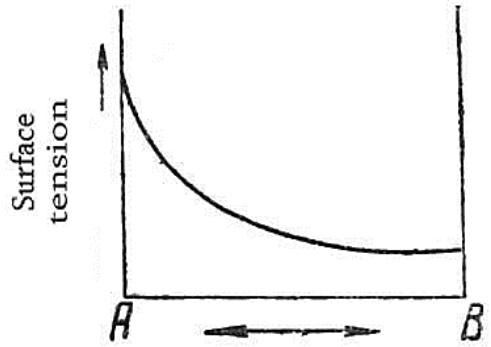

Fig. 1. Surface tension of a binary system

Materials characterized by high values of $G_2$are referred to as surface-active materials. If $G_2$is expressed in moles per square centimeter, this quantity may be determined, at low concentrations of the second component (c_2), from the dependence of the surface energy (γ)of the principal substance or material on the logarithm of the concentration of the second component, c_2.

Based on the above, for the manufacture of components in critical engineering applications, it is of great importance to use raw materials with a uniform and high degree of dispersity [14–19].

Magnitude of Surface Energy

The range of surface energy values observed in different materials is quite wide: approximately 72 erg/cm² for water at room temperature, and up to several thousand erg/cm² for materials such as diamond and silicon carbide (Table 1).

Table 1

Experimental values of surface energies of various materials in vacuum or inert gas atmosphere

Material	Phase	Temperature (°C)	Surface energy (erg/cm²)
Water	Liquid	25	72
Copper	Liquid	1120	1259
Copper	Solid	1100	1430
Silver	Liquid	1000	920
Silver	Solid	750	1140
Platinum	Liquid	1750	1865
B□O□	Liquid	900	80
Al□O□	Liquid	2080	700
Al□O□	Solid	1850	905
MgO	Solid	25	1000
TiC	Solid	1100	1190

The excess free energy of materials with a high specific surface area is sufficiently large to act as a driving force for a number of processes and is therefore of particular interest in ceramics. In particular, it is considered a primary factor responsible for the densification of pressed powders into dense final products during sintering.

Causes of microcrack formation

Since brittle fracture of a perfect material requires crack initiation and subsequent propagation, it is also essential to understand how microcracks are formed within materials. Of particular importance is the prevention of crack initiation on the surface of a component. In polycrystalline materials, a key factor is the difference in thermal expansion coefficients of the constituent phases, which leads to the development of stresses at grain boundaries. In many cases, these stresses become sufficiently high to initiate the formation of fine microcracks. Such processes also occur during cooling of specimens after firing, or during service due to thermal stresses, especially when their magnitude is high at the material surface. Similar defects may also develop in multiphase ceramic composites in the form of voids at the surface, either at interfaces between different phases or along grain boundaries of the same phase, as a result of thermal etching processes. The main cause of crack formation is mechanical surface damage and chemical corrosion [20–23]. In practice, it is difficult to neglect these factors; therefore, materials should be regarded as containing a certain number of defects. In some cases, brittle fracture or cracking is observed not only in brittle materials but also in ductile ones, for example under low-temperature conditions, impact loading, or when plastic deformation is suppressed. In such cases, some plastic deformation is observed prior to fracture. From a theoretical standpoint, fracture occurs due to microcracks formed by the coalescence of dislocations generated during plastic deformation, which leads to the onset of brittle fracture. Theoretical considerations indicate that dislocations tend to accumulate in large numbers at grain boundaries and surfaces, as well as at intersections of slip planes, where high stress concentrations arise. These stresses may be sufficient to cause the coalescence of several dislocations and the formation of a crack nucleus (Fig. 2). One example is the accumulation of dislocations at the intersection of two slip planes, leading to crack formation at crystal plane intersections (Fig. 3).

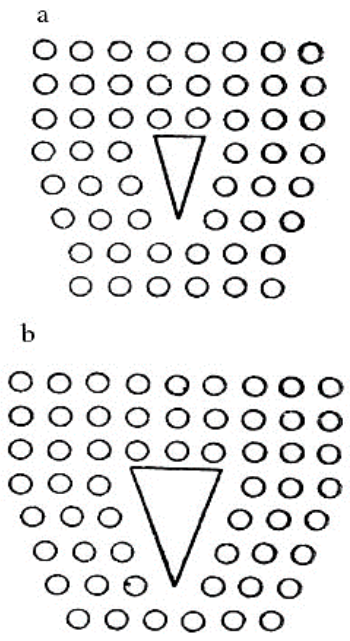

Fig. 2. Coalescence of dislocations leading to crack nucleation. a – two dislocations; b – three dislocations.

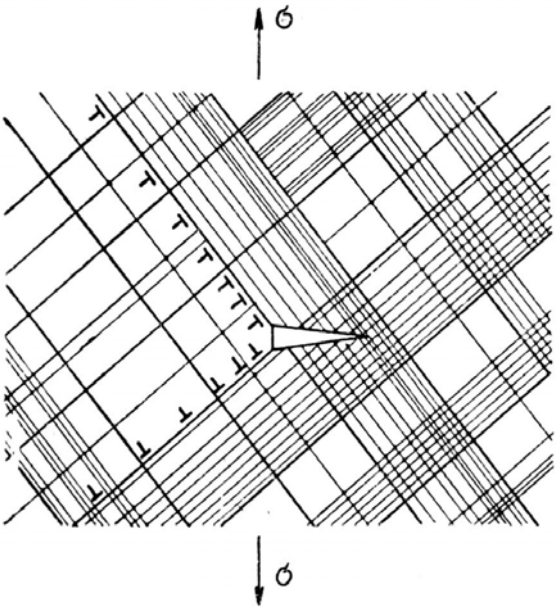

Fig. 3. Schematic representation of dislocation pile-up and crack formation at the intersection of two slip bands.

Theoretical calculations demonstrate that the coalescence of dislocations can occur even under conventional stress levels. During plastic deformation, if dislocations are generated rapidly, an increasing number of them flow into existing microcracks, causing steady, progressive growth. However, if dislocations are hindered by impurities or generated only under high stress, the microcracks may expand due to the stress concentration surrounding them, leading to cleavage, as is typical in brittle materials. In such brittle materials, the energy required for crack propagation is lower than the energy consumed during their formation via plastic deformation. Consequently, crack growth remains uninhibited and proceeds until final structural failure occurs under the same initial stress level. Thus, for brittle materials, the critical stage of failure is crack initiation.

The behavior differs for reinforced materials, such as carbides with metallic binders. In these systems, failure requires the initiation of new cracks at the phase boundaries, while the plasticity of the metallic phase necessitates the expenditure of significant energy and stress to drive further crack propagation. Such materials do not fail even when the applied stress exceeds the level required for crack initiation. For crack growth to continue toward complete failure in these cases, the stress must be increased to significantly higher values.

Elastic Deformation and Strength

The study of ceramic composite properties is complex because material failure under mechanical loading occurs not through a single simple mechanism across different materials and conditions, but rather through several distinct phenomena. Complexity also arises from the fact that the same material may fail in different ways depending on the magnitude of stress, the loading rate, the material's prehistory, environmental conditions, and temperature. Ignoring any of these factors, neglecting their simultaneous influence, or lacking knowledge of the failure mechanisms can lead an experimenter to significant errors.

Fracture processes

In general, brittle fracture of ceramics occurs through cleavage along specific crystallographic directions. At elevated temperatures, crystalline phases may also fail along grain boundaries, where shear stresses develop and intergranular cracks are formed. The presence of such cracks leads to localized stress intensification, which ultimately results in fracture.

As a consequence of applied tensile stresses, a local reduction in the cross-sectional area occurs, such that the nominal stress becomes lower than the actual stress acting on the material. As a result, the apparent tensile strength is lower than the real fracture-inducing stress (Fig. 4). The actual stress may be evaluated by accounting for changes in the specimen's cross-sectional area.

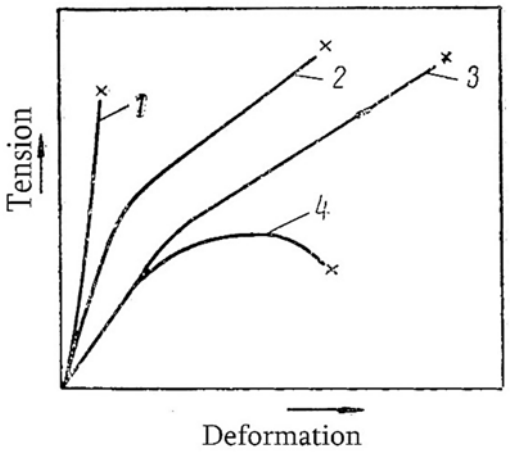

Fig. 4. Brittle and ductile fracture

1 – Brittle fracture; 2 – Ductile fracture under torsion testing; 3 – Same under tensile testing; 4 – Nominal tensile strength in fracture.

In ceramics and ceramic composites, static fatigue and subcritical crack growth are frequently observed. In such cases, fracture is associated with stress concentrations acting at crack tips, combined with accelerated corrosion at these locations. This type of degradation is highly sensitive to changes in the surrounding environment of the specimen [24–27].

Elastic deformation

Up to the proportional limit, the tensile stress is directly proportional to the relative elongation (Hooke's law):

$$\sigma=E\varepsilon \qquad 3$$

where E — is Young's modulus.

If a specimen is elongated under tensile loading, it is accompanied by a reduction in its thickness. This process is expressed as the ratio of the relative change in thickness to the relative change in length:

$$\mu=\frac{\Delta d/d}{\Delta l/l} \qquad 4$$

where d is the thickness and $\boldsymbol{l}$ is the length.

During the processes of plastic flow, viscous flow, and creep, the volume of the specimen remains constant and μ = 0.5. In the case of elastic deformation, Poisson's ratio varies from 0.2 to 0.3. Poisson's ratio is related to the modulus of elasticity and the shear modulus by the ratio:

$$\mu=\frac{E}{\Delta G}-1 \qquad 5$$

where E is the modulus of elasticity, and G is the shear modulus.

This relationship is valid for isotropic bodies, which possess a single modulus of elasticity regardless of the loading direction. For monocrystals (single crystals), this condition does not hold, whereas for polycrystalline ceramics, it serves as an excellent approximation. If a load is applied rapidly to the specimen, the deformation does not instantaneously recover to its equilibrium state, particularly at elevated temperatures.

Elastic Effect and Internal Friction

In the case of rapid loading, the deformation does not return immediately to its initial equilibrium state, particularly at elevated temperatures. In addition to the instantaneous deformation established in accordance with Hooke's law, a gradual increase in deformation is observed, referred to as the elastic effect, which is characterized as the deformation behavior of a standard linear solid.

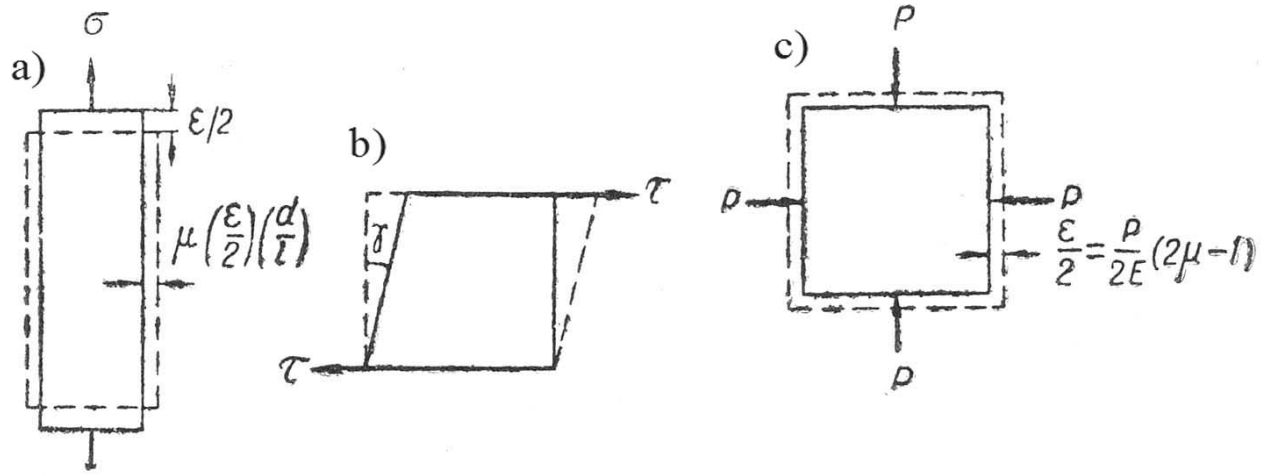

Fig. 5. Determination of Elastic Constants: (a) Young's modulus; (b) Shear modulus; (c) Bulk compression coefficient

The modulus of elasticity of such a body is defined as the ratio of stress magnitude to the total deformation magnitude. Upon application of the load, the instantaneously occurring deformation is determined by the dynamically non-relaxing modulus of elasticity:

$$E_{el.} = \sigma_0/\varepsilon_0 \qquad 6$$

where σ_0 is the magnitude of stress, and ε_0 is the total relative deformation.

Elastic Constants

The elastic elongation of a solid body corresponds to a uniform increase in interatomic distances and, consequently, is directly related to the nature and magnitude of the forces acting between atoms, as well as to the energy of the crystal lattice. In this regard, it is necessary to consider a reasonably satisfactory relationship that correlates the modulus of elasticity with the energy of the crystal lattice.

Crystals with a low coefficient of thermal expansion are characterized by a high modulus of elasticity (Figure 6). If no defects are present at the interfaces between phases, the deformation of each phase should be approximately identical, and the greater portion of the applied load is borne by the phase possessing the higher modulus of elasticity. Assuming equal values of Poisson's ratio for both phases, the overall modulus of elasticity is expressed by the following relationship:

$$E = E_1V_1 + E_2V_2 \qquad 7$$

where V_1 and V_2 are the volume fractions of the two phases.

The introduction of a second phase with a low modulus of elasticity into the material is equivalent to the presence of pores whose volumetric elastic modulus is practically zero. If the material has a Poisson's ratio of $\mu = 0.3$, then the modulus of elasticity in the case of closed porosity can be calculated using the following equation:

$$F = E_0 (1\ 1.9P + 0.9P^2) \qquad 8$$

where P is the porosity.

Figure 6 shows the dependence of the modulus of elasticity on the melting temperature of various materials.

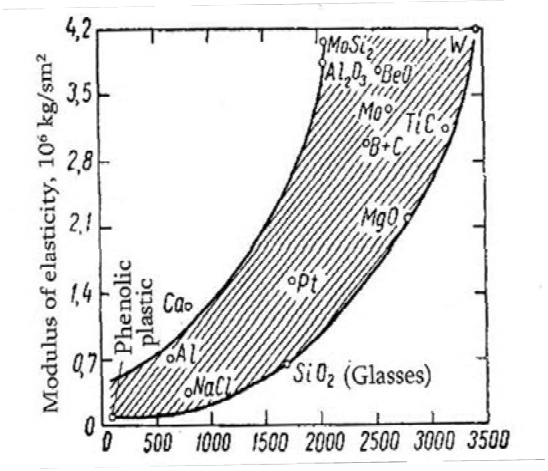

Fig. 6. Dependence of the modulus of elasticity on the melting temperature of various materials.

Figure 7 illustrates the variation of the elastic modulus of alumina oxide ceramic as a function of porosity.

Table 2 presents the values of the elastic modulus of ceramic materials.

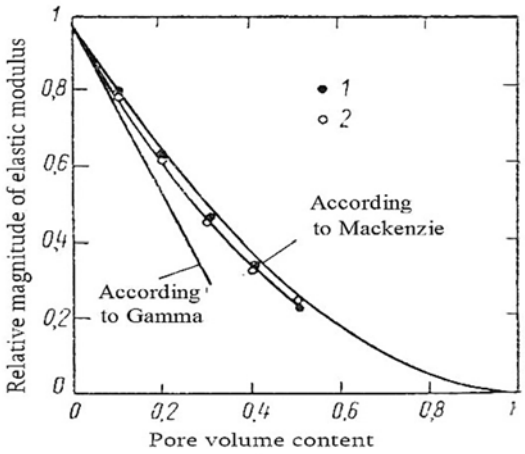

Figure 7. Variation of the elastic modulus of alumina oxide (Al_2O_3) ceramics as a function of porosity, according to P.L. Coble and W.D. Kingery (Coble R.L., Kingery W.D., *Journal of the American Ceramic Society*, 39, 377, 1956). 1 – elastic modulus; 2 – shear modulus.

With increasing temperature, the interatomic distances increase due to thermal expansion, and the force required to separate atoms decreases to some extent. In practice, the decrease in the modulus of elasticity with rising temperature is insignificant until the elastic effect becomes pronounced. The subsequent temperature range corresponds to the transition of the non-relaxing modulus of elasticity into a relaxing one. The magnitude of deformation during the elastic effect also depends on the frequency of mechanical vibrations and corresponds to new deformation mechanisms of the material under the action of stress [28–33].

The average strength of various ceramic composite materials varies within a wide range (up to 6×10^4 MPa for perfect, defect-free materials). Table 3 presents the flexural strength values of different ceramics

Table 2

Elastic modulus values of some ceramic materials (kg/cm²)

Material	Elastic modulus (kg/cm²)
Alumina oxide crystals	3.9 × 10□
Sintered alumina oxide (5% porosity)	3.7 × 10□
High-clay ceramics (90–95% Al□O□)	3.7 × 10□
Beryllium oxide ceramic (5% porosity)	3.2 × 10□
Boron nitride (hot-pressed, 5% porosity)	0.8 × 10□
Boron carbide (hot-pressed, 5% porosity)	3.0 × 10□
Graphite (20% porosity)	0.02 × 10□
Magnesium oxide ceramic (5% porosity)	2.1 × 10□
Spinel ceramic (5% porosity)	2.5 × 10□
Molybdenum silicide ceramic (5% porosity)	4.1 × 10□
Dense silicon carbide (5% porosity)	4.8 × 10□
Sintered titanium carbide (5% porosity)	3.2 × 10□
Stabilized zirconium dioxide ceramic (5% porosity)	1.5 × 10□
Quartz glass	0.74 × 10□
Pyrex glass	0.7 × 10□
Mullite porcelain	0.7 × 10□
Steatite ceramic	0.7 × 10□
High-grade fireclay refractory	1.0 × 10□
Magnesite refractory	1.8 × 10□
Silicon carbide on binder (20% porosity)	3.5 × 10□

Table 3

Flexural strength of some ceramic materials (MPa)

Material	Flexural strength (MPa)
Alumina oxide crystals	350–1000
Sintered alumina oxide	210–350
High-clay ceramics (90–95% Al□O□)	350
Beryllium oxide ceramic (5% porosity)	140–280
Boron nitride (hot-pressed, 5% porosity)	50–100
Boron carbide (hot-pressed, 5% porosity)	350
Magnesium oxide ceramic (5% porosity)	100
Molybdenum disilicide ceramic (5% porosity)	700
Spinel ceramic (5% porosity)	85
Dense silicon carbide (5% porosity)	1100
Stabilized zirconium dioxide ceramic (5% porosity)	84
Quartz glass	109
Pyrex glass	79
Mullite porcelain	70
Steatite ceramic	140

Static fatigue

The fracture behavior of oxide ceramics, in addition to their inherent brittleness, is characterized by the fact that their measured strength depends on the duration of loading and the rate at which the load is applied (Figure 8). In general, ceramic materials and ceramic composites can withstand high loads for short periods of time; however, under long-term loading their strength decreases significantly. Accordingly, the experimentalist must take into account the influence of the loading rate on the material behavior. It has been found that static fatigue occurs in humid environments. The chemical nature of this process is also reflected in the temperature dependence of static fatigue. The strength under short-term loading at room temperature is equivalent to the strength observed under long-term loading at significantly lower temperatures.

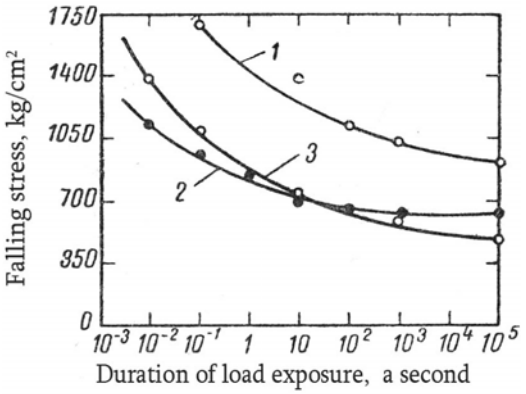

Figure 8. Dependence of fracture stress on loading time according to Baker and Preston. 1 – quartz glass (humid); 2 – porcelain (dry); 3 – sodium–calcium silicate glass (humid).

Thermal Expansion and Thermal Stresses

In homogeneous and isotropic composite materials, no stresses, or only negligible stresses, are generated during thermal expansion. However, if the material is rigidly constrained and prevented from expanding, significant stresses develop within it. At the same time, these stresses are equivalent to those that would arise if the specimen were allowed to expand freely and then subsequently compressed by external forces back to its original dimensions. The force required for this process is proportional to the material's modulus of elasticity and the magnitude of elastic strain, which, in turn, is equal to the product of the thermal expansion coefficient and the temperature difference between the initial and final states. In the case of such thermal and mechanical stresses, the presence of closed porosity in the matrix, as well as its distribution, size, and shape, play an important role.

Thus, in the presented formulation, we obtain:

$$\sigma = \frac{Ea\left(T - T_0\right)}{P} \qquad 9$$

where E is the modulus of elasticity (kg/cm² × 10^6); a is the coefficient of linear thermal expansion (×10^{-6}); T is the initial temperature (°C); T_0 is the final temperature (°C); P is the closed porosity of the material (wt%), ranging from 0.1 to 5%.

3. CONCLUSION

The porosity value is selected for ceramic composite materials in cases where the product is required to exhibit maximum mechanical properties, while also taking into account the beneficial role of pores under conditions of thermally induced stresses. This is particularly important under high thermal gradients, where pores can help to dissipate the energy generated by dislocations and crack formation. According to a number of studies, the mechanical properties of the material deteriorate significantly when the porosity exceeds 8–9 wt.%. Therefore, in our opinion, the porosity in the material should not exceed 5 wt.% in order to preserve the high operational properties obtained through processing, while still allowing pores to play a positive role in stress relaxation under thermal loading

The inclusion of porosity in the denominator is justified by the fact that, under high mechanical stresses or thermal shock conditions, closed pores, when uniformly distributed within the matrix and having an approximately equiaxed shape with sizes below 5 μm, facilitate stress relaxation and hinder the accumulation and concentration of energy associated with stress development. In general, resistance of composites to thermal shock requires a sufficiently uniform degree of dispersion within the matrix, so that stresses at phase and grain boundaries are minimized under thermal shock conditions. As a result, the material becomes more suitable for reliable long-term performance under severe operating conditions. In structural analysis, particular importance is given to data on the volumetric fractions of phases present in the material, since each phase is characterized by its own specific operational properties. The coexistence of such phases must be well balanced to ensure their stable performance under service conditions. In this context, the real particle size distribution within the matrix plays a crucial role, as it directly influences the operational properties of the composite material [20–21].

REFERENCES

1. Introduction to ceramics – D. Kingery, Publishing House of Construction Literature, Moscow, 1967, pp. 254-264.
2. Grathwohl G. (Herausgeber). Mechanische Eigenschaften keramischer Konstruktions werkstoffe. ISBN 3-88355-194-5. DGM Information gesellschaft mbh. 1993.
3. Kingery W.D, editor. Kinetics of High-Temperature Processes, part IV, Technology Press. Cambridge. Massachusetts and John Willey and Sons, New York; 1959.
4. Mackenzie J.K. and Shuttleworth R.A. Phenomenological Theory of Sintering, Proc. Phys. Soc. London, Book 62. 833, 1949.
5. Burke J.E. The Role of Grain Boundaries in sintering J. Amer. Ceram. Soc. 40, 80, 1957.
6. Ceramic Fabrication Processes, edited by W. D. Kingery. Vol. IV, 1960.
7. Kingery W. D., J. Appl. Phys., 30, 301, 1959.
8. Sune S.C., Cook R. L.. Am. Ceram. Soc., 34, 145, 1951
9. Z. Kovziridze.-Macro-mechanical properties-porous phase dependence formula. Georgian Patent. "Saqpatenti". Certificate 7276. 2018.03.07.
10. Z. Kovziridze, Mechanical Modulus of Materials National Intellectual Property Center of Georgia "Sakpatenti" Certificate of Deposit 7136 10/11/2017.
11. Budworth D. W.-Theory of pore Closure during sintering. Trans. Britt. Ceram. Soc. v.69, 1970, p. 29-31.
12. Burggraf A. I. Korngroesse. Korngroessenverteilung und Korngrenzen im Zusammenschaften 27. 1977. IV. 6. s.102-114.
13. Hans Walter Hennicke, Friedrich Yakovlevich Kharitonov, Zviad Davidovich Kovziridze. Barium-Containing Electroceramics Resistant to Thermal Shocks. Monograph. Tbilisi University Press, Tbilisi, Georgia. 1992.
14. Griffith A.A. Phil. Trans.Roy. Soc. London. A221. 163.1920. First International Congress for Applied Mechanics (Delft). 1924. ed.J. Waltman Delft 1925.
15. Griffith A.A. Phil.Trans. Roy. Soc. London. A221. 163. 1920.
16. Inglis C.E. Trans. Inst. Nav. Archit. 55. 1. 219. 1913.
17. Orowan E. Z. Krist. A89. 327. 1934.
18. Charles R.J. Journ. Appl. Phys. 29. 1549. 1958.
19. Baker T.C. Preston F. W. Journ. Appl. Phys. 17. 170. 1946.
20. Fullman R. L. Trans Amer. Journal M.E., 197, 447, 1953.
21. Cahn J. W., Fullman R. L. Metals, 8, 610, 1956.
22. Herring C. – in: The physics of powder metallurgy/Ed. Kingston W.E. – N.Y.:Mc Grow-Hill. 1951. P. 143.
23. Klein G.A., Krakhmalov V.A. - Crystallography. 1967. Vol. 12. p. 1096.
24. Munz D. Fett T. Ceramics: Mechanical Properties, Failure Behaviour, Materials Selection,, ISBN 3-540-65376-7, Springer-Verlag Berlin Heidelberg, New-York, 1999.P. 61.
25. Helga Gollisch-Szibov-zum Zusammensetzung der Gefuegedaten und mechanischen Eigenschaften Von Porzellan. Doktor Arbeit. 1979, Clausthal, p. 3-117.
26. Zviad Kovziridze, Jimsher Aneli, Natela Nijaradze, Gulnazi Tabatadze. Ceramic and Polymer Compozites. Monograph. LAMBERT

Academic Publishing. Germany. International Book Market Service LTD. Member of OmniScriptum Publishing Group. 17 Meldrum Street, Beau Bassin. 71504. Mauritius. 1917. P. 198-208.

27. Z. Kovziridze, I. Heinrich, N. Nijaradze – Study of preparation and Effect of Si20N2 Phase on the Properties of SiC composite. 4th International Congress on Ceramics. Chicago. Illinois. USA. July 15-19. 2012. P.75. Baker T.C. Preston F.W. Journ. Appl. Phys., 17, 170, 1946.
28. Landau L.D., Lifshitz I.M. Theory of Elasticity – Moscow, Nauka. 1967
29. Lifshitz, I.M., Geguzin, Ya. E., *Fizika Tverdogo Tela* (Solid State Physics), 1965, Vol. 7, p. 62.
30. Strelov, K.K., *Structure and Properties of Refractories*. Moscow: Metallurgiya, 1972, p. 216.
31. Zviad Kovziridze, Hans Walter Hennicke, Fridrich Kharitonov. Thermomechanics of Ceramics. Monograph. Fachhochschule Karlsruhe Hochschule fuer Technik. Karlsruhe. Germany. 1998.
32. Hennicke, Hans-Walter; Kharitonov, Friedrich Yakovlevich; Kovziridze, Zviad Davidovich. *Barium-Containing Electroceramics Resistant to Thermal Shock*. Monograph. Tbilisi University Press: Tbilisi, Georgia. 1992.
33. W. Kollenberg. Technische Keramik. Vulkan-Verlag Essen. Germany. S.21- 68. 2004.
34. Z. Kovziridze - The Formula of Dependence of Mechanical Characteristics of Materials on Crystalline Phase Composition in the Matrix. Advances in Materials Physics and Chemistry, Impact Factor. 2020, V.10.# 8. P. https://www.scirp.org/journal/ampc USA Delaware.

უაკ 621.9.02

კომპოზიციური მასალების თერმული დარტყმის წინააღმდეგობის ფორმულა

ზ. კოვზირიძე

საქართველოს ტექნიკური უნივერსიტეტი, ბიონანოკერამიკისა და ნანოკომპოზიტების ტექნოლოგიის ინსტიტუტი, სტუ ბიონანოკერამიკისა და ნანოკომპოზიტების მასალათმცოდნეობის ცენტრი. თბილისი. კოსტავას 69. საქართველო

E-MAIL: kowsiri@gtu.ge

რეზიუმე: მიზანი. კერამიკული მასალებისა და კომპოზიტების ექსპლუატაციის პირობებში ხშირად ვითარდება არა მხოლოდ მაღალი მექანიკური დაძაბულობები, არამედ თერმული დატვირთვები და აეროთერმული შოკები. მაგალითად, ელექტროგადამცემ ხაზებზე, როდესაც კოსმოსური ხომალდები შედიან მკვრივ ატმოსფერულ ფენებში და ა.შ. ამ დატვირთვებს შეუძლიათ მნიშვნელოვნად დააზიანონ სტრუქტურა. ყველა მასალას აქვს მიკრობზარები და

შეიძლება ჰქონდეს ისინი, რომელთა წვერებზე კრიტიკული ტემპერატურული შოკების დროს წარმოიქმნება მაქსიმალური დაძაბულობა, ვითარდება მაღალი ენერგიები და ბზარის წვერი იშლება, რაც იწვევს პროდუქტის კოლაფსს.

ასეთი ექსტრემალური სამუშაო პირობების გათვალისწინებით, საინტერესოა იმ ტემპერატურული ენერგიების, ფაზებს შორის გაფართოების კოეფიციენტის თანაფარდობის, ფორიანობისა და ელასტიურობის მოდულის მნიშვნელობების გამოთვლა, რომლებიც უზრუნველყოფენ პროდუქტების ეფექტურ ექსპლუატაციას.

მეთოდი. მასალების ექსპლუატაციის პირობების საფუძველზე, მათი ექსპლუატაციის თვისებები შესწავლილი იქნა თანამედროვე კვლევის მეთოდების გამოყენებით. კერამიკული მასალების მიკრო- და მაკროსტრუქტურული, მიკრო- და მაკრომექანიკური მახასიათებლების შესწავლისა და განზოგადების საფუძველზე შეირჩა ფორმულის პარამეტრები.

შედეგები. ფორმულა მოიცავს პროდუქტზე განხორციელებულ თერმულ შოკებს, რომლებიც გამოწვეულია ინდუცირებული ენერგიების განვითარების მექანიზმების ანალიზით და ამ ენერგიების ზეგავლენით მასალაში ბზარებზე. ამ დატვირთვებით გამოწვეული ენერგიების გავრცელების მექანიზმების გააქტიურების შედეგები არსებულ ბზარებზე და თავად პროდუქტში განვითარებული ენერგიები, რაც მასალას კატასტროფამდე მიჰყავს. გათვალისწინებულია პროდუქტში დახურული ფორების დადებითი როლი ტემპერატურული დატვირთვების დროს წარმოქმნილი სტრესების პირობებში.

დასკვნა. ჩვენს მიერ შემოთავაზებული ფორმულა აღწერს პროდუქტზე თერმული და გაზის თერმული დარტყმების შედეგად წარმოქმნილი ენერგიის პროდუქტში არსებულ შინაგან ენერგიებად გარდაქმნის პროცესს, რომლებიც მოქმედებენ მასალის დეფექტებზე და ეს, პირველ რიგში, ბზარის განვითარებაზე მოქმედებს, რადგან როდესაც მის წვერზე კრიტიკული დაძაბულობა ვითარდება, ბზარი წვერიდან იშლება. როგორც ცნობილია, ენერგიის დაგროვების დროს ბზარის წვერზე მაქსიმალური დაძაბულობა წარმოიქმნება და ხდება მისი გახეთქვა.

საკვანძო სიტყვები: თერმული დარტყმა, ელასტიურობის მოდული, გაფართოების კოეფიციენტი, ფორიანობა, ბზარი.

UDC 666.762.93

SYNTHESIS AND CHARACTERIZATION OF β SiAlON-SiC COMPOSITES BASED ON NATURAL ALUMINOSILICATES

Z. Kovziridze, M. Mshvildadze, N. Kutsiava, T. Loladze, T. Tsilosani, N. Nizharadze, G. Tabatadze, M. Kapanadze, M. Balakhashvili, N. Darakhvelidze, V. Qinqladze

Institute of Bionanoceramic and Nanocomposite Technology Technical University of Georgia. GTU Center for Materials Science of Bionanoceramics and Nanocomposites. 69, Kostava Str., Tbilisi 0175, Georgia

E-mail: kowsiri@gtu.ge

Resume: Objective. The paper investigates the synthesis and structural properties of β-SiAlON composites obtained within the Si-SiC-Al system via the nitridation method, utilizing natural aluminosilicates (perlite, kaolin). **Method.** Structural properties were investigated using X-ray diffraction (XRD) analysis and scanning electron microscopy (SEM). Micro- and macromechanical properties were also evaluated. **Results.** It was established that a robust SiAlON matrix is formed within the temperature range of 1300–1500°C. A self-reinforced microstructure was obtained. Physico-mechanical testing demonstrated that at 1500°C, the composite is characterized by zero open porosity and high density (3.21 g/cm³). **Conclusion.** The obtained materials are promising for high-temperature and erosive environments.

Key words: β-SiAlON, silicon carbide, composite, structure, aluminosilicate.

1. INTRODUCTION

This article addresses the synthesis of SiAlON-containing composite materials within the Si-SiC-Al system via the nitridation method. The novelty of the research lies in the integration of natural materials: kaolin, clay, and perlite into the starting mixture, aiming at the structural modification of the composite. The paper analyzes the influence of the nitridation process on the phase composition and evaluates the physico-technical characteristics of the resulting material in comparison with traditional counterparts.

One of the primary challenges in modern materials science is the optimization of the fabrication process and the cost reduction of high-tech ceramic composites [1-6]. SiAlON-type systems are distinguished by unique mechanical and thermal properties; however, their synthesis often requires expensive raw materials and a complex technological cycle. This paper discusses an alternative approach for fabricating SiAlON-containing composites within the Si-SiC-Al system, utilizing natural aluminosilicate raw materials - kaolin, clay, and perlite in the synthesis process. The objective of the research is to obtain a material via the nitridation method that retains high performance characteristics while simultaneously remaining resource-efficient.

The utilization of natural aluminosilicates (kaolin, clay, perlite) significantly reduces both the

energetic barrier required for synthesis and the cost of the product. This approach aligns with the principles of modern "green ceramics," which entail the substitution of expensive synthetic powders with accessible, local resources while minimizing negative environmental impact.

The formation of SiAlON phases within the Si-SiC-Al system is a complex physicochemical process that depends directly on the composition of the starting components and the parameters of the reaction environment. The nitridation method enables the formation of a robust crystalline structure under controlled synthesis conditions [7-14]. The present article investigates the influence of natural additives, specifically kaolin, clay, and perlite, on the phase transformations and the microstructure of the final product. The incorporation of kaolin and perlite into the system not only alters the reaction kinetics but also promotes the formation of a composite with specific properties, thereby expanding its application range under extreme conditions.

The nitridation process within the Si-SiC-Al system, in the presence of natural additives, promotes the activation of the reaction bonding mechanism. The oxide phases released as a result of the thermal decomposition of perlite and kaolin actively participate in the formation of a complex oxynitride matrix, which accounts for the high density and thermal shock resistance of the material.

The objective of the present work is to determine the optimal ratio between Si-SiC-Al and natural mineral additives in order to obtain a SiAlON-containing composite with enhanced mechanical properties

2. MAIN PART

Within the framework of the study, it was demonstrated that the controlled introduction of additives enables regulation of the pore structure and phase composition of the composite, which ultimately determines the operational reliability of the obtained sialon-containing material in aggressive environments.

The scientific novelty of the research lies in the integration of natural materials, kaolin, clay, and perlite, into the starting mixture, aiming at the structural modification of the composite. The paper analyzes the influence of the nitridation process on the phase composition and evaluates the physico-technical characteristics of the resulting material in comparison with traditional counterparts. One of the primary challenges in modern materials science is the optimization of the fabrication process and the cost reduction of high-tech ceramic composites [1-6].

SiAlON-type systems are distinguished by unique mechanical and thermal properties; however, their synthesis often requires expensive raw materials and a complex technological cycle. For the research, aluminum powder, silicon, and silicon carbide powders were utilized, along with minor additives of magnesium and yttrium oxides to intensify the sintering process. The mineral additives selected were raw mineral materials available in Georgia, which contain the necessary elements for SiAlON formation: Makvaneti kaolin (extracted in the Ozurgeti municipality, near the village of Makvaneti; a high-quality, white kaolin containing the mineral kaolinite), Macharula refractory clay (extracted in Imereti, specifically the Kharagauli municipality; a traditional, plastic

clay), and Paravani perlite (extracted in the area adjacent to Lake Paravani, Javakheti; a glass of volcanic origin). Table 1 presents the material composition of the investigated composites.

Table 1

Material composition of the composites

Composite Number	Material composition of the composites							
	Kaolin	Refractory Clay	Perlite	Al	SiC	Si	MgO	Y_2O_3
1	12	11	3	22	25	25	0,92	1,8
2	9	14	3	22	25	25	0,92	1,8
3	9	14	3	20	27	25	0,92	1,8
4	13	7	4	24	27	25	0,92	1,8

The research was conducted in two stages. The objective of the first stage was to obtain the SiAlON-containing material and to investigate the progression of the nitridation process. In the second stage, the SiAlON-containing material obtained at 1300°C was comminuted, and the samples were pressed at various temperatures using the hot-pressing method to achieve a compact material and evaluate its properties. In the first stage, the components were weighed on an analytical balance according to the compositions specified in Table 1, blended, and milled in an attritor to achieve a particle size of less than 1 μm. The prepared batch was then dried in a thermostat to the required moisture content, and the samples were molded. At the next stage, the samples were nitrided at different temperatures in order to determine the dynamics of sialon formation. After holding for 30 min at the selected temperature, the sintered samples were crushed, ground into fine powder, and prepared for X-ray phase analysis. The results of the X-ray phase analysis are presented in Fig. 1.

The figure clearly illustrates the dynamics of phase transformations with increasing temperature (from 1000°C to 1300°C). The X-ray diffraction patterns show the transformation of the initial components into sialon phases. At lower temperatures (1000°C), distinct peaks corresponding to free Si and Al are observed. Silicon carbide (SiC) remains stable, while kaolinite and perlite undergo dehydration, leading to the formation of amorphous phases.

As the temperature increases (1100-1200^{0}C), the nitridation of Si and Al initiates, accompanied by the nucleation of silicon nitride (α and β Si_3N_4) and aluminum nitride AlN.

At elevated temperatures (1300°C), the formation of β-SiAlON occurs. The peaks observed in the regions of d□□□ = 3.130, 2.665, and 2.324 Å indicate the formation of a complex oxynitride lattice. The presence of Al in the system "substitutes" Si atoms within the Si_3N_4 lattice, leading to the formation of sialon.

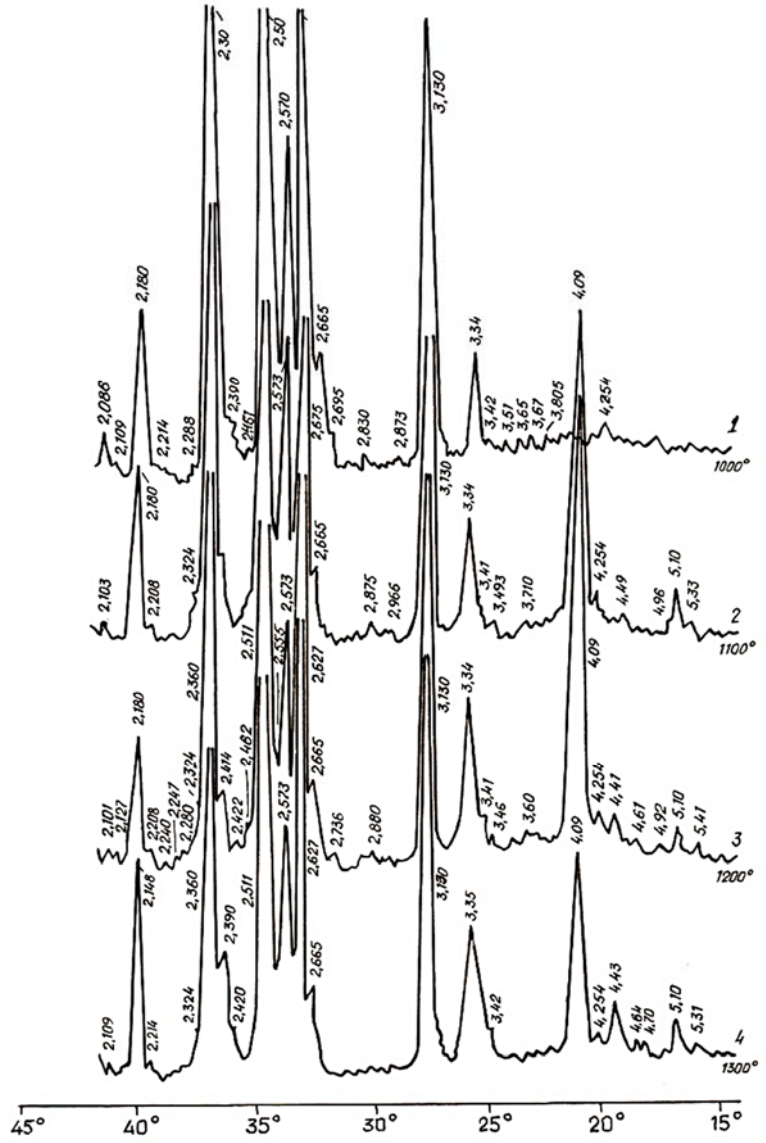

Fig. 1. Dynamics of SiAlON formation

The curve obtained at 1300°C (curve 4) indicates that the process is complete and a rigid structural framework has been formed. The formation of β-SiAlON and the peaks corresponding to d = 3.130, 2.665, and 2.324 Å confirm the presence of the sialon phase. This indicates that during the nitriding process, Al and O atoms substituted into the Si_3N_4 lattice. The role of SiC should also be emphasized. The silicon carbide peaks remain stable throughout the entire temperature range, indicating that SiC does not participate directly in the reaction but rather acts as a reinforcing phase, enhancing the crack resistance of the composite.

The addition of perlite and clay at lower temperatures promotes the formation of a certain amount of eutectic melt (glass-like phase). This "liquid bridge" accelerates nitrogen diffusion and stimulates the growth of silicon nitride and sialon crystals. Aluminum powder not only serves as a

constituent of sialon but, upon melting above 660 °C, also creates a reactive medium that facilitates the nitriding of silicon.

The characteristic peaks of the natural raw materials are no longer directly observed in the diffraction pattern. The absence of individual peaks characteristic of kaolin and perlite at 1300 °C is particularly significant, as it indicates their complete thermal decomposition and the full integration of their constituent oxides (SiO_2 and Al_2O_3) into the sialon matrix.

According to the results of the X-ray phase analysis, the principal phase transformations in the Si–SiC–Al system in the presence of natural additives are completed at 1300 °C. The diffraction pattern reveals distinct maxima corresponding to β-SiAlON-type solid solutions. The significant decrease in the intensity of the initial component peaks (free Si and Al), together with the growth of new nitride phases, indicates a high degree of nitriding. The incorporation of perlite and kaolin into the system promotes the reaction-bonding process, resulting in the formation of a homogeneous and densely bonded structure in the final product.

Among the investigated composites, the composition of composite #4 was considered optimal, and further studies were carried out on this material. As demonstrated by the study, the final formation of the sialon lattice is most intensive at 1500 °C with a holding time of 30 minutes, which is clearly confirmed by the phase analysis of this composite.

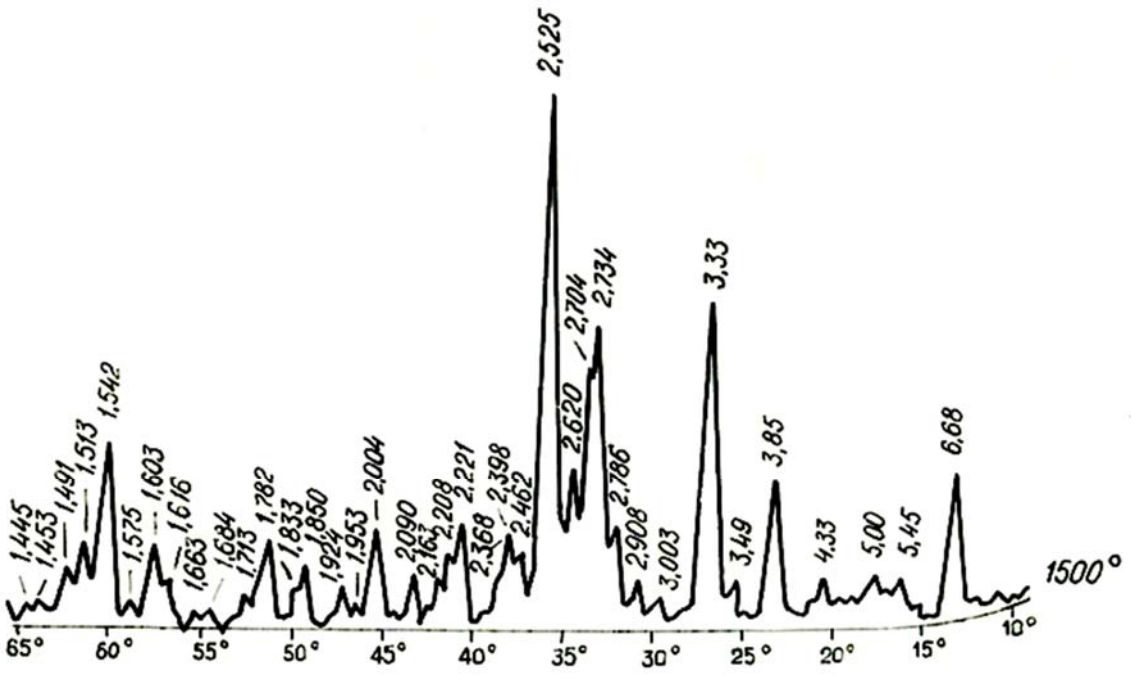

Fig. 2. X-ray of N4 Composite

Figure 2 demonstrates the formation of a fully developed high-temperature phase composition. Compared with the previous pattern obtained at 1300°C, the peaks are significantly sharper, indicating a higher degree of crystal lattice ordering and structural perfection.

The major peaks observed in the diffraction pattern indicate that the matrix of the system is predominantly composed of β-SiAlON. The characteristic peaks at d = 3.33, 2.525, and 2.704 Å (together with several minor peaks within the 40–60° interval) directly correspond to the sialon structure. The increase in temperature to 1500 °C resulted in the maximum substitution of Al and O atoms into the β-Si_3N_4 lattice, leading to the formation of a solid solution with high chemical stability and corrosion resistance. Regarding SiC (silicon carbide), the peak in the vicinity of d = 2.525 Å is highly intense. In this region, overlapping of the β-SiAlON and β-SiC peaks occurs. Silicon carbide retains its crystalline structure without decomposition and forms the "skeleton" of the composite, thereby ensuring high refractoriness and mechanical strength of the material.

The minor peaks at d = 6.68, 4.33, and 3.85 Å indicate that the oxides derived from the natural additives form complex aluminosilicate phases, such as mullite-type structures or cristobalite. The liquid phase formed with the participation of perlite and clay at 1500 °C becomes fully crystallized or incorporated into the solid solution, thereby filling the interparticle spaces and reducing the porosity of the material.

The X-ray phase analysis of the sample obtained at 1500 °C (Fig. 2) demonstrated that the formation of the β-SiAlON phase in the system was completed. The diffraction pattern clearly exhibits diffraction maxima characteristic of sialon solid solutions (d = 3.33, 2.525, 1.542 Å, etc.). It should be noted that the intensity of the peaks increases with increasing temperature, indicating a high degree of crystallinity of the material. The liquid phase formed on the basis of the natural additives (perlite and kaolin) promotes particle sintering and the formation of a strong ceramic matrix in which SiC dispersed particles are uniformly distributed. The resulting phase composition determines the high service performance of the composite under extreme thermal conditions.

The results of the electron microscopic investigation of the microstructure are presented in Fig. 2(a–d). At a magnification of ×1000, the material appears sufficiently dense and homogeneous. No large pores or cracks are observed, indicating effective sintering in the presence of natural additives (perlite and clay). The microstructure of the developed composite (Fig. 2) is characterized by high homogeneity and density.

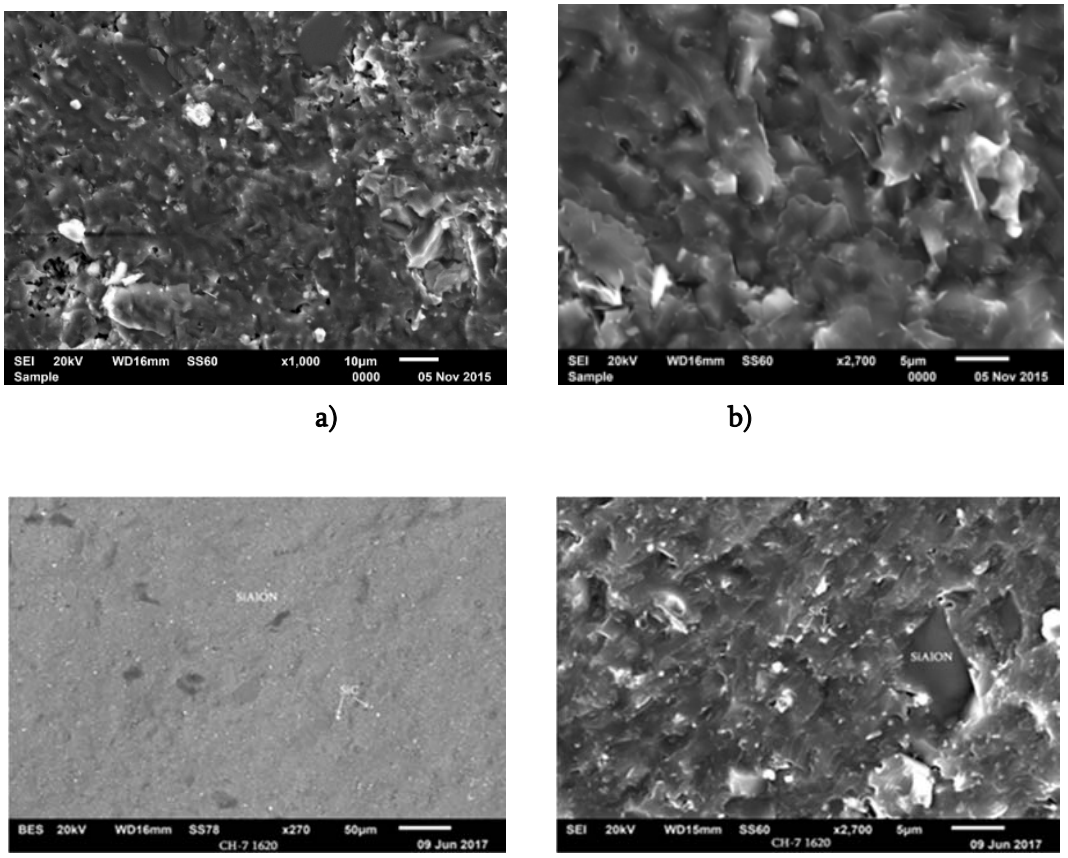

a) b)

c) d)

Fig. 2. Microstructure of the composite at different magnifications: (a) ×1000, (b) ×2700, (c) ×270, (d) ×2700.

The surface morphology confirms the efficiency of the reaction-sintering process, during which the initial powder mixture was transformed into a dense monolithic structure. At higher magnification (×2700), the morphology of β-SiAlON and SiC phases becomes clearly distinguishable. The composite matrix consists of elongated prismatic or needle-like crystals intertwined with one another, which is characteristic of the reinforced β-SiAlON microstructure. These interlocked "needle-like" crystals are responsible for the high strength and fracture toughness of the material. The space between the sialon crystals is filled with a glass-like aluminosilicate phase formed during the thermal treatment of the natural additives (kaolin and perlite). This liquid-derived phase acts as a bonding medium, ensuring the high density of the composite. A small amount of residual porosity is observed in the samples. The isolated nature and low volume fraction of the pores indicate that the glassy phase generated during the thermal decomposition of kaolin and perlite effectively fills the intercrystalline spaces during synthesis. The electron microscopic analysis of the fracture surface of the samples (Fig. 3) demonstrates that the fracture behavior of the material is predominantly brittle. Distinct crystallite facets are visible on the fracture surface, indicating high local strength. However, the presence of elongated sialon crystals and dispersed SiC particles promotes

crack deflection mechanisms, thereby increasing the fracture toughness of the material and preventing catastrophic instantaneous failure. Unlike metals, the contribution of plastic deformation to fracture is practically absent; nevertheless, the brittle fracture is "controlled" and "complex" due to the reinforced microstructure, which represents a highly favorable characteristic for ceramic materials.

The energy-dispersive spectroscopic (EDS) analysis (Fig. 4a - f) revealed a non-uniform yet systematic distribution of elements within the composite structure. The data obtained from Spectrum 2, characterized by high concentrations of N, O, Al, and Si, unequivocally confirm the formation of the sialon matrix. The participation of natural aluminosilicates in the synthesis process is evidenced by Spectrum 3, which is dominated by oxide phases. This positively affects the mechanical properties of the material, particularly its microhardness and refractoriness.

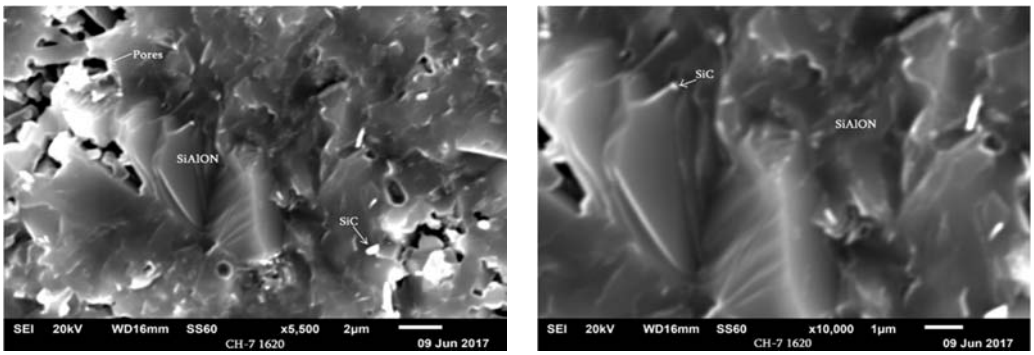

a) b)

Fig. 3. Electron microscopic analysis of the fracture surface of the samples: (a) ×5500, (b) ×10 000.

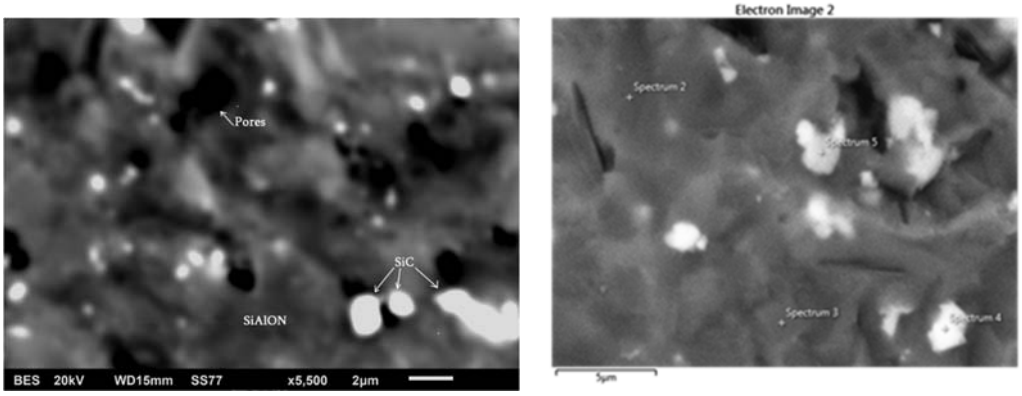

a) b)

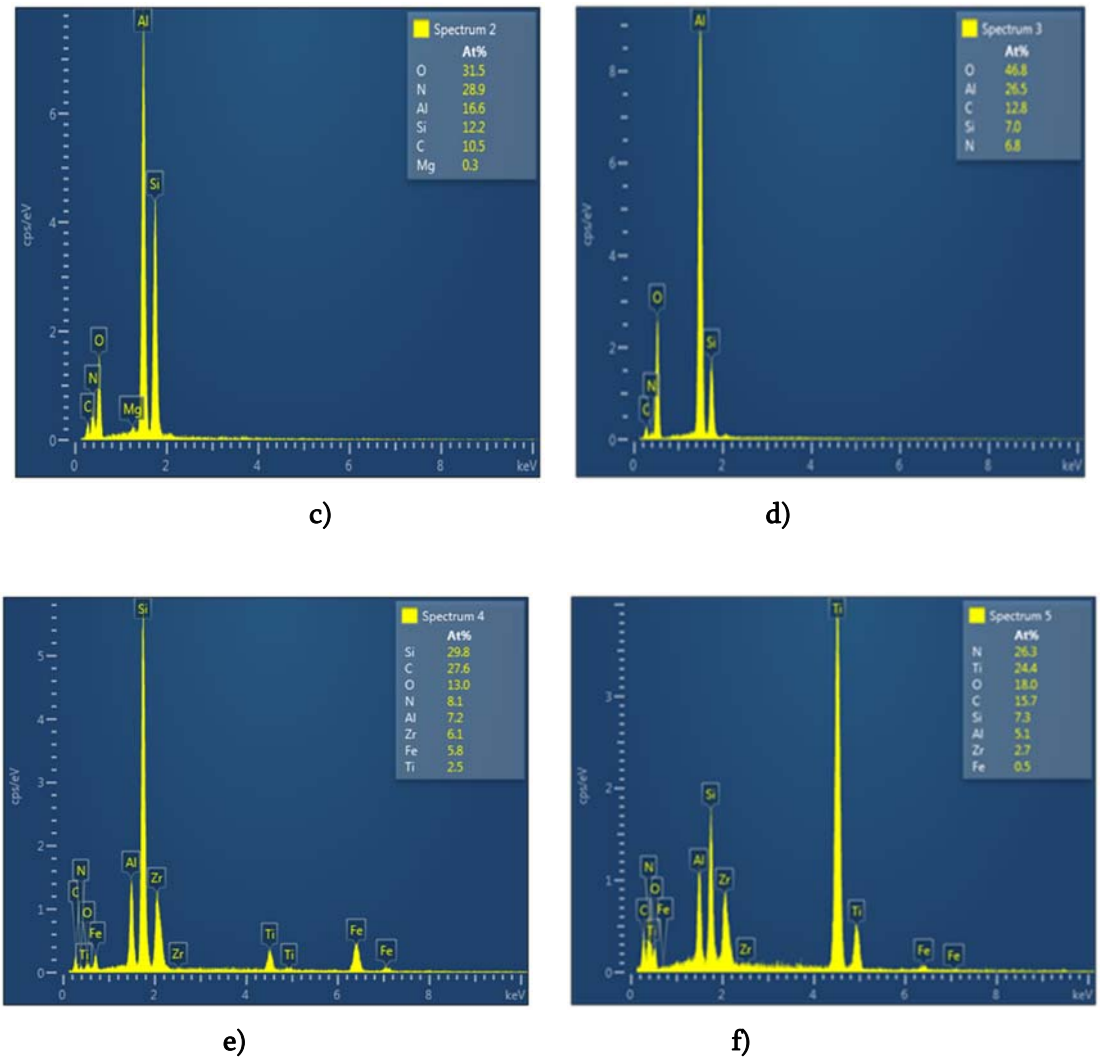

Fig. 4. Results of micro-spectral (EDS) analysis (a–v):
a) magnification ×5500; b) magnification ×10,000

Thus, the comparison of SEM, XRD, and EDS data confirms that, at a temperature of 1500°C, a dense β-SiAlON-based composite was formed in the Si–SiC–Al system using natural additives via the nitridation method. The presence of elongated β-crystals observed in the microstructure is directly correlated with the high intensity of the β-phase detected by XRD, which ultimately determines the superior performance characteristics of the material.

The study of the physical and mechanical properties of pressed samples within the temperature range of 1300–1500°C demonstrated a direct correlation between the thermal treatment temperature and the final density of the material (Table 2).

The lowest porosity (0.02%) was recorded at 1300°C, indicating that, at this temperature, the liquid phase formed due to natural additives is still insufficient to completely fill the intercrystalline

spaces. This result is in full agreement with the SEM micrographs, where the number of pores is minimal.

The increase in density from 2.97 to 3.21 g/cm³ indicates the threshold of strength associated with the complete formation of the β-SiAlON phase. High strength values under compression (356–375 MPa) and bending (166–250 MPa) are noteworthy, which are attributed to the reinforcing effect of SiC and the inherent strength of the SiAlON matrix.

Table 2

The characteristics of the N4 Composite

Composite index	Compaction temperature	Open porosity w, %	Total porosity, ∏, %	Density, ρ, g/cm³	Compressive strength, mpa	Flexural strength, mpa
4	1300⁰C	3,40	10,1	2.97	356	166
4	1500⁰C	0,02	0,02	3.21	375	250

The micromechanical properties of the obtained materials were determined using a DUH-211S dynamic ultra-microhardness tester in compliance with the requirements of the modern ISO 14577 international standard.

The graphs (e.g., *sialon basis 100 a..jpg* and *sialon white 100 a..jpg*) illustrate the loading and unloading cycles [12]. The fact that the curves are closely aligned, with minimal scatter, indicates a high degree of material homogeneity.

The shape of the force-depth curves indicates that the material possesses a high capacity for elastic recovery. A smaller residual depth following load removal corresponds to a higher material hardness.

The force-depth curves obtained via nanoindentation (Fig. 4) confirm the high local hardness of the SiAlON matrix. The minimal scattering of the data points indicates structural homogeneity within the composite, which was achieved through the selection of the optimal synthesis regime."

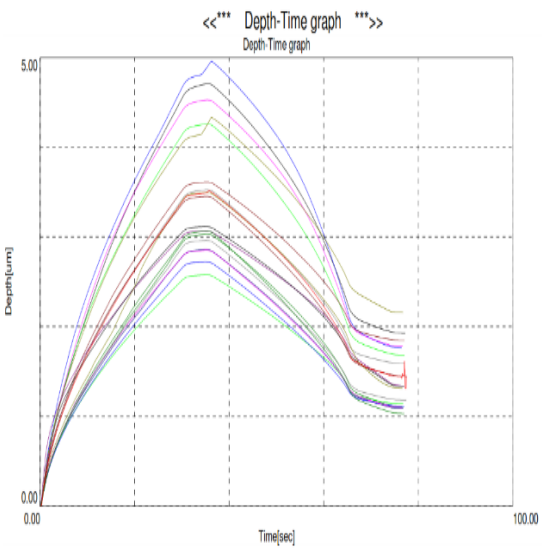
<<*** Depth-Time graph ***>>
Depth-Time graph
5.00
0.00
Depth[um]
0.00
100.00
Time[sec]

a)

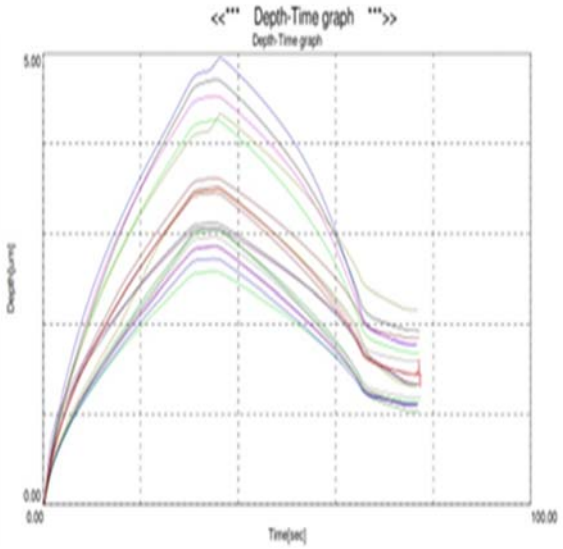
<<*** Depth-Time graph ***>>
Depth-Time graph
5.00
0.00
0.00
100.00
Time[sec]

b)

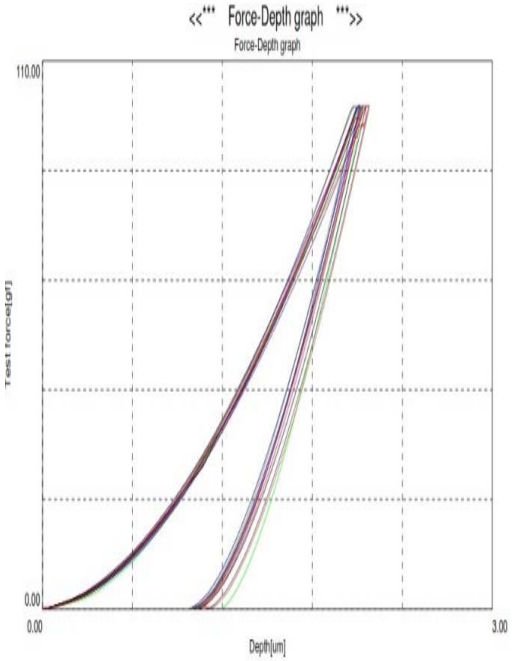
<<*** Force-Depth graph ***>>
Force-Depth graph
110.00
0.00
Test force[gf]
0.00
3.00
Depth[um]

a)

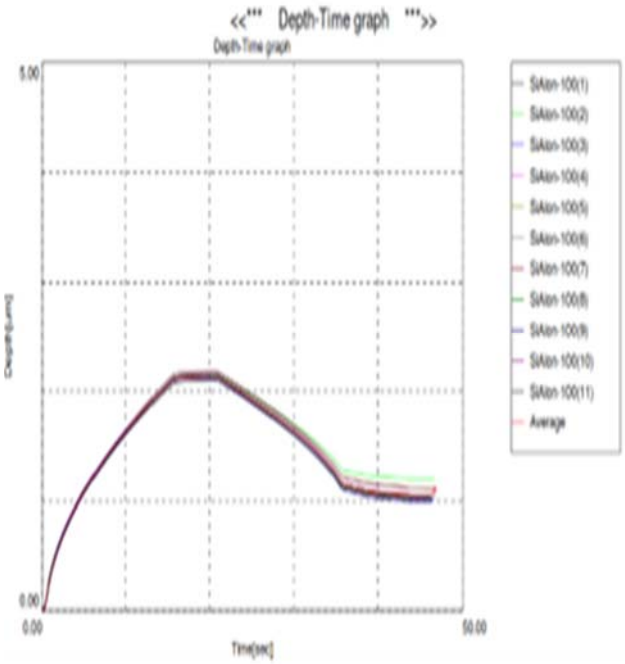
<<*** Depth-Time graph ***>>
Depth-Time graph
5.00
0.00
0.00
50.00
Time[sec]
SiAlon-100(1)
SiAlon-100(2)
SiAlon-100(3)
SiAlon-100(4)
SiAlon-100(5)
SiAlon-100(6)
SiAlon-100(7)
SiAlon-100(8)
SiAlon-100(9)
SiAlon-100(10)
SiAlon-100(11)
Average

d)

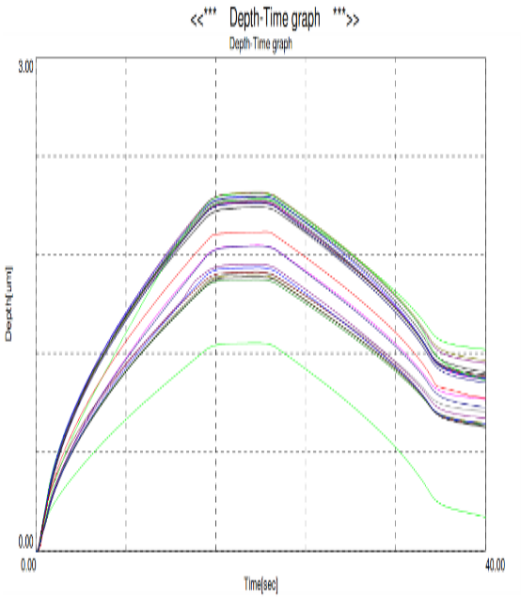

e)

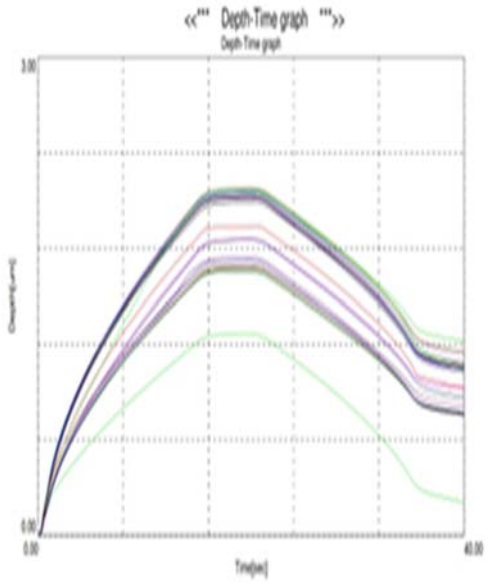

f)

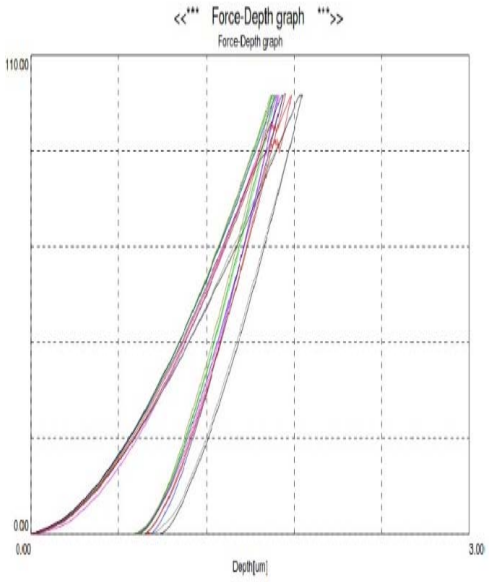

g)

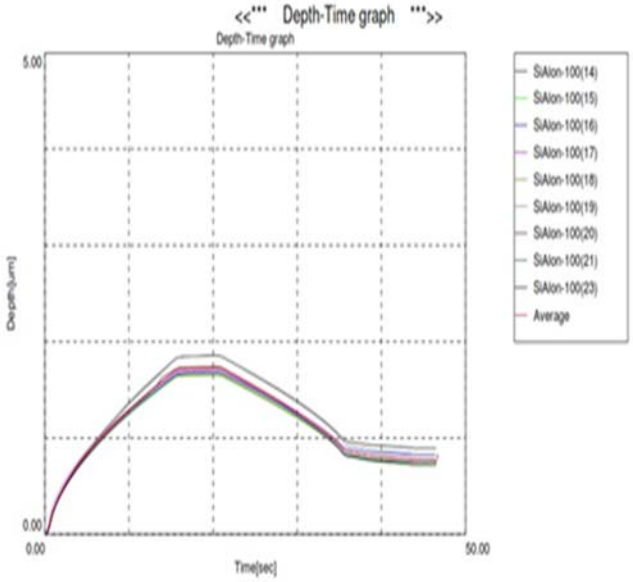

h)

Fig. 4. Micro-mechanical properties
of the obtained composite. a), b), c), d), e), f), g), h).

The samples obtained from the investigated composite were subjected to thermal shock resistance testing. The specimens were heated in a muffle furnace at 1300 °C with a holding time of 30 minutes, after which they were immediately immersed in a water bath at room temperature, and changes on the sample surface were monitored. Under these thermal cycling conditions, the samples withstood 21 cycles without any observable defects, confirming the high thermal shock resistance of the developed material.

According to the empirical relationship proposed by Professor Z. Kovziridze, the fracture stress energy can be expressed as a function of mass and velocity in the following form:

$$E_{td}=mxas.p\ ,$$

Where, E_{td}-energy of tension of decomposition; m-mass; a-speed of crack propagation.

In our case, the sample made of electrical-grade material was fabricated in the form of a rod with the following dimensions: length l = 110 mm, width b = 20 mm, and height a = 10 mm. At 1450 °C, the mass of the sintered rod with these dimensions was 45.5 g.

The specimen is fully consolidated, exhibiting zero open porosity. Assuming that the crack propagation velocity during fracture is 2000 m/s, the fracture energy dissipation, according to our empirical formula, can be calculated as follows:

$$Etd=45.5g\cdot(2000m/s)=91kJ$$

3. CONCLUSION

The results of the presented study confirm that:

1. High-quality SiAlON-based composites can be obtained in the Si–SiC–Al system via the nitridation method using natural raw materials (kaolin, clay, and perlite).

2. XRD analysis revealed that in the temperature range of 1500–1620°C, the main crystalline phase is β-SiAlON, while SiC inclusions are retained in the structure.

3. SEM investigations demonstrated a “self-reinforced” microstructure with elongated SiAlON crystals, which contributes to the material’s monolithic character.

4. The obtained composite, characterized by zero open porosity, high compressive strength (265 MPa) and flexural strength (170 MPa), as well as high thermal resistance, is considered a promising material for the fabrication of refractory components intended for aggressive environments.

REFERENCES

1. Jack, K. H. (1976). Sialons and related nitrogen ceramics. Journal of Materials Science, 11(6), 1135-1158. DOI: 10.1007/BF00553100
2. Ekström, T., & Nygren, M. (1992). SiAlON Ceramics. Journal of the American Ceramic Society, 75(2), 259-276. DOI: 10.1111/j.1151-2916.1992.tb04471.x
3. Hampshire, S. (2007). Sialon ceramics. In Structure and Properties of Ceramics (pp. 119–127). https://doi.org/10.1002/9783527603978.ch4. In Encyclopedia of Materials: Science and Technology (pp. 8555–8559).
4. Riley, F. L. (2000). Silicon Nitride and Related Materials. Journal of the American Ceramic Society, 83(2), 245-265. DOI: 10.1111/j.1151-2916.2000.tb01182.x
5. Z.D. Kovziridze (1993). Development of Scientific Bases and Technology for Obtaining

Celsian and Alumosilicate Ceramics Using Barite and Perlite (Doctoral thesis, pp. 41–50). Tbilisi.

6. Z. Kovziridze, N. Nizharadze, et al. (2014). Obtaining of nanocomposites in SiC–SiAlON and Al_2O_3–SiAlON systems by alumothermal processes. Journal of Electronics Cooling and Thermal Control, 4(1), 1–11. https://doi.org/10.4236/jectc.2014.41001
7. Mazzucato, F., et al. (2016). Synthesis of SiAlON ceramics from natural clays. Applied Clay Science, 132-133, 450-458. DOI: 10.1016/ j.clay.2016.08.001
8. Kartal, G., et al. (2011). Synthesis of SiAlON powders from kaolin using carbothermal reduction nitridation. Ceramics International, 37(1), 365-371. DOI: 10.1016/j.ceramint. 2010.08.013
9. T. Kordzakhia et al. (2020). High-temperature synthesis of SiAlON-based composites from Georgian natural raw materials. Ceramics–Silikáty, 64(2), 213–221. https://doi.org/10.13168/cs.2020.0006
10. Chen, I. W., & Rosenflanz, A. (1997). A tough SiAlON ceramic based on the α–β transformation. Nature, 389(6652), 701–704. https://doi.org/ 10.1038/39542
11. Belmonte, M. (2006). Advanced ceramic-matrix composites microstructure and properties. Advances in Science and Technology, 45, 1261-1270. DOI: 10.4028/www.scientific.net/AST.45.1261
12. Oliver, W. C., & Pharr, G. M. (1992). An improved technique for determining hardness and elastic modulus using load and displacement sensing indentation experiments. Journal of Materials Research, 7(6), 1564–1583. https://doi.org/10.1557/JMR.1992.1564
13. Guo, S. Q. (2009). Reaction-sintered ZrB_2–SiC ceramics. Journal of the European Ceramic Society, 29(6), 995–1005. https://doi.org/10.1016/j.jeurceramsoc.2008.11.008
14. Zou, J., et al. (2012). Synthesis and characterization of SiAlON-SiC composites. Materials Chemistry and Physics, 133(1), 159-164. DOI: 10.1016/j.matchemphys.2012.01.005,

უაკ 666.762.93

ბუნებრივი ალუმინოსილიკატების ბაზაზე დაფუძნებული β-SiAlON-SiC კომპოზიტების სინთეზი და დახასიათება

ზ. კოვზირიძე, მ. მშვილდაძე, ნ. კუცია ვა, მ. კაპანაძე, თ. წილოსანი, თ. ლოლაძე, ნ. ნიჟარაძე, გ. ტაბატაძე, მ.ბალახაშვილი, ნ. დარახველიძე, ვ. ქინქლაძე

საქართველოს ტექნიკური უნივერსიტეტი, ბიონანოკერამიკისა და ნანოკომპოზიტების ტექნოლოგიის ინსტიტუტი, სტუ ბიონანოკერამიკისა და ნანოკომპოზიტების მასალათმცოდნეობის ცენტრი. თბილისი. კოსტავას 69. საქართველო

E-MAIL: kowsiri@gtu.ge

რეზიუმე: მიზანი. მიზანი. ნაშრომი იკვლევს Si-SiC-Al სისტემაში ნიტრიდაციის მეთოდით მიღებული β-SiAlON კომპოზიტების სინთეზს და სტრუქტურულ თვისებებს, ბუნებრივი ალუმინოსილიკატების (პერლიტი, კაოლინი) გამოყენებით.

მეთოდი. სტრუქტურული თვისებები გამოკვლეული იქნა რენტგენის დიფრაქციული (XRD) ანალიზისა და სკანირების ელექტრონული მიკროსკოპიის (SEM) გამოყენებით.

ასევე შეფასდა მიკრო და მაკრომექანიკური თვისებები.

შედეგები. დადგინდა, რომ 1300–1500°C ტემპერატურის დიაპაზონში წარმოიქმნება მყარი SiAlON მატრიცა. მიღებულია თვითგამაგრებული მიკროსტრუქტურა. ფიზიკურ-მექანიკურმა ტესტირებამ აჩვენა, რომ 1500°C ტემპერატურაზე კომპოზიტს ახასიათებს ნულოვანი ღია ფორიანობა და მაღალი სიმკვრივე (3.21 გ/სმ³).

დასკვნა. მიღებული მასალები პერსპექტიულია მაღალი ტემპერატურისა და ეროზიული გარემოსთვის.

საკვანძო სიტყვები: β-SiAlON, სილიციუმის კარბიდი, კომპოზიტი, სტრუქტურა, ალუმინოსილიკატი.

UDC 691.2

TREATMENT OF MALIGNANT TUMORS WITH MAGNETIC HYPERTHERMIA AND GUIDED LOCAL HYPERTHERMIA

Z. Kovziridze[1], N. Mitskevich[2], S. Badzgaradze[3], G. Mentheshashvili[4], P. Khorava[4], A. Saldadze[3]

[1] Institute of Bionanoceramic and Nanocomposite Technology Technical University of Georgia. 69, Kostava Str., Tbilisi 0175, Georgia,

[2]Iv. Javakhishvili Tbilisi State University Department of Immunology and Microbiology, 1, Av.Chavchavadze, Tbilisi 0172, Georgia,

[3]Immuno and Oncothermia center ''INTEGRA''. 9 April Street. 8. 4600. Kutaisi. Georgia,

[4]Institute of Clinical Oncology, 5, Lublyana str., Tbilisi, 1059, Georgia

E-mail: kowsiri@gtu.ge

Resume: **Goal.** The receiving ultra dispercive nanoparticle for controlled local hyperthermia. **Method.** Average size of hematite and magnetite micro and nano powders and poly dispersity index, zeta potential and distribution of particles were studied. Analysis showed that average size of the obtained particles for magnetite is 740.9 nm, for hematite ultra dispersive particles – 30-100 nm. Alternate current feed source was created for hyperthermia. Proceeding from the requirements of the objectives the U type MnZn material magneto conductors were selected, in which 10.0 and 8.0 mm width gaps were cut and glass test tubes with magnetite or hematite suspensions were placed in them. Series of experiments at various field intensity and frequencies showed that for efficient magnetic hyperthermia therapy more powerful device was needed with frequency of up to 10 Mega Hertz to achieve the temperature -42-45^{o}C necessary for full activation of Neel and Brown mechanisms in particles.

Results. As a result of the experiment it was shown that in all animals (outbred albino mice, 3 months old) inhibition of cancer growth was fixed and intratumoral necrosis developed, while after 7 and 10 sessions tumors were ulcerated, which refers to positive effect of the experiment (Conclusion of Pathologic anatomical Laboratory "PATGEO", Tbilisi, Georgia).

Conclusion. High anti-blastoma effect innovate-ive technology was developed. Apparatus worked on patients in oncological clinic "INTEGRA" Kutaisi for treating by "Cancerthermia" method. **Received high results. The anti-cancer mono therapeutic effect and adjuvant action was proved in cancer polychemiotherapy.** Creation of innovative technology of locally controlled "Cancerthermia" for treating patients

Key words: magnetic hyperthermia, nanopowder, malignant cancer, necrosis, ulceration, controlled local hyperthermia, "Cancerthermia".

1. INTRODUCTION

It is known that malignant cancers consist of cancer cells, which differ from normal ones by uncontrolled and unlimited propagation and

growth of cells. Therefore intensity of metabolic processes in malignancies and, correspondingly, energetic requirements are higher than in common healthy tissues. Taking into consideration this factor, it is perspective to use chemical and biophysical effects on cancer tissues and its neighboring tissues, which in definite time period will exhaust energetic potential of degenerated cells, will result in denaturation (death) of their proteins and will preserve viability of healthy cells.

Such biophysical impact might be the local hyperthermia (42-45 ^{o}C).

Cancer cells die at about 43^{o} C, since delivery of oxygen via blood vessels is insufficient, while normal cells are not injured even at higher temperature. Alongside with it, cancer is heated easier than normal tissues around it, since blood vessels and nervous systems are less developed in cancer [1-3].

Research strategy is: Therapy of voluntary patients in the clinic by the method "Cancerthermia" created at the Center of **Bionanoceramic and Nanocomposites Material Science Center** of Georgian Technical University (GTU) by the use of Clinical apparatuses "LEZI-1" Innovation and uniqueness of the technology is that, on the base of **experimental material, for the first time in Georgia therapeutic effect and adjuvant action of anticancer mono-therapeutic treatment was presented in cancer's polychemiotherapy.**

2. MAIN PART

Ceramic microspheres for cancer radiotherapy $Y_2O_3 – Al_2O_3 – SiO_2$ glass microspheres

In 1987 Hyatt and Day [4] and Erbe and Day [5] proved for the first time that it was possible to use $17Y_2O_3$ – $19Al_2O_3$ –64 SiO_2 (mol%) 20-30 μM diameter glass microspheres for *in situ* irradiation of cancer. In this glass Yttrium-89 (^{89}Y) is nonradioactive isotope, which is found in nature at 100%, but neutron irradiation results in activation of ^{89}Y, which results in creation of β-irradiating ^{90}Y, half-life of which equals to 64.1 hr. When these 20-30 mcm diameter radioactive glass microspheres are injected into organism (e.g. liver cancer) they fall into narrow blood vessels of cancer and block delivery of nutrients. Alongside with it, it gives high-ionized β -rays acting at short distances. β-ray does not affect other chemical elements and it has short, 2.5 mm penetration range into live tissue and thus is not dangerous for healthy tissues. These microspheres are characterized by high chemical durability and therefore the radioactive ^{90}Y microsphere stays in diseased body and doesn't affect surrounding healthy tissues. Radioactivity of ^{90}Y at neutron irradiation [6] decreases to insignificant level in 21 days; therefore microspheres lose activity after treatment of cancer. They are used already clinically for liver cancer therapy in Canada, USA and China. They are used in clinical experiments for treatment of affected kidney and spleen and in cinoectomy irradiation of arthritis joints. [7-20].

Ceramic microspheres for cancer hyperthermia, ferromagnetic glass ceramics

Currently lithium ferrite ($LiFe_5O_8$) containing glass ceramic in hematite (α-F_2O_3) bio-compatible matrix and SiO_2-P_2O_5 glass phase [21-27], magnetite (F_3O_4) in β-volastonite (β-$CaSiO_3$) matrix and CaO-SiO_2-B_2O_3-P_2O_5 glass phase [28-35], α-Fe_2O_3 [36], in Fe_3O_4 B_2O_3 -free CaO-SiO_2-P_2O_5 glass phase [37] and zinc-iron ferrite in CaO-SiO_2 glass phase [38] are developed as thermo grain to be used

in hyperthermia. Thus, e.g. glass ceramic, that contains F_3O_4 in β-$CaSiO_3$ matrix and CaO-SiO_2-B_2O_3-P_2O_5 glass phase was efficient [29-31] in destruction of cancer cells implanted in rabbit femoral bone, when it was introduced in the pin-form into brain channel and [36] was placed in alternate magnetic field [33]. But such glass-ceramic pins can't be used clinically, since cancer cells can be scattered around normal cells and injection of glass-ceramic pins can result in cancer metastasis. 20-30 mcm diameter ferromagnetic microspheres might be used for local heating of cancer through loss of hysteresis by ferromagnetic materials, without initiation of cancer metastasis. Microspheres can be introduced into cancer via blood vessels [39] and then place it in alternate magnetic field. But up to now, 20-30 mcm size microspheres are not obtained and they have not revealed high heat formation capacity. Currently precise mechanism of hyperthermia for cancer therapy is not known. Unknown is the size of magnetite or hematite particles too. There are no data in special references about it.

Index of morbidity and lethality conditioned by melignancies in the whole world is increasing permanently. Early diagnostics is rather difficult and majority of patients address hospitals because of generalized cancers (III-IV stages), when they need combined surgical, radiation and drug therapy and complex treatment. Number of patients who address physician-oncologists with manifestation of clinical signs and various metabolic derangements inherent to complicated cancer processes has increased.

Development of new methods of treatment of melignancies is the most urgent task of oncology Inculcation of drugs and methods of treatment possessing positive effects which are proved by experimental and clinical studies –into clinical practice is a forward step in the sphere of treatment of oncologic patients.

Goal and objectives of hyperthermal studies

The present research pursues improvement of modern and recent results in the sphere of treatment of patients suffering from cancer, by the application of hyperthermia on cancer formation.

To achieve this goal we plan to resolve the following objectives:

1. Study of anticancer therapeutic effect on experimental cancers'
2. Determination of adjuvant anticancer effect of hyperthermia in experiment, in combination with poly-chemotherapy.
3. Study of various regimes of hyperthermia considering immediate and recent results.

Experimental

To implement the first stage works, first of all, we'll take X-ray of the used magnetite powder and hematite nano-particles obtained on the rotation kathode device created by us; Fig. 1 and Fig.2

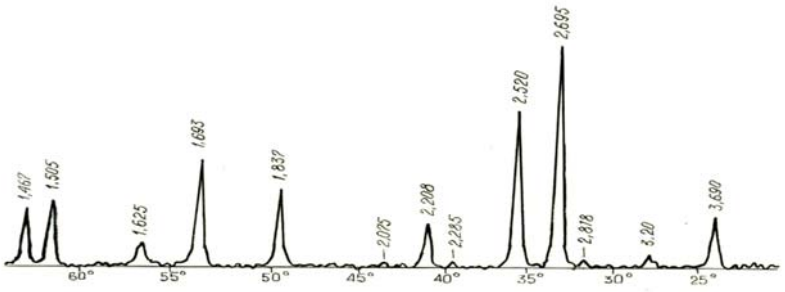

Fig.1.X-Ray of the obtained (α-Fe_2O_3) hematite nanopowder

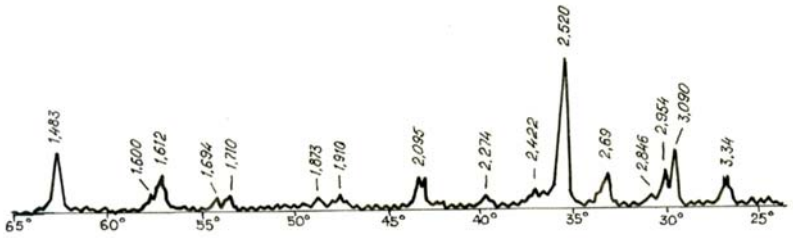

Fig. 2. X-Ray of the used magnetite (Fe_3O_4) micropowder

As is seen from the X-ray analysis magnetite consists mainly of Fe_3O_4, d_{hkl}=2,954; 1,520; 2,095; 1,710; 1,612; 1,483Å, hematite d_{hkl}=2,690; 2,520; 2,422; 1,710; 1,694; 1,600 Å, traces of $CaCO_3$ d_{hkl}=3,030; 1,910; 1,873 and traces of SiO_2, but the main mass is magnetite, therefore powder is of dark black color.

The obtained hematite powder is red, and the mass completely consists of α-Fe_2O_3. With "Nanophox" device –Clausthal-Zellerfeld, Germany - accumulation curve of hematite particle distribution and particle density-normal Gauss distribution was determined (Fig. 3 and 4). From Figures is shown, that in powder the particles (agglomerate) with sizes till 300 nm are 62-63%. The "Nanophox" device fixd also the agglomerated nanopowder. Fig. 5 shows graphical representation of analysis of hematite powder stability. Fig. 6 shows the rotation cathode device created by us (Patent, receiving methode-registration number 11731, 15.03.2010. Georgian National Patent Center "SAQPATENTI")

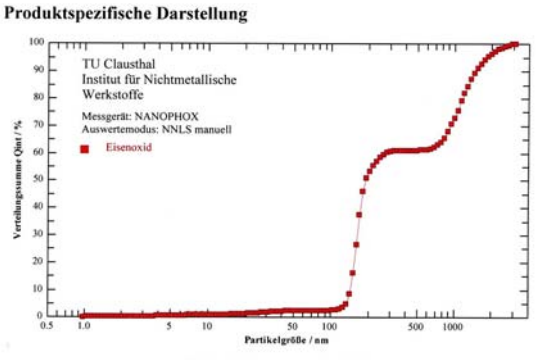

Fig.3. The curve of the particle distribution of the hematite nanopowder.

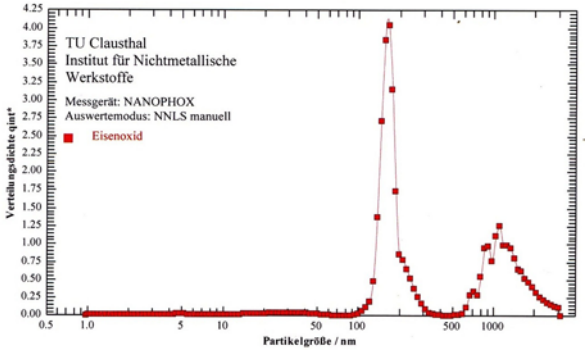

Fig. 4. The compactness of the hematite nanopowder

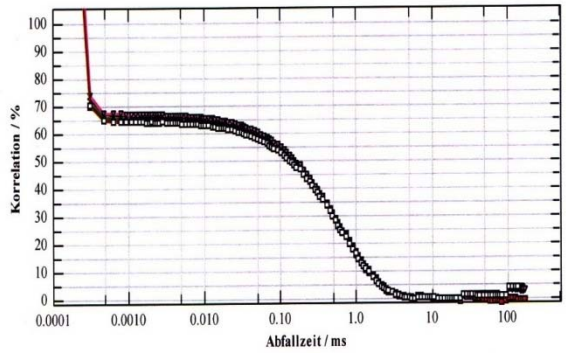

Fig. 5. offers graphical expression of analysis of powder stability.
In the process of Analysis powder revealed homogeneity, equal distribution According to sizes and correspondingly, good stability.

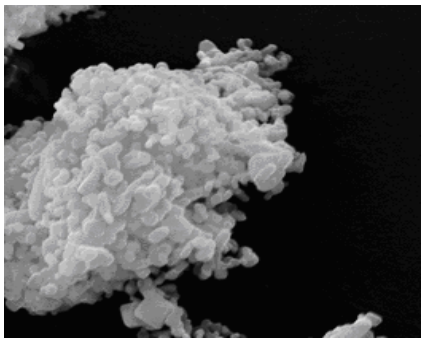

Fig. 6. The rotation cathode device for receiving of hematite nanopowders and scanning electron-microscopy representation of hematite agglomeration. Average size of the particle 30-100nm.

After phase analysis the physical properties of magnetite powder were studied on the apparatus "Nanosizer" of Great Britain origin (in Germany, Clausthal-Zellerfeld, Institute of Steine und Erden). Powder was screened through # 0063-8270 mesh sieve in advance.

Intensity on the offered Figures is that of the transmitted laser ray, Width - is a peak width and shows the particle distribution according to dimensions. The narrower a peak, the more homogeneous is spreading.

Particle characterization is based on the average size and polydispersity index Pdl. If its value is within 0,1-0,5 the suspension is of good polydispersity.

Zeta potential is the potential of diffuse layer of a particle, which is in the solvent. If the value of Zeta-potential is within 30mv +30mv, such particle has a tendency towards aggregation.

According to the analysis the sizes of the obtained particles are redistributed mainly in two ranges/bands. Approximately 93% of particles are of 200-1000 nm and their average size equals to 478,6 nm. Sizes of approximately 7% of particles are within 3-7 μM. Their average size is 5,41μ. This should be a result of nanoparticles aggregation. To study the impact of further mechanical treatment on the sizes of the obtained particles, experimental lot was treated in a porcelain cup, for 5 hours, in single-ball vibrating mill.

After grinding in vibrating mill for 5 hours the average particle size is 740,9 nm, polydispersity

index - 0,571; big (coarse) 3-7 mcm size particles disappeared, general dispersity of particles increased, which conditioned low Zeta – potential - 19,8 mv. This refers to a tendency of this dispersity powder towards aggregation.

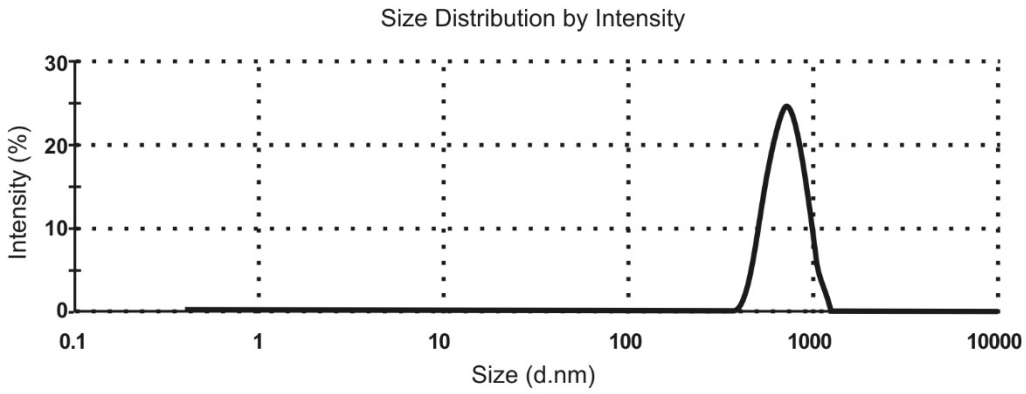

Fig. 7. Analysis of powder ground in vibrating mill for 5 hours.

Dispersant – water

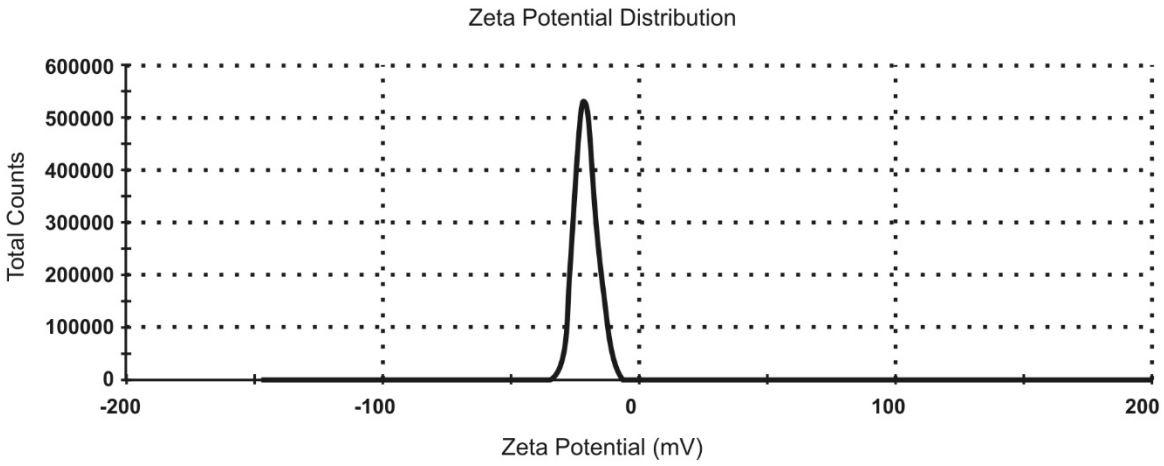

Fig. 8. Zeta –potential of powder ground in vibrating mill for 5 hrs. Dispersant – water

The present research aimed to create a device for hyperthermia. Original, alternate current feed source (Fig. 9) was created for application of method of hyperthermia, to achieve thermal scattering of magnetic particles [40-42] and to obtain alternate current magnetic field. The device is characterized by the following parameters:

- Output voltage 0 -240 V;
- Current for loading – 10 A (long-term regime);
- Peak load – 12 A;
- Range of alternate current frequency – 20 kHz – 295 kHz
- Frequency alteration load – 1 kHz.

Output voltage value was restricted by the terms stipulated for security observance.

Schematic-construction type parameters of the above stated feed source were experimentally correlated according to the alternate magnetic field intensity level to be created.

Thermocouple was used for temperature measurements (due to small sizes and low inertia) in a set with 3.5-rate digital tester. For elevation of accuracy of this method a tester was calibrated at 45 ◦C.

For measuring of current form, value and frequency we used electron-ray two-channel 1 MHz oscillograph. Dada was taken at 0.1 Ohm 0.1% accuracy shunt inserted in power circuit, at the coil, in succession.

Determination of the necessary level of magnetic field intensity was based on the following experiment: in 10 mm diameter PVC (polyvinylchloride) test tube, in 1 gram distilled water the 1x3 mm size 15 mg thin iron plate was immersed (hereinafter referred as Tube #0). It was considered that at definite approximation, the above stated composition was a version corresponding to 1.5% water solution of the tested powder. Then a tube was placed in various intensity alternate magnetic fields.

Practically all types of toroidal, TD, E, ELP, U standard dimension magnetic conductors were tested.

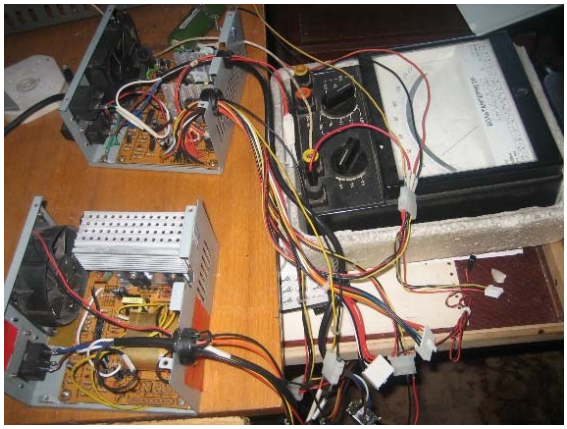

Fig. 9. Original alternate current feed source

Fig.10. Selected magnetic conductor types

Proceeding from the pursued objectives, after data correlation the preference was given to U type magnetic conductors of MnZn material, of 67/87 electromagnetic properties (Fig.10). To receive the needed dimensions, alongside with the standard magnetic conductors, we used those of needed sizes, which were obtained by corresponding mechanical treatment of ETD34, E42 and E52 standard magnetic conductors.

In the bundle of magnetic conductors various size gaps were cut: 20mm, 16 mm, 12 mm, 10 mm and 8 mm. On the basis of experience acquired in the process of experiments 10.0 mm and 8.0 mm width gaps were given preference as working ones. Similarly, optimal dimensions of magnetic conductors in millimeters were selected:

1. 50 X 50 X 11;
2. 60 X 50 X 12;
3. 40 X 40 – area of magnetic conductor section 32 mm^2;
4. 40 X 30 - area of magnetic conductor section 32 mm^2.

To cover the whole range of 20 kHz-295 kHz frequency electric coils were prepared for every magnetic conductor:

1. 42 windings – 2.0 mm transformer copper conductor;
2. 36 windings - 2.0 mm transformer copper conductor;
3. 34 windings - 2.0 mm transformer copper conductor;
4. 30 windings - 2.0 mm transformer copper conductor;
5. 30 windings - 3 X 0.6 mm transformer copper conductor;
6. 26 windings - 2.0 mm transformer copper conductor;
7. 22 windings - 2.0 mm transformer copper conductor;
8. 18 windings - 1.5 mm^2 section mounting multithread copper conductor;
9. 16 windings -1.5 mm^2 section mounting multithread copper conductor;
10. 12 windings -1.5 mm^2 section mounting multithread copper conductor;

Magnetic conductors prepared by us together with the above stated alternate current feed source enabled us to carry out sets of experiments at various field intensity and frequency.

#1 and #2, that is 5% and 10% suspensions were prepared from hematite and magnetite, correspondingly. From 8 mm diameter glass pipe the tubes were made in which the above referred suspensions were poured (Fig. 11).

Initially experiments were conducted at the frequencies: 27.7 kHz, 33.3 kHz, 40.0 kHz, 50.0 kHz, 66.0 kHz, 100.0 kHz, 166.0 kHz, 200.0 kHz, 250.0 kHz and 290.0 kHz.

By variation of voltage coming from power source we fixed 4.0. 5.0, 8.0, 9.0 and 10.0 A current in electric coils. Temperature monitoring was performed in 1 min, 5 min, 10 min and 15 min intervals. Expediency of continuation of experiments in alternate magnetic field of lower than 8.0 A was practically excluded. Similarly was excluded application of gaps width of which exceeded 10 mm. Magnetic field intensity in 8 mm and 10 mm gaps for magnetic conductors of the above frequencies were obtained: 4200 A/winding, 4000 a/winding 3800 A/winding, 3400 A/winding, 3200 A/winding, 3000 A/winding, 2800 A/winding, 2600 A/winding.

Fig. 11. Test tubes made of glass pipe

Fig.12. Course of experiment

The first series of experiments showed that temperature of solutions in tubes placed in magnetic field (Fig, 12) compared to the environment temperature used to increase within 15 minutes only by 8.0-10.0 °, inclusive 6-7 °, within the first 5 minutes. Tube #0, when placed in analogous intensity field within the first 5 minutes yielded 25-30 ° increase, inclusive 15-20 ° in the first minute. Intensity of increase of temperature is directly proportional to magnetic field intensity. In the process of experiments, in gaps, at high magnetic field intensity, significant overheating of magnetic conductors and power winding was observed. According to measure-ments, temperature on the surface of magnetic conductors at gaps used to increase up to 50-70 °C during experiments. Therefore, the impact on tubes would have been significant too. A series of experiments was carried out that showed that increase of temperature by 6-7 °C in 5 min period in tubes was conditioned by thermal effect of magnetic conductor in gaps.

As it was shown by the experiments, more powerful device of 5-10 mega Herz is needed for efficient treatment by magnetic hyperthermia to enable thorough activation of Neel and Brawn mechanisms at the impact of alternate magnetic field on micro- and nanopowders obtained by us. The works in this direction will be continue. We have developed also other method, a new device for hyperthermia therapy and further works were continued at the second stage. Conditionally we called the device "Lezi" (Fig.13). (Georgian Inteligent Privecy National Center "SAQPATE-NTI". Deponing Certificate 5054. Work: "Control Local Hyperthermia and Magnetic Hyperthermia for Therapy of Malignancies").

Fig. 13 Device "Lezi" (in the left).
Cage with mice (in the right)

Antitumoral effect of hyperthermia
in experimental cancers
at the treatment by a device "Lezi"

Stage II

Scientific novelty

On the basis of experimental material the anticancer mono-therapeutic effect of hyperthermia and its adjuvant action in polychemotherapeutic treatment was presented for the first time in Georgia.

With this in view rational schemes of hyperthermia were developed.

Essence of research

Materials and methods:

3 months old 18-20 g albino mice (outbred, non-linear) were used in experiments.

After selection for experiments, the mice were kept in vivarium for 10-14 days at quarantine regime, according to sex. Individual protocols were executed for each animal. Animals were kept at similar feeding and care conditions.

Experiments were carried out by the use of cancer strain of Erlich adenocarcinoma. Inoculation of Erlich adenocarcinoma was performed in mices, subcutaneously, in infrascapular region.

Experiments were carried out by the methods widely applied in experimental oncology. The anticancer effect of hyperthermia was evaluated according to cancer growth inhibition, frequency of intratumoral necrosis and changes in the data of animal life prolongation.

The results will be processed by variation statistics methods.

The study was conducted on 18 groups of mice. Here are the typical results:

Obtained results and discussion

Experiments fixed inhibition of cancer growth in the I, III and V animals, while in the II, IV and VI animals, where progressive growth of a size of cancer formation was observed, the so called "intratumoral necrosis" was developed in cancers – necrosis of cancer cells. This, according to our opinion is conditioned by the effect of hyperthermia.

In the second experimental group we again studied anticancer therapeutic effect of hyperthermia. On the first day of the experiment, on 17.04.2024, subcutaneous inoculation of EAT cancer strain was performed. Cancer developed in all three experimental animals.

Table 1

Animal #	Number of sessioins and date of measuring size					
	I 17.04.2023	II 20.04.2023	III 22.04.2023	IV 24.04.2023	VII 30.04.2023	X 09.05.2023
1	8x8x5/10x8x5	8x8x5/10x5x5	10x8x5/8x5x3 (necrosis)	10x8x5/5x5x3 (necrosis)	12x10x8/5x5x3 (necrosis, ulcerarion)	10x10x8/8x8x5 (necrosis, ulceration)
2	10x8x5	10x8x5	8x8x5 (necrosis)	8x6x3 (necrosis)	16x12x5 (necrosis, ulceration)	12x9x5 (necrosis, ulceration)
3	16x14x10	16x14x10	16x14x10 (necrosis)	16x14x5 (necrosis)	17x14x5 (necrosis, clearly expressed ulceration)	21x14x8 (necrosis, clearly expressed ulceration)

17.04.2023 - we measured animal cancers (see Table #1, Fig. 14). Measurements were performed after every 3 sessions. On 20.04.2024 the first session of hyperthermia was carried out. These sessions were carried out every second day. A device was placed on cancer formation; at the ends of a device 43-45^{o}C was fixed. Length of hyperthermia manipulation equaled to 30, 40 and 50 min, correspondingly, on I, II and III animals.

The first mouse was two-humped. Treatment was performed on the right hump.

After 3 sessions of the experiment it was found that in all three animals inhibition (stopping) of cancer growth was fixed, while the II and III animals revealed development of intratumoral necrosis in cancers (Fig. 14). In this case, again, inhibition of cancer growth and intratumoral necrosis were conditioned by the effect of hyperthermia.

In these animals measurements were made after seven sessions. According to Table 2 and visually necrosis and ulceration are observed, which refers to positive effect of the experiment. After ten sessions, again vivid necrosis and ulceration of the tumor was observed, see Fig. 15.

#1

#2

#3

Fig.14. Animals #1, #2 and #3 after 3 sessions. Intratumoral necrosis was observed in the II and III cases. In the I case inhibition of progress of cancer was observed.

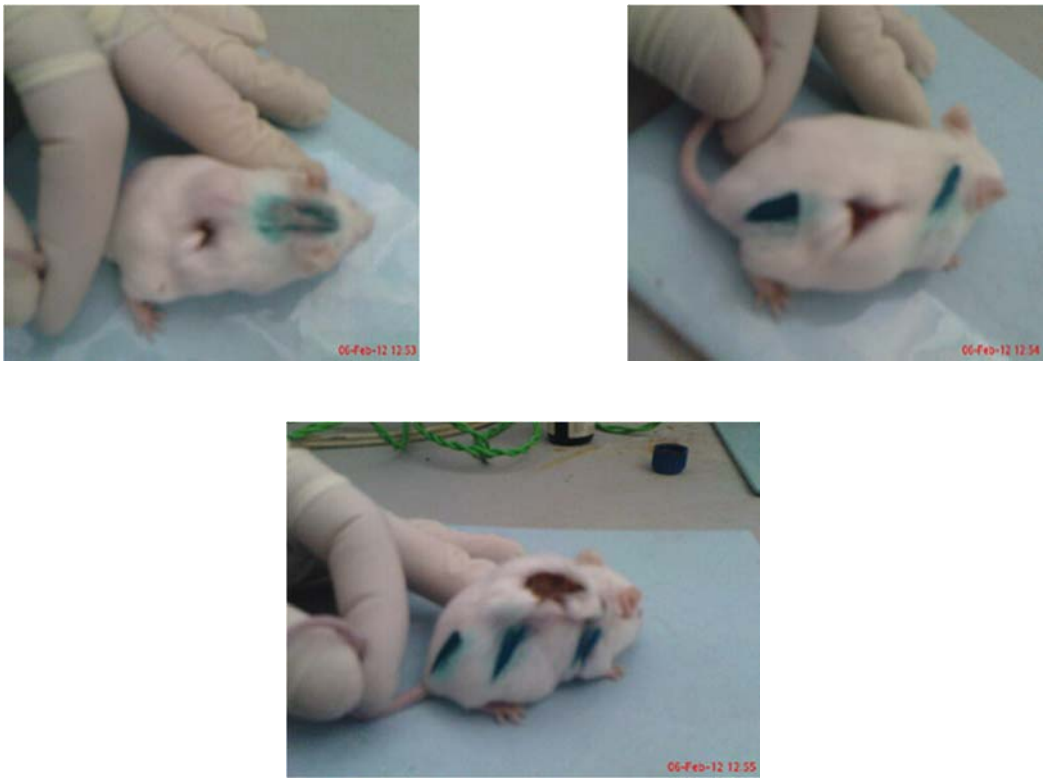

Fig. 15. #1. #2 and #3 animals after ten sessions.
Ulceration of tumor is fixed. Necrosis is clearly expressed.

According the next stage of experiments the results show, that After the eighth session necrosis of the whole treated diseased section was apparent and ulceration around the tumor section in all three animals was observed which refers to transition of disease to the phase of recovery. Currently animals are under supervision, they feel themselves well.

There were three or four sessions left before the end of the treatment, but at the suggestion of the oncologists, both animals were euthanized and an analysis of the liver and lungs was performed in the pathological-anatomical laboratory "Path-geo" to see the possibility of metastatic spread of the tumor to the organs. The analysis with pictures and their description is presented below.

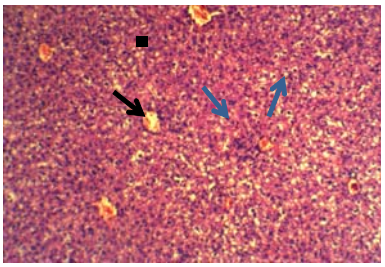

N1 A Liver

Fig.16 The black arrow shows a blood vessel with the presence of erythrocytes in it. The blue arrow shows hepatocytes (liver cells) around the blood vessel. Tumor cells are not detected in the preparati

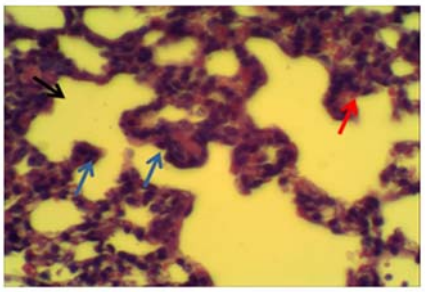

1 A. Lung

Fig.17 Black arrow - shows pulmonary alveoli, blue arrow - first-order alveolocytes, red arrow - erythrocyte. Tumor cells are not detected in this preparation. Accordingly, based on the results of morphological studies, no liver and lung tumor metastases were observed

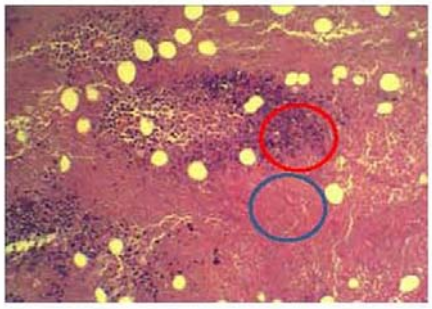

A Tumor

Fig. 18 Blue circle - necrotic masses. Red circle - karyorhexis (the process of cell nucleus breakdown). Tumor cells are observed, with pronounced posimorphism, which characterizes Ehrlich adenocarcinoma

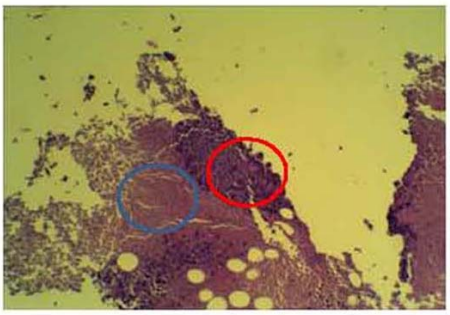

A Tumor

Fig. 19 Blue circle - necrotic tissue. Red circle - tumor cell plastids,
characterized by pronounced nuclear polymorphism (various)

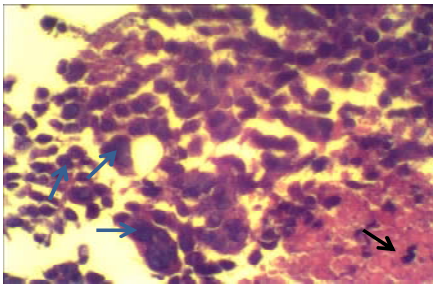

A Tumor

Fig. 20. Black arrow - focal necrosis. Blue arrow - tumor cells, characterized by hyperchromic (dark), sharply polymorphic nuclei

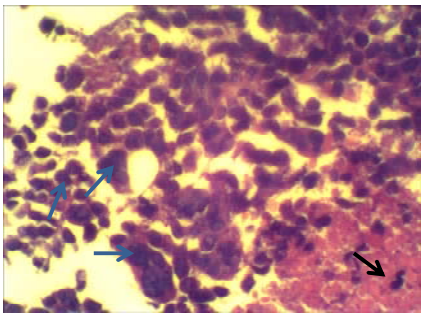

A. Tumor

Fig. 21 Black arrow - focal necrosis. Blue arrow - tumor cells, characterized by hyperchromic, sharply polymorphic nuclei

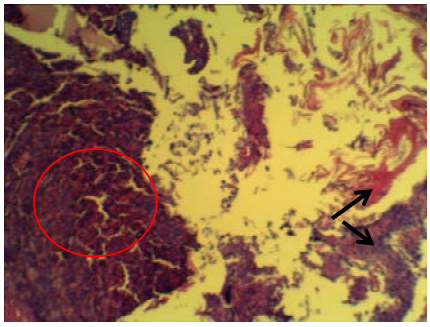

A. Tumor

Fig.22 Black arrow - skin, epidermis, subcutaneous tissue. Red circle - solid proliferates of tumor cells (multiplying cells)

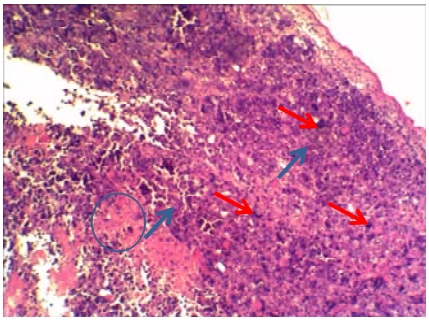

A. Tumor

Fig. 23 Blue circle - necrosis center. Blue arrow - tumor cells, characterized by hyperchromic, sharply polymorphic nuclei. Red arrow - so-called. ugly cells

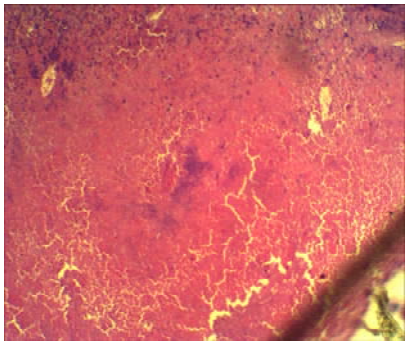

A tumor

Fig. 24 This image shows necrosis

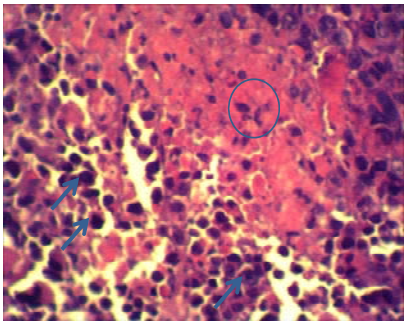

A tumor

Fig. 25. Blue circle - a focus of necrosis. Blue arrow - tumor cells, characterized by hyperchromic, sharply polymorphic nuclei

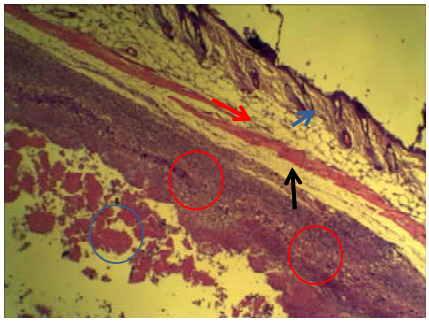

A tumor

Fig. 26 Blue arrow - skin. Red arrow - subcutaneous adipose tissue. Blue circle - necrotic tissue. Red circle - tumor cell proliferates. Black arrow - platysma striated muscle tissue

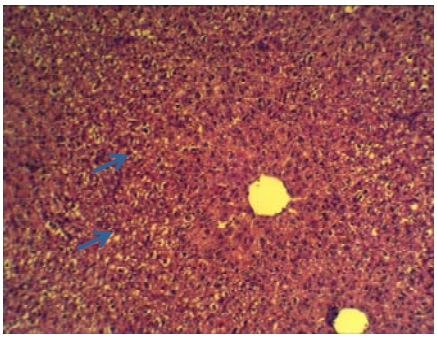

Liver

Fig. 27 Tumor cells are not fixed. Blue arrow - hepatocytes around the blood vessel

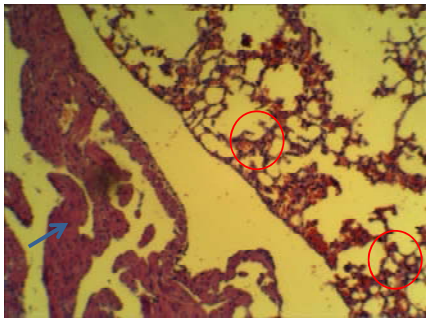

B. Lung

Fig. 28 Red circle - pulmonary alveoli, exposed alveolocytes. Blue arrow - fibrous tissue. Here too, based on the results of morphological examination, no tumor metastases were seen in the liver and lungs

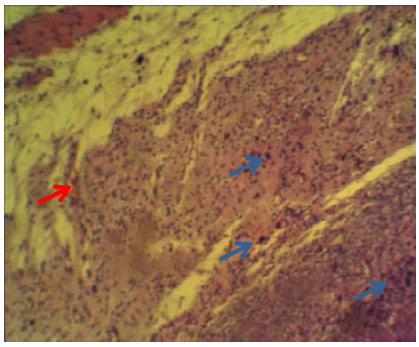

B. Tumor

Fig.. 29 Red arrow - blood vessel, erythrocytes. Blue arrow - tumor cells

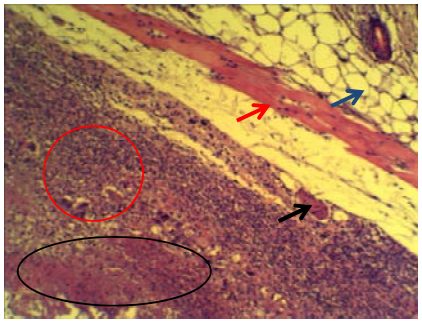

B. Tumor

Fig.. 30 Blue arrow - subcutaneous adipose tissue. Red arrow - platysma striated muscle tissue. Black arrow - nerve fiber. Red circle - tumor cell proliferation. Black oval - necrosis focus

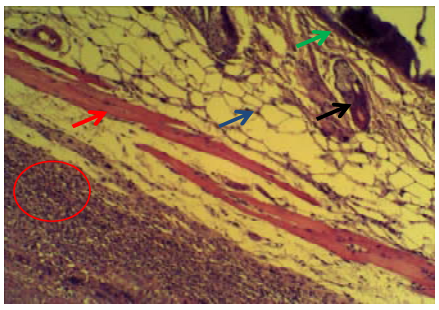

B. Tumor

Fig. 31 Blue arrow - subcutaneous adipose tissue. Red arrow - platysma striated muscle tissue. Black arrow - hair bulb. Green arrow - skin, epidermis. Red circle - tumor cell proliferation

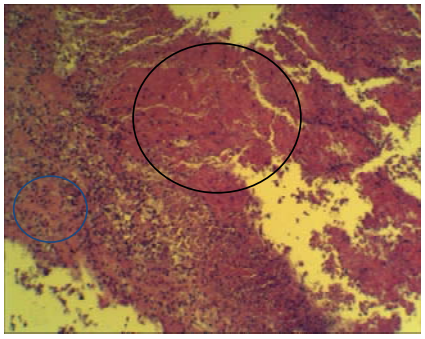

B. Tumor

Fig. 32 Black circle - necrosis center. Blue circle - proliferates of surviving tumor cells

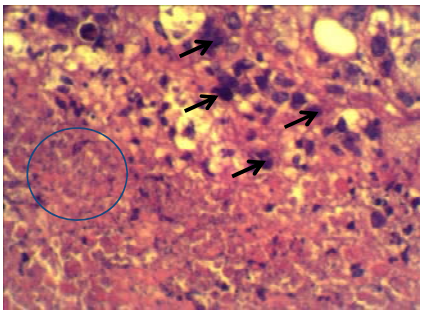

B. Tumor

Fig. 33 Black arrow - tumor cell, hyperchromic and sharply polymorphic nucleiiT. Blue circle - focal necrosis

The antitumor effect is assessed by reducing the tumor mass, necrosis of tumor tissue, and complete disappearance of the tumor. Also, the tumor tissue was studied in dynamics by the method of morphological research, tumor necrosis, and correlation of tumor mass and necrotic areas. Based on the results of the morphological research, it was determined that the liver and lungs (the main target organs) are intact, and secondary tumor lesions are not recorded. After three sessions of hyperthermic treatment, a decrease in the size of the tumor formation and necrosis of the disease are visually observed in animals of all groups. And massive necrosis, after seven sessions. In all cases, necrosis and ulceration of the disease are observed, which indicates the transition to the phase of tumor healing.

After eight to ten sessions, necrosis and ulceration of the disease are again observed, which indicates the irreversibility of the process and the effectiveness of the hyperthermic method used. In all cases, the inhibition of tumor growth and intratumoral necrosis are due to the effects of hyperthermia. The results of visual observations are confirmed in all animals: measurements and photographs taken after three, seven, and ten sessions.

We have developed an innovative technology for patients called "*Cancerthermia*." Below, we will focus on the aspect of innovation of the technology. A wrung piece of thin fabric that was dipped in 42-45^{0}C water is applied on the tumor area identified during the preliminary examinations. On the peace of fabric, 25x18 cm (or any other size) 45^{0}C thermopad of our instrumentis placed until the fabric runs dry (time is empirical), in order to ensure the *precursor pre-treatment* of the patient's skin, to open and expand the pores, so that

the heat emitted from the thermopad penetrates deeper into the diseased area to make cancer cells to be more likely affected by "*Cancerthermia"* and killed. Thereafter, the temperature on the equipment should be lowered to 43^{0}C, and the session continued for a period of about 40-80 minutes, depending on how the patient and the disease itself responds to "*Cancerthermia"*. When using the above mentioned technology in the clinic, the results have been achieved after 7 – 8 sessions, instead of 10-12 sessions, which is beneficial to the patients both psychologically and financially. Innovative method and anti blastoma technology results proved to have a success at "Integra" Oncology Clinical Center in Kutaisi, where our medical equipment to treat cancer using a controlled local "*Cancerthermia"* method was introduced in the first stage of treatment by this method, the clinic achieved good results in all cancer patients (Fig. 35-41). Patient treatment is ongoing and the results are equally positive. The anticancer effect is evaluated by reduction of tumor mass, necrosis, and outright disappearance of the tumor. In addition, tumor tissue dynamics has been studied using morphological method, by correlation between tumor necrosis and tumor mass and necrotic areas. This technological innovative method, which we named as "Cancerthermia".

The morphological study showed that liver and lungs (primary target organs) are intact, secondary tumor lesions are not observed. No metastatic lesions were observed in the organs.

Therefore, Based on the available material we can say that there is no metastasis in these organs during tumor mass lysis as a result of Local controlled "Cancerthermia".

Fig. 34. Clinical therapeutic apparatus "LEZI-I" for local controlled cancerthermia, created at the Bionanoceramic and Nanocomposites Material Science Center of Georgian Technical UNiversity (head: Professor Z.Kovziridze). Certificate 6193. 18.02.2015. Georgian Patent.)

This apparatus can be used for treating any body, less brain, rectum and cervix uterus. We offer MRT images of bodies of some cancer patients as a characteristic example, which show clearly cancer formations up to therapy and their disappearance or decrease within three seances after treatment: ovaries, stomach and lung. Full cycle consists from 6-7 seances.

Clinical Case 1

- **Patient : 55 years old.**
- **Ds: NSCLC**
- **stage 3**

pT3N2M0

Before treatment **After treatment**

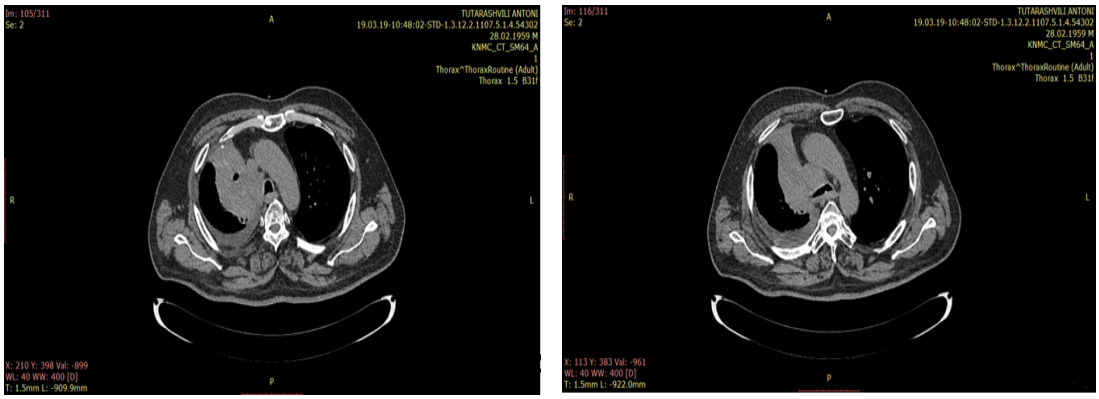

Fig. 35

Clinical Case 2

- Patient : I.L 28 years old
- DS: NSCLC
- Stage 4
- pT2N2M1

Before treatment **After treatment**

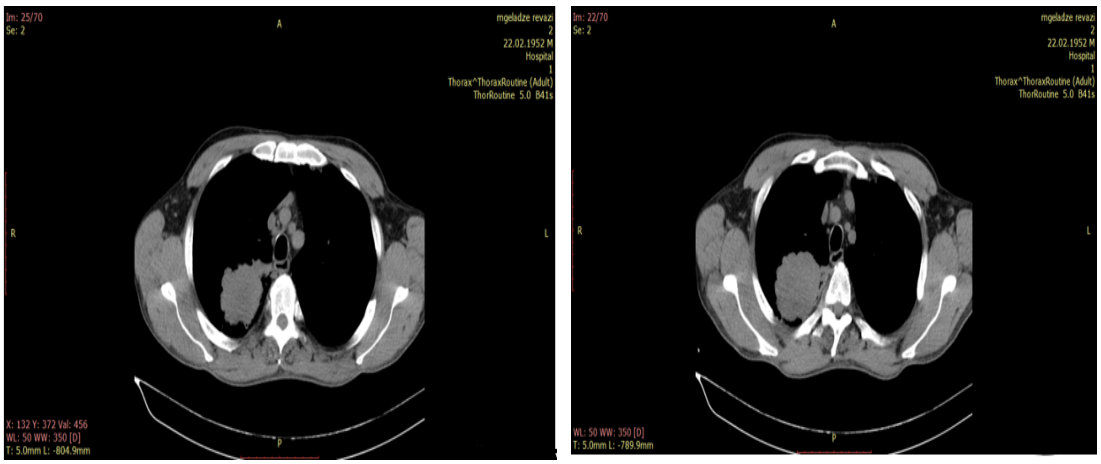

Fig. 36

Clinical Case 3

- Patient : V.CH.58 years old
- DS: NCSLC
- Stage:4

PT2N1M1

Befor treatment **After treatment**

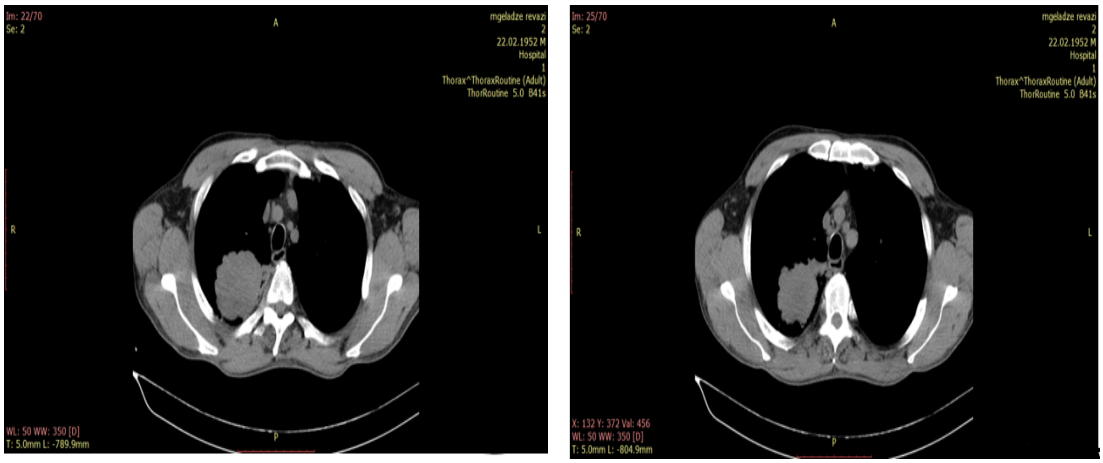

Fig.37

Clinical Case 4

Picture 38. Patient with malignant ovaries cancer; C56 III stage, II cl. group

1. Before treatment **2. After treatment**

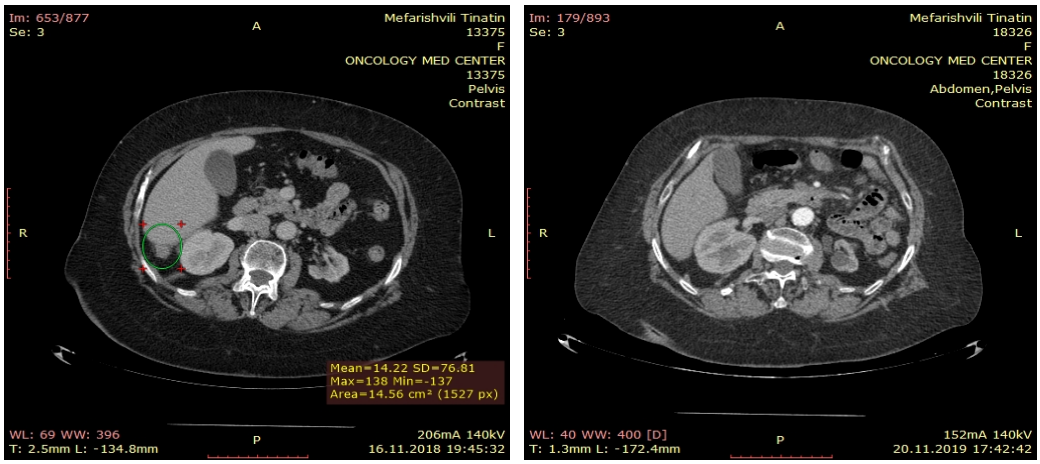

Fig. 38

Clinical case 5

3.Before treatment 4. **After treatment**

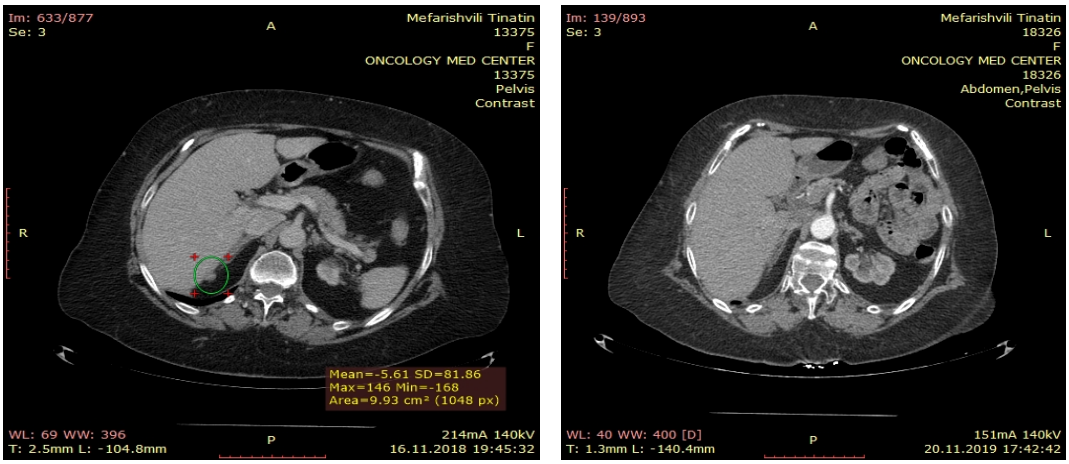

Fig. 39

Picture 15. Malignant gastric cancer C16.9 II stage, II cl. group

1. Before treatment 2. **After treatment**

Clinical Case 6

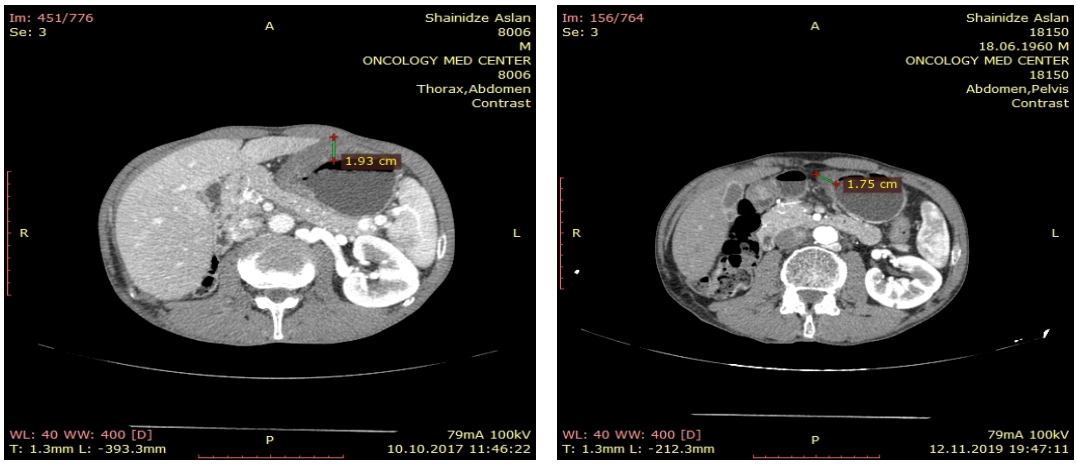

Fig.40

Clinical case 7

3. Before treatment **4. After treatment**

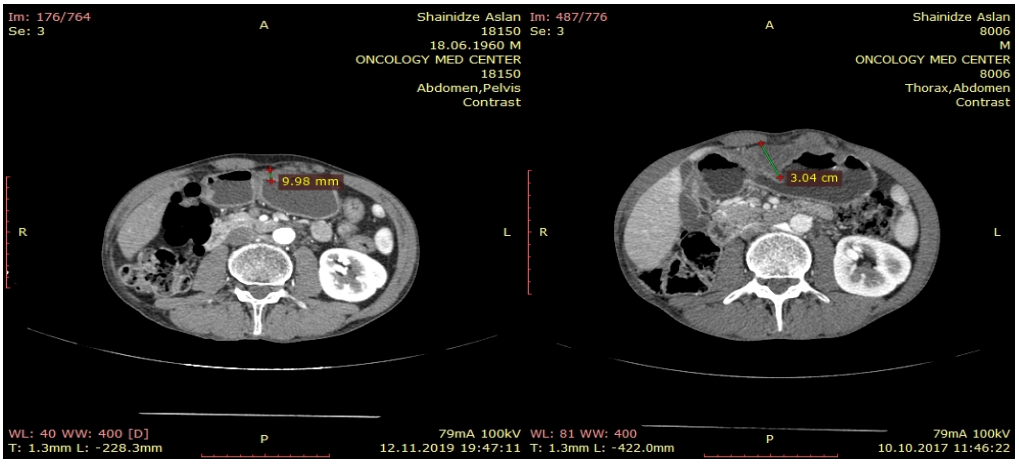

Fig. 41

3. CONCLUSION

The ultimate goal of the work: to create an innovative high-tech controlled local "cancerthermia" method created by us for the treatment of cancer tumors in the clinic for patients. innovative high-tech guided local “cancerthermia” has been developed as a monotherapeutic and adjuvant anti-tumor effect, using our devices “LEZI-1”, In polychemotherapy treatment of tumors.

Modern methods are used to conduct research: MRT, chemical, thermal, X-ray structural, electronic and biological microscopy, etc. Advantages of our work and the uniqueness lies in the fact that the controlled local "cancerthermia" treatment is harmless to human health and is not characterized by any side effects. and as a result has great advantages over surgical, chemo- and radiation therapy.

Based on the above, the importance of the research, both for Georgia and internationally, for both the social situation and technological development, is invaluable.

REFERENCES

1. R. Cavaliere, E. C. Ciocatto, B. C. Giovanella, C. Heidelberger, R. O. Johnson, M. Margottini, B. Mondovi, G. Moricca, and A. Rossi-Fanelli, “Selective Heat Sensitivity of Cancer Cells. Biochemical and Clinical Studies,” Cancer, 20 1351–1381 (1967).
2. K. Overgaard and J. Overgaard, “Investigation on the Possibility of a Thermic Tumour Therapy. II. Action of Combined Heat-Roentgen Treatment on a Transplanted Mouse Mammary Carcinoma,” Eur. J. Cancer, 8 573–575 (1972).
3. J. Overgaard, “Effect of Hyperthermia on Malignant Cells In Vivo. A Review and a Hypothesis,” Cancer, 39 2637–2646 (1977).
4. M. J. Hyatt and D. E. Day, “Glass Properties of Yttria–Alumina–Silica System,” J. Am. Ceram. Soc., 70 283–287 (1987).

5. E. M. Erbe and D. E. Day, "Chemical Durability of Y2O3–Al2O3–SiO2 Glasses for the In Vivo Delivery of Beta Radiation," J. Biomed. Mater. Res., 27 1301–1308 (1993).
6. D.E. Day and T.E. Day, "Radiotherapy Glasses," An Introduction to Bioceramics. eds. L.L. Hench and J. Wilson. World Science, Singapore, 305–317, 1993.
7. G. J. Ehrhardt and D. E. Day, "Therapeutic Use of 90Y Microspheres," J. Nucl. Med., 14 233–242 (1987).
8. R. V. Mantravadi, D. G. Spigos, W. S. Tan, and E.L. Felix, "Intraarterial Yttrium 90 in the Treatment of Hepatic Malignancy," Radiology, 142 783–786 (1982).
9. M. J. Herba, F. F. Illescas, M. P. Thirlwell, G. J. Boos, L. Rosenthall, M. Atri, and P. M. Bret, "Hepatic Malignancies: Improved Treatment with Intraarterial Y-90," Radiology, 169 311–314 (1988).
10. I. Wollner, C. Knutsen, P. Smith, D. Prieskorn, C. Chrisp, J. Andrews, J. Juni, S. Warber, J. Klevering, J. Crudup, and W. Ensminger, "Effects of Hepatic Arterial Yttrium 90 Glass Microspheres in Dogs," Cancer, 61 1336–1344 (1988).
11. S. Houle, T. K. Yip, F. A. Shepherd, L. E. Rotstein, K. W. Sniderman, E. Theis, R. H. Cawthorn and K. Richmond-Cox, "Hepatocellular Carcinoma: Pilot Trial of Treatment with Y-90 Microspheres," Radiology, 172 857–860 (1989).
12. J.H. Anderson, J.A. Goldberg, R.G. Bessent, D. J. Kerr, J. H. McKillop, I. Stewart, T. G. Cooke, and C. S. McArdle, "Glass Yttrium-90 Microspheres for Patients with Colorectal Liver Metastases," Radiol. Oncol., 25 137–139 (1992).
13. M.A. Burton, B.N. Gray, C. Jones, and A. Coletti, "Intraoperative Dosimetry of 90Y in Liver Tissue," J. Nucl. Med., 16 495–498 (1989).
14. F. A. Shepherd, L. E. Rotstein, S. Houle, T. C. Yip, K. Paul, and K. W. Sniderman, "A Phase I Dose Escalation Trial of Yttrium-90 Microspheres in the Treatment of Primary Hepatocellular Carcinoma," Cancer, 70 2250–2254 (1992).
15. Z. P. Yan, G. Lin, H. Y. Zhao, and Y. H. Dong, "An Experimental Study and Clinical Pilot Trials on Yttrium-90 Glass Microspheres Through the Hepatic Artery for Treatment of Primary Liver Cancer," Cancer, 72 3210–3215 (1993).
16. Z. P. Yan, G. Lin, H. Y. Zhao, and Y. H. Dong, "Yttrium-90 Glass Microspheres Injected via the Portal Vein," Acta Radiol., 34 395–398 (1993).
17. J. C. Andrews, S. C. Walker, R. J. Ackermann, L. A. Cotton, W. D. Ensminger, and B. Shapiro, "Hepatic Radioembolization with Yttrium-90 Containing Glass Microspheres: Preliminary Results and Clinical Follow-Up," J. Nucl. Med., 35 1637–1644 (1994).
18. J. H. Tian, B. X. Xu, J. M. Zhang, B. W. Dong, P. Liang, and X. D. Wang, "Ultrasound-Guided Internal Radiotherapy Using Yttrium-90-Glass Microspheres for Liver Malignancies," J. Nucl. Med., 37 958–963 (1996).
19. X. Cao, N. He, J. Sun, J. Tan, C. Zhang, J. Yang, T. Lu, and J. Li, "Hepatic Radioembolization with Yttrium-90 Glass Microspheres for Treatment of Primary Liver Cancer," Chin. Med. J., 112 430–432 (1999).

20. S. D. Chen, J. F. Hsieh, S. C. Tsai, W. Y. Lin, K. Y. Cheng, and S. J. Wang, "Intra-Tumoural Injection of 90Y Microspheres into an Animal Model of Hepatoma," Nucl. Med. Commun., 22 121–125 (2001).
21. M. Kawashita, F. Miyaji, T. Kokubo, G. H. Takaoka, I. Yamada, Y. Suzuki, and K. Kajiyama, "Phosphorus-Implanted Glass for Radiotherapy: Effect of Implantation Energy," J. Am. Ceram. Soc., 82 683–688 (1999).
22. M. Kawashita, R. Shineha, H.-M. Kim, T. Kokubo, Y. Inoue, N. Araki, Y. Nagata, M. Hiraoka, and Y. Sawada, "Preparation of Ceramic Microspheres for In Situ Radiotherapy of Deep-Seated Cancer," Biomaterials, 24 2955–2963 (2003).
23. M. Hiraoka and G. M. Hahn, "Comparison Between Tumor pH and Cell Sensitivity to Heat in RIF-1 Tumors," Cancer Res., 49 3734–3736 (1989).
24. N. Araki, Y. Nagata, M. Hiraoka, M. Kawashita, T. Kokubo, Y. Inoue, and Y. Sawada, "Treatment of VX2 Tumors in Rabbit Liver by Radioactive Y2O3 Microspheres," Transactions of the 7th World Biomaterials Congress. Edited by The Australian Society for Biomaterials Inc., Sydney, Australia, 1827, 2004.
25. N. F. Borrelli, A. A. Luderer, J. N. Panzarino, and H. L. Rittler, "Magnetic Glass–Ceramics for Tumor-Therapy by Hyperthermia," Am. Ceram. Soc. Bull., 61 819–819 (1982).
26. A. A. Luderer, N. F. Borrelli, J. N. Panzarino, G. R. Mansfield, D. M. Hess, J. L. Brown, E. H. Barnett, and E. W. Hahn, "Glass–Ceramic-Mediated, Magnetic-Field-Induced Localized Hyperthermia - Response of a Murine Mammary-Carcinoma," Radiat. Res., 94 190–198 (1983).
27. N.F. Borrelli, A.A. Luderer, and J.N. Panzarino, "Hysteresis Heating for the Treatment of Tumors," Phys. Med. Biol., 29 487–494 (1984).
28. Y. Ebisawa, T. Kokubo, K. Ohura, and T. Yamamuro, "Bioactivity of CaO _ SiO2-Based Glasses - In Vitro Evaluation," J. Mater. Sci.: Mater. Med., 1 239–244 (1990).
29. Y. Ebisawa, Y. Sugimoto, T. Hayashi, T. Kokubo, K. Ohura, and T. Yamamuro, "Crystallization of (FeO,Fe2O3)–CaO–SiO2 Glasses and Magnetic 182 International Journal of Applied Ceramic Technology—Kawashita Vol. 2, No. 3, 2005 Properties of their Crystallized Products," J. Ceram. Soc. Jpn., 99 7–13 (1991).
30. K. Ohura, M. Ikenaga, T. Nakamura, T. Yamamuro, Y. Ebisawa, T. Kokubo, Y. Kotoura, and M. Oka, "A Heat-Generating Bioactive Glass–Ceramic for Hyperthermia," J. Appl. Biomater., 2 153–159 (1991).
31. T. Kokubo, Y. Ebisawa, Y. Sugimoto, M. Kiyama, K. Ohura, T. Yamamuro, M. Hiraoka, and M. Abe, "Preparation of Bioactive and Ferrimagnetic Glass–Ceramic for Hyperthermia," Bioceramics, Vol. 3. eds. J. E. Hulbert and S. F. Hulbert. Rose-Hulman Institute of Technology, Indiana, 213–223, 1992.
32. Y. Ebisawa, T. Kokubo, K. Ohura, and T. Yamamuro, "Bioactivity of Fe2O3- Containing CaO–SiO2 Glasses—In-Vitro Evaluation," J. Mater. Sci.: Mater. Med., 4 225–232 (1993).
33. M. Ikenaga, K. Ohura, T. Yamamuro, Y. Kotoura, M. Oka, and T. J. Kokubo, Orthop. Res., 11 849 (1993).

34. Y. Ebisawa, F. Miyaji, T. Kokubo, K. Ohura, and T. Nakamura, "Surface Reaction of Bioactive and Ferrimagnetic Glass–Ceramics in the System FeO– Fe2O3–CaO–SiO2," J. Ceram. Soc. Jpn., 105 947–951 (1997).
35. Y. Ebisaw, F. Miyaji, T. Kokubo, K. Ohura, and T. Nakamura, "Bioactivity of Ferrimagnetic Glass–Ceramics in the System FeO–Fe2O3–CaO–SiO2," Biomaterials, 18 1277–1284 (1997).
36. H. Konaka, F. Miyaji, and T. Kokubo, "Preparation and Magnetic Properties of Glass–Ceramics Containing a-Fe for Hyperthermia," J. Ceram. Soc. Jpn., 105 833–836 (1997).
37. M. Kawashita, H. Takaoka, T. Kokubo, T. Yao, S. Hamada, and T. Shinjo, "Preparation of Magnetite-Containing Glass–Ceramics in Controlled Atmosphere for Hyperthermia of Cancer," J. Ceram. Soc. Jpn., 109 39–44 (2001).
38. M. Kawashita, Y. Iwahashi, T. Kokubo, T. Yao, S. Hamada, and T. Shinjo, "Preparation of Glass–Ceramics Containing Ferrimagnetic Zinc-Iron Ferrite for the Hyperthermal Treatment of Cancer," J. Ceram. Soc. Jpn., 112 373–379 (2004).
39. Masakazu Kawashita, Ceramic Microspheres for Biomedical Applications
Int. J. Appl. Ceram. Technol., 2 [3] 173–183 (2005).
40.Z.Kovziridze, G. Donadze, G. Mamniashvili, A. Akhalkatsi, D. Daraselia, D. Japharidze, O. Romelashvili, A. Shengelaia, C. Gavasheli, J.G. Heinrich. THE RECEIVING AND STUDY OF HEMATITE NANOPARTICLES FOR HYPERTHERMIA, 1st International Conference for Students and Young Scientists on Materials Processing Science, Tbilisi, Georgia 10-13 October 2010, Journal of Georgian Ceramists Association "Ceramics" N 2(23), 2010,1(24), 2011, Tbilisi, p.37-46.
41. Z. Kovziridze, J. Heinrich, R. Goerke, G. Mamniashvili, Z. Chachkhiani, N. Mitskevich, G. Donadze. Production of superparamagnetic nanospheres for hyperthermic therapy of surface (skin) cancer diseases. 3rd International congress on Ceramics, November 14-18, 2010, Osaka, Japan. IOP Conference Series: Materials Science and Engineering, 2010.
42. Z. Kovziridze, J. Heinrich, R. Goerke, G. Mamniashvili, A. Akhalkatsi, Z. Chachkhiani, N. Mitskevich, G. Donadze. PRODUCTION OF BIONANOCERAMIC SUPERPARAMAGNETICS FOR CREATION OF CONTROLLED. LOCAL HYPERTHERMIA AND THEIR USE, AS THERAPEUTIC AGENTS, FOR PURPOSEFUL TRANSPORTATION IN LIVING ORGANISMS IN SURFACE (SKIN) CANCER TREATMENT. Journal of Georgian Ceramists Association "Ceramics" N 1(22), Tbilisi, 2010, p.43-51.,

უაკ 691.2

ავთვისებიანი სიმსივნეების მკურნალობა მაგნიტური ჰიპერთერმიითა და მართვადი ლოკალური ჰიპერთერმიით

ზ. კოვზირიძე[1], ნ. მიცკევიჩი[2], ს. ბაძგარაძე[3], გ. მენთეშაშვილი[4], პ. ხორავა[4], ა. სალდაძე[3]

[1] საქართველოს ტექნიკური უნივერსიტეტი, ბიონანოკერამიკისა და ნანოკომპოზიტების ტექნოლოგიის ინსტიტუტი, თბილისი. კოსტავას 69. საქართველო.

[2] ივ. ჯავახიშვილის თბილისის სახელმწიფო უნივერსიტეტი. იმუნოლოგიის და მიკრობიოლოგიის დეპარტამენტი. ი. ჭავჭავაძის პრ. 1. თბილისი 0172 საქართველო.

[3] იმუნო და ონკოთერმიის ცენტრი „ინტეგრა“ 9 აპრილის ქ. 8. 4600 ქუთაისი საქართველო

E-MAIL: kowsiri@gtu.ge

რეზიუმე: მიზანი. მიზანი. კონტროლირებადი ლოკალური ჰიპერთერმიისთვის მიღებული ულტრადისპერსიული ნანონაწილაკი. **მეთოდი.** შესწავლილი იქნა ჰემატიტისა და მაგნეტიტის მიკრო და ნანო ფხვნილების საშუალო ზომა და პოლიდისპერსიულობის ინდექსი, ზეტა პოტენციალი და ნაწილაკების განაწილება. ანალიზმა აჩვენა, რომ მაგნეტიტის შემთხვევაში მიღებული ნაწილაკების საშუალო ზომაა 740.9 ნმ, ჰემატიტის ულტრადისპერსიული ნაწილაკებისთვის კი - 30-100 ნმ. ჰიპერთერმიისთვის შეიქმნა ალტერნატიული დენის წყარო. მიზნების მოთხოვნებიდან გამომდინარე, შეირჩა U ტიპის MnZn მასალის მაგნიტოგამტარები, რომლებშიც გაკეთდა 10.0 და 8.0 მმ სიგანის ნაპრალები და მათში მოათავსეს მინის საცდელი მილები მაგნეტიტის ან ჰემატიტის სუსპენზიებით. სხვადასხვა ველის ინტენსივობისა და სიხშირის ექსპერიმენტების სერიამ აჩვენა, რომ მაგნიტური ჰიპერთერმიის ეფექტური თერაპიისთვის საჭირო იყო უფრო მძლავრი მოწყობილობა 10 მეგაჰერცამდე სიხშირით, რათა მიღწეულიყო -42-45°C ტემპერატურა, რომელიც აუცილებელია ნაწილაკებში ნილისა და ბრაუნის მექანიზმების სრული გააქტიურებისთვის. შედეგები. ექსპერიმენტის შედეგად ნაჩვენები იყო, რომ ყველა ცხოველში (3 თვის ასაკის ალბინოსი თაგვები) დაფიქსირდა კიბოს ზრდის ინჰიბირება და განვითარდა სიმსივნისშიდა ნეკროზი, ხოლო 7 და 10 სესიის შემდეგ სიმსივნეები დაწყლულდა, რაც ექსპერიმენტის დადებით ეფექტზე მიუთითებს (პათოლოგანატომიური ლაბორატორიის „PATGEO“ დასკვნა, თბილისი, საქართველო).

დასკვნა. შემუშავდა მაღალი ანტიბლასტომური ეფექტის მქონე ინოვაციური ტექნოლოგია. აპარატი მუშაობდა ქუთაისის ონკოლოგიურ კლინიკა „INTEGRA“-ში პაციენტებზე „კანცერთერმიის“ მეთოდით მკურნალობისთვის. მაღალი შედეგები მიიღო. კიბოს საწინააღმდეგო მონოთერაპიული ეფექტი და დამხმარე მოქმედება დადასტურდა კიბოს პოლიქიმიოთერაპიაში. პაციენტების სამკურნალოდ ადგილობრივად კონტროლირებადი „კანცერთერმიის“ ინოვაციური ტექნოლოგიის შექმნა.

საკვანძო სიტყვები: მაგნიტური ჰიპერთერმია, ნანოფხვნილი, ავთვისებიანი კიბო, ნეკროზი, წყლული, კონტროლირებადი ადგილობრივი ჰიპერთერმია, „კანცერთერმია“.

UDC 666.3/7

PRODUCTION OF VITRIFIED CERAMIC TILES FROM GURIA POLYMINERAL CLAYS AND OBSIDIAN COMPOSITES

N. Gegia, T. Rukhadze, G. Enukidze, K. Khachaturiani, M. Tkemaladze, T. Loladze

LEPL TSU, Al. Tvalchrelidze Caucasus Institute of Mineral Resources 11 Mindeli St., 0186, Tbilisi, Georgia

E-mail: nestan.gegia@tsu.ge; temo798@gmail.com

Resume: This paper investigates the role of obsidian as a fluxing agent in composites formulated with low-grade polymineral clays from the Guria region. The incorporation of obsidian into the clay matrix enabled the fabrication of high-density vitrified ceramic tiles from the clay-obsidian composite system.

Objective. The aim of this research is to develop high-performance ceramic tiles that comply with international standards by incorporating a novel component (obsidian) into the polymineral clay composites native to the Guria region.

Method. Chemical and X-ray diffraction (XRD) analyses were employed to characterize the raw materials. XRD patterns were recorded using a DRON-4.0 diffractometer equipped with a copper anode and a nickel filter, operated at a scanning speed of 2°/min ($\lambda = 1.54778$ Å). Tile compaction was performed using an Italian Mignon SSN-EA laboratory hydraulic press. Firing was carried out in an Italian FCJM10/H51 muffle furnace at temperatures up to 1300°C, with a heating rate of 10°C/min and a soaking time of 20 min. The flexural strength of the fired tiles was evaluated using an Italian CC 96-2006 fleximeter.

Results. The material composition of the Guria ceramic clays was evaluated via chemical and mineralogical analyses. In their raw state (without additives), these low-grade clays are unsuitable for ceramic tile manufacturing. However, when blended into a composite system and pressed at 400 kgf/cm^2, the effective formation of a glassy phase at a relatively low firing temperature (1150 °C) successfully encapsulated the clay particles. This liquid-phase sintering mechanism yielded ceramic tiles characterized by minimal water absorption (0.0%–0.07%), high flexural strength (25.0–34.0 MPa), excellent frost resistance (passed 40 cycles), and outstanding acid resistance (98.5%–99.5%).

Conclusion. The vitrified ceramic tiles fabricated via the proposed technological process meet the mechanical and technological requirements of the international standard **ISO 13006:2018 (NEW)**, classifying them as Class I tiles. Furthermore, the products satisfy the technical specifications of **GOST 13996-93** (Ceramic facade tiles and carpets), **GOST 6787-2001** (Ceramic floor tiles), and **GOST 961-89** (Acid-resistant and thermo-acid-resistant ceramic tiles) for industrial and construction applications.

Key words: firing, vitrification, clay, ceramic tile, composite, acid resistance, obsidian, strength, porosity, frost resistance, shrinkage, water absorption.

1. INTRODUCTION

Ceramic tiles represent one of the oldest building materials, yet they remain highly relevant in modern architecture, with global and domestic demand expanding annually. The annual import volume of ceramic tiles currently stands at $55 million USD in Georgia and exceeds $300 million USD across the South Caucasus region, exhibiting a continuous upward trend. This expanding market has stimulated significant interest in evaluating and utilizing local raw material bases. Consequently, it is imperative to map domestic mineral resources, re-evaluate and systematize existing deposits, identify alternative raw materials, and develop advanced processing technologies [1].

2. MAIN PART

The objective of these technological investigations is to manufacture high-performance ceramic tiles capable of satisfying rigorous modern standards by introducing a novel fluxing component into polymineral clays sourced from the Lanchkhuti, Chokhatauri, and Ozurgeti municipalities of the Guria region. Various natural additives, including perlite, quartz, feldspar, pumice, and obsidian, were screened. Based on preliminary screening, obsidian was selected as the optimal fluxing agent. In ceramic processing, a flux is a material that reacts with clay minerals upon heating to form low-melting eutectic compounds. The introduction of obsidian into the composite formulation lowers the optimum firing temperature, minimizes pyroplastic deformation, enhances sintering kinetics, dramatically reduces water absorption to near-zero levels (0%–0.1%), and increases the bulk density and mechanical strength of the final product [2].

Obsidian acts as an exceptionally effective low-temperature fluxing agent that promotes liquid-phase formation, thereby binding the distinct mineral components into a coherent, high-density composite matrix. The application of obsidian as a highly reactive, glass-forming additive was pioneered and investigated at the Scientific-Research Department of Mineral Processing and Wastewater Treatment of the Al. Tvalchrelidze Caucasus Institute of Mineral Resources (TSU). Initial studies were conducted on representative geological surface samples of low-grade, polymineral clays from the Adjara region. The X-ray amorphous structure of obsidian ensures early-stage glassy phase formation at reduced firing temperatures, completely wetting the solid particles and accelerating the densification process. The resulting ceramic composites exhibited low water absorption, high mechanical strength, and enhanced acid and frost resistance at reduced thermal budgets. This developed technology was secured by a national patent [2].

Building upon the successful outcomes achieved with the Adjara clay composites, the research was extended to the low-grade polymineral clays of the Guria region (Lanchkhuti, Chokhatauri, and Ozurgeti municipalities). Obsidian native to Georgia was utilized as a universal fluxing agent to achieve fully vitrified ceramic tiles [3].

Technological samples were blended from composite surface samples gathered across five villages in the Guria region. To determine their elemental and phase composition, the clay samples and the

obsidian additive were subjected to chemical (silicate) analysis, while the clay matrices were evaluated via X-ray diffraction (XRD). The obsidian feedstock was confirmed to be X-ray amorphous. The quantitative chemical compositions of the clay samples and the obsidian are summarized in Table 1.

Table 1

Chemical (silicate) analysis Results

No.	Sample name	SiO_2	Al_2O_3	Fe_2O_3	FeO	TiO_2	CaO	MgO	Na_2O	K_2O
1	Sameba	50, 6	16.0	9.5	-	1.12	1.5	2.5	1.0	1.78
2	Shua Amaghleba	46.7	20.9	12.2	-	1.92	0.8	0.1	0.2	0.7
3	Bucknari	47.0	15.1	9.8	-	1.52	1 , 8	3.7	1.2	1.4
4	Vani	4 7.1	13.4	5.6	-	1.02	2, 5	5.3	0.4	2.0
5	Mamati	40.0	25.0	14.0	-	1.2	0.2	1.0	0.1	0.4
6	Obsidiani	74.9	13.1	0.2	1.1	-	0.17	1.3	3.5	4.1

Silicate analysis reveals that the clays contain high concentrations of coloring oxides (Fe_2O_3 and TiO_2), with Fe_2O_3 ranging between 5.6% and 14.0%, and TiO_2 between 1.0% and 2.0%. Conversely, the Fe_2O_3 content in the obsidian is remarkably low, with ferrous iron oxide (FeO) measured at 1.1%. Additionally, obsidian exhibits high levels of alkalis (Na_2O and K_2O), which play a critical role in facilitating low-temperature vitrification and liquid-phase sintering.

The X-ray diffraction patterns of the clay samples are illustrated in Figures 1–5.

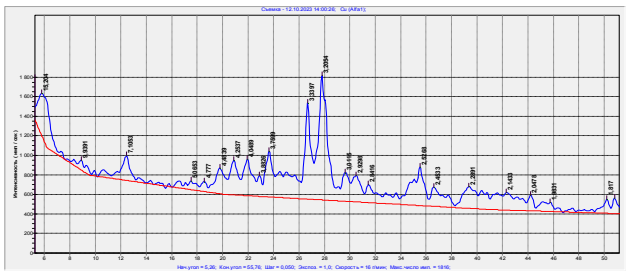

Fig . 1. Village Sameba Clay Sample X-ray

Ca- montmorillonite -15.2; 4.48; 2.52 Å;
Ca-Na- Feldspar -4.04; 3.76; 3.20 Å;
Quartz ; chlorite -7.10; 4.77 Å

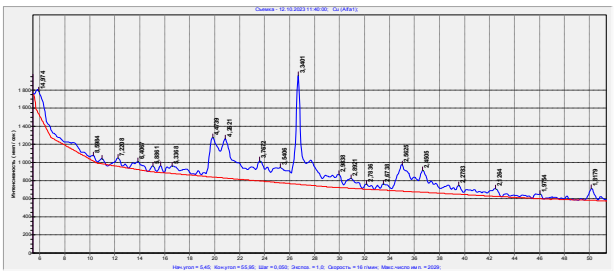

Fig . 2. Village Shua Amaghleba Clay Sample X-ray

Ca- montmorillonite -15.0; 4.47; 2.56 Å;
Halloysite - 4.42; 2.55 Å; Quartz

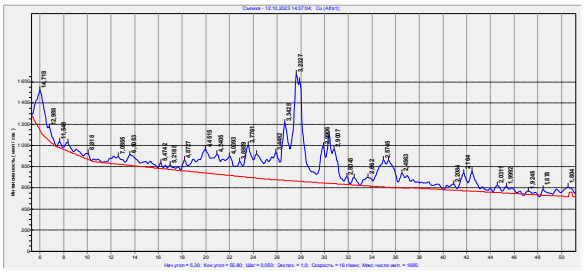

Fig . 3. Village Bucknari Clay Sample X-ray

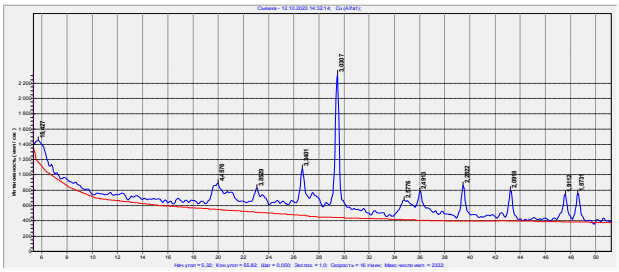

Fig . 4. Village Vani Clay Sample X-ray

Ca - montmorillonite -14.7; 4.45; 2.57 Å;
Ca-Na Feldspar - 4.033; 3.77; 3.23 Å;
Quartz

Ca- montmorillonite -15.4; 4.46; 2.57 Å;
Calcite -3.85; 3.03; 2.49; 2.28; 2.09; 1.911; 1.873 Å;
Quartz - (signs)

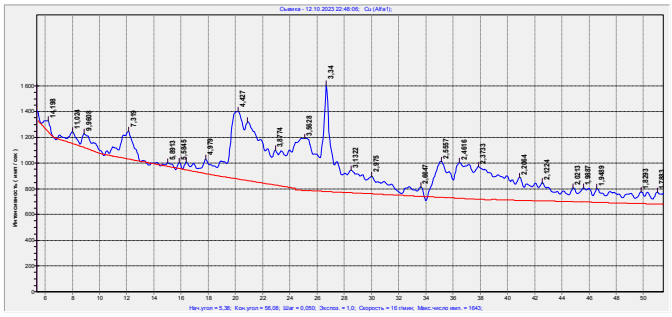

Fig . 5. Village Mamati Clay Sample X-ray

Halloysite -7.32; 4.42; 3.56; 2.55Å; Montmorillonite - 4.42, 2.55 Å;
Quartz ; Illite (signs) -9.96,4.98 Å

X-ray diffraction (XRD) analysis revealed that the clay mineral assemblage of the samples is dominated by halloysite, Ca-montmorillonite, chlorite, and hydromica (illite). The silt fraction of three samples is composed of feldspar and quartz, whereas the remaining two samples contain feldspar, quartz, and calcite.

As shown in Table 1, the Al_2O_3 content of the Shua Amaghleba and Mamati samples is 20.9% and 25.0%, respectively. These relatively high values are associated with the predominance of halloysite (Figs. 2 and 5), a clay mineral characterized by a high alumina (Al_2O_3) content. Conversely, the Sameba, Buknari, and Vani samples, whose clay fraction is dominated by Ca-montmorillonite, contain significantly lower Al_2O_3 concentrations, ranging from 13% to 16%.

The plasticity of the samples was determined, as plasticity is one of the fundamental properties of clay, defined as its ability to undergo changes in shape and dimensions under the action of external forces without the formation of cracks, while

retaining the acquired shape after the removal of the applied load. This property depends primarily on the mineralogical composition and the degree of dispersion of the clay.

The plasticity of the investigated samples was determined using the Vasiliev–Atterberg method, which is based on determining the maximum and minimum amounts of water that can be incorporated into the material. The plasticity index is expressed as the difference between the moisture content at the liquid limit and that at the plastic limit (Atterberg limits) [4]. The results of the plasticity measurements are presented in Table 2.

Table 2

Results of the Determination of Sample Plasticity (Atterberg Limits)

Sample Name	Plasticity Number	Evaluation
Sameba	33.1	Highly plastic
Shua Amaghleba	33.6	Highly plastic
Bucknari	14	Moderately Plastic
Vani	49.5	Highly plastic
Mamati	30.4	Highly plastic

Owing to its exceptionally high plasticity index (49.5) in its natural state, the pressed green tiles made solely from Vani clay developed extensive drying cracks under ambient conditions. The remaining raw clays were likewise found to be unsuitable for tile manufacturing in their unblended states. Consequently, composite formulations incorporating various mineral modifiers (quartz, feldspar, pumice, and obsidian) were systematically investigated to optimize the firing parameters and final properties. The most superior technological parameters were consistently achieved using the clay-obsidian composite system.

The optimized ceramic processing route was executed as follows: the ceramic composite (clay matrix + 40 wt. % obsidian) was wet-milled in a porcelain ball mill with water until a residue of less than 80 μm was obtained. The slurry was dried in an oven to a residual molding moisture content of 4%–6%. Compaction was carried out on an Italian Nannetti Mignon SSN-EA laboratory hydraulic press (Fig. 1). To study the effect of forming pressure on tile quality, specimens were pressed at both 400 kgf/cm^2 and 600 kgf/cm^2. To determine the optimum firing schedule, the green compacts were fired in an Italian Sassuolo Laboratory FCJM10/H51 muffle furnace (Fig. 2) within a temperature range of 1100–1200°C. The heating rate was maintained at 10°C/min up to 1000 °C, and then reduced to 7°C/min, followed by a 30-minute dwell time at the target peak temperatures of 1100°C and 1150 °C. Linear firing shrinkage and water absorption, the critical quality indicators for vitrified tiles, were measured [4, 5, 6], as reported in Table 3.

Table 3

Results of Physical Parameter Determination

Name of the village	Pressing Power , kgf / cm ²	Roasting Temperature , ⁰C	Shortening, %	Water absorption, %
Sameba	400	1100	9.0	2.1
	600		9.3	1.8
	400	1150	10.3	0.01
	600		10.5	0
Shua Amaghleba	400	1100	8.1	1.6
	600		9.6	1.3
	400	1150	10.6	0.04
	600		11.0	0.02
Bucknari	400	1100	5.1	4.4
	600		5.8	4.1
	400	1150	9.8	0.2
	600		10.2	0.1
Vani	400	1100	3.2	11.4
	600		3.8	10.9
	400	1150	9.4	0.0
	600		9.9	0.0
Mamati	400	1100	9.1	0.5
	600		9.5	0.4
	400	1150	12.0	0.07
	600		12.8	0.05

The data in Table 3 demonstrate that 1150 °C is the optimum firing temperature for all five clay-obsidian composite formulations, yielding water absorption values strictly below 0.1%.

The difference in water absorption between compacts pressed at 400 kgf/cm^2 and 600 kgf/cm^2 is negligible. For instance, the Vani clay composite achieved zero water absorption (0.0%) at both pressures when fired at 1150 °C, while the variance for the remaining formulations did not exceed 0.01%–0.02%. Consequently, increasing the molding pressure to 600 kgf/cm^2 is economically unjustified, as a pressure of 400 kgf/cm^2 is fully sufficient to meet standard requirements [7].

Based on these findings, a standard compaction pressure of 400 kgf/cm^2 was selected. The physical, mechanical, and ceramic properties of the resulting tiles, including water absorption, total linear

shrinkage, bulk density, apparent porosity, frost resistance, acid resistance, and flexural strength (both initially and after 40 freeze-thaw cycles), were comprehensively evaluated [8, 9]. Flexural strength testing was performed using an Italian Nannetti CC 96-2006 fleximeter (Fig. 3). The consolidated properties are detailed in Table 4.

Table 4

Physical and Mechanical Properties of Ceramic Tiles Produced from the New Composite Material

Name of the village	Roasting Temperature, ^{0}C	Water absorption, %	Medium Density , kg / m3	Porosity, %	Frost resistance, Cycle	Acid resistance , %	Reduction, %	Pressing Power , kgf / cm ^{2}	Strength, MPa	
									Before freezing	After Freezing
Sameba	1100 1150	3.8 0.05	2309 2410	8.7 0 , 1	- 40	- 98 , 8	8.6 11.0	400 400	- 24.7	- 24.3
Shua Amaghleba	1100 1150	1.6 0.04	2370 2405	3.8 0 , 1	- 40	- 9 8.7	8.1 11.1	400 400	- 26.8	- 26.3
Bucknari	1100 1150	8.4 0.07	2098 2510	17.6 0 , 2	- 40	- 99 , 0	6.4 10.9	400 400	28.5	28.1
Vani	1100 1150	1.4 0.0	1856 2214	21.2 0. 0	- 40	- 99.5	3.2 9.4	400 400	33.8	33.6
Mamati	1100 1150	0.5 0.07	2324 2424	1.2 0.2	- 40	- 98 , 5	9.1 12.0	400 400	29.3	28,7

The experimental data in Table 4 demonstrate that firing the composites at 1150 °C under a compaction pressure of 400 kgf/cm^2 successfully yields fully vitrified ceramic tiles. These products exhibit extremely low water absorption (< 0.1%), high flexural strength, and exceptional acid and frost resistance, strictly satisfying both domestic and international technical standards [7, 10, 11, 12, 13].

Fig.1.
Hydraulic press

Fig. 2
Muffle furnace

Fig. 3
Flexometer

3. CONCLUSION

- The optimum compaction pressure for the clay-obsidian ceramic composite is established at 400 kgf/cm^2.
- The optimum firing temperature required to achieve complete vitrification is 1150 °C.
- During firing at 1150 °C, the amorphous, glass-like structure of the obsidian provides an abundant liquid phase that effectively wets and encapsulates the clay matrix grains, leading to intensive liquid-phase sintering and a highly consolidated composite structure.
- This efficient liquid-phase formation at a lowered temperature (1150°C) ensures exceptional performance metrics in the fired tiles: minimal water absorption (0.0%–0.07%), high mechanical flexural strength (25.0–34.0 MPa), robust frost resistance (passed 40 freeze-thaw cycles), and high acid resistance (98.5%–99.5%).
- In terms of their technological and mechanical parameters, the vitrified ceramic tiles fulfill the requirements of the international standard ISO 13006:2018 (NEW), qualifying them as Class I ceramic tiles.
- The physical-mechanical properties of the developed tiles comply with the technical specifications of GOST 13996-93 (for exterior facade cladding) and GOST 6787-2001 (for ceramic floor tiles).
- The vitrified tiles satisfy the rigorous chemical and thermal criteria set forth by GOST 961-89 for acid-resistant and thermo-acid-resistant ceramic tiles intended for heavy-duty structural applications.

REFERENCES

1. Gegia, N., Enukidze, G., Khachaturiani, K., Kvatashidze, R., Enukidze, L., Ukleba, E., & Guruli, T. (2017). Investigation of the Material Composition and Some Technological Properties of Atsquri Ceramic Clays. Mining Journal, Tbilisi, No. 1(38), pp. 138–142.

2. Patent P20257753B. (2025). Production of High-Quality Ceramic Tiles by Adding Obsidian to Polymineral Clay Batches. Tbilisi, Georgia.
3. Romero, M., & Pérez, J. M. (2015). Relation between the microstructure and technological properties of porcelain stoneware: A review. Materiales de Construcción, 65(320), e065. Madrid, Spain.
4. Guzman, I. Ya. (2004). Praktikum po tekhnologii keramiki [Practical Course on Ceramic Technology]. Moscow: Vysshaya Shkola, 195 p. (in Russian).
5. Ivanova, A. V., & Mikhailova, N. A. (2005). Technological Testing of Clays. Ekaterinburg, Russia.
6. Pérez, J. M., Rincón, J. Ma., & Romero, M. (2012). Effect of molding pressure on microstructure and technological properties of porcelain stoneware. Ceramics International, 38(1), pp. 317–325.
7. International Organization for Standardization. (2018). ISO 13006:2018. Ceramic tiles – Definitions, classification, characteristics and marking.
8. Ivanova, A. V., & Mikhailova, N. A. (2005). Tekhnologicheskie ispytaniya glin [Technological Testing of Clays]. Ekaterinburg, Russia, 41 p. (in Russian).
9. Vakalova, T. V., Pogrebenkov, V. M., & Revva, I.B. (2014). Investigation of Physical-Mechanical and Technological Properties of Clay Raw Materials. Tomsk, Russia, 36 p. (in Russian).
10. GOST 13996-93. Ceramic Facade Tiles and Carpets Made of Them. Technical Conditions.
11. GOST 6787-2001. Ceramic Floor Tiles. Technical Conditions.
12. GOST 6141-91. Glazed Ceramic Tiles for Interior Wall Facing. Technical Conditions.
13. GOST 961-89. Acid-Resistant and Heat-Acid-Resistant Ceramic Tiles. Technical Conditions,

---

უაკ 666.3/7

გურიის პოლიმინერალური თიხებისა და ობსიდიანის კომპოზიტიდან ვიტრიფიცირებული კერამიკული ფილების მიღება

ნ. გეგია, თ. რუხაძე, გ. ენუქიძე, კ. ხაჩატურიანი, მ. ტყემალაძე, თ. ლოლაძე

სსიპ თსუ, ალ. თვალჭრელიძის სახ. მინერალური ნედლეულის კავკასიის ინსტიტუტი. მინდელის ქუჩა 11, 0186, თბილისი, საქართველო

E-mail: nestan.gegia@tsu.ge; temo798@gmail.com

რეზიუმე. სტატიაში განხილულია ობსიდიანის როლი გურიის დაბალხარისხიანი, პოლიმინერალური თიხებისგან შემდგარ კომპოზიტში, რომელმაც შესაძლებელი გახადა კომპოზიტიდან (თიხა+ობსიდიანი) ვიტრიფიცირებული კერამიკული ფილების დამზადება.

მიზანი. კვლევების მიზანს წარმოადგენს გურიის რეგიონის ტერიტორიაზე გავრცელებული პოლიმინერალური თიხების კომპოზიტში ახალი კომპონენტის დამატებით მაღალხარისხიანი კერამიკული ფილების მიღება, რომლებიც დააკმაყოფილებს სტანდარტების მოთხოვნებს.

მეთოდი. კვლევებში გამოყენებული იქნა ქიმიური და რენტგენოფაზური ანალიზები.

რენტგენოფაზური ანალიზი - დიფრაქტომეტრი Дрон-4.0, სპილენძის ანოდით და ნიკელის ფილტრით; გადაღების სიჩქარე - 2 გრად/წთ, ტალღის სიგრძე - 1.54778 Å;

ფილების დაწნეხვა- იტალიური Mignon SSN-EA ლაბორატორიული ჰიდრავლიკური პრესი;

გამოწვა - იტალიური FCJM10/H51 მოდელის მუფელის ღუმელი; მაქსიმალური ტემპერატურა- 1300 ^{0}C, ტემპერატურის მატება 10 ^{0}C წუთში, დაყოვნების დრო - 20 წთ;

მექანიკური სიმტკიცე ღუნვაზე - იტალიური CC 96-2006 მოდელის ფლექსიმეტრი.

შედეგი. ქიმიური და რენტგენოფაზური ანალიზებით შესწავლილი იქნა გურიის რეგიონის კერამიკული თიხების ნივთიერი შედგენილობა. დამატებითი კომპონენტის გარეშე აღნიშნული თიხები კერამიკულ ფილებად გამოუსადეგარია. შედგენილი კომპოზიტისგან 400 კგძ/სმ^2 დაწნეხილი კერამიკული ფილების თიხური ნაწილაკების დაბალ ტემპერატურაზე (1150 ^{0}C) მინისებრი ფაზით კარგმა დაფარვამ უზრუნველყო ფილების ძალიან დაბალი წყალშთანთქმა (0,0-0,07 %), მაღალი სიმტკიცე (25,0 – 34,0 მპა), ყინვა (40 ციკლი) და მჟავამედეგობა (98,5-99,5 %).

დასკვნა. კვლევების შედეგად დამუშავებული ტექნოლოგიით მიღებული ვიტრიფიცი-რებული კერამიკული ფილები ტექნოლოგიურ - მექანიკური პარამეტრებით აკმაყოფილებს საერთაშორისო სტანდარტის (ISO 13006:2018, NEW) მოთხოვნებს, რომლის თანახმად ისინი განეკუთვნებიან პირველ კლასის ფილებს, ასევე, სტანდარტების: **13996-93** (კერამიკული ფილები გარე ფასადის მოპირკეთებისათვის), **6787-2001** (კერამიკული ფილები იატაკისათვის) და **961-89** (მჟავამედეგი და თერმომჟავამედეგი კერამიკული ფილები), ტექნიკური პირობების მოთხოვნებს.

საკვანძო სიტყვები: გამოწვა, ვიტრიფიცირება, თიხა, კერამიკული ფილა, კომპოზიტი, მჟავა-მედეგობა, ობსიდიანი, სიმტკიცე, ფორიანობა, ყინვამედეგობა, შეკლება, წყალშთანთქმა.

DOI https://doi.org/10.36073/2960-9534

THE GEORGIAN CERAMISTS ASSOCIATION JOINED
THE INTERATIONAL CERAMIC FEDERATION SINCE 2008

THE GEORGIAN CERAMISTS ASSOCIATION HAS BEEN A MEMBER
OF THE EUROPEAN CERAMIC SOCIETY SINCE 2002

THE GEORGIAN CERAMIC ASSOCIATION WAS FOUNDED IN 1998
THE MAGAZINE WAS FOUNDED IN 1998

TBILISI, "INTERNATIONAL JOURNAL OF CERAMICS, COMPOSITES, SCIENCE AND ADVANCED TECHNOLOGIES", Vol. 28. 1(55). 2026

Reference of magazine is obligatory on reprinting

Print circulation 5,25. Contract amount 50. Printed A4 format.

GEORGIAN CERAMISTS ASSOCIATION. Tbilisi. Str. Kostava 69. Phone: +995 599 151957
E-mail: kowsiri@gtu.ge, Zviad Kovziridze

http://ceramics.gtu.ge